Sapienza University of Rome

Department of Information Engineering, Electronics and Telecommunications

GNSS-based passive radar techniques for maritime surveillance

Author

Federica Pieralice
Department of Information Engineering, Electronics and Telecommunications

Thesis Supervisor

Prof. Debora Pastina
Department of Information Engineering, Electronics and Telecommunications

Contents

List of figures

List of tables

List of acronyms

GNSS	Global Navigation Satellite System
GPS	Global Positioning System
GLONASS	GLObal NAvigation Satellite System
AIS	Automatic Identification System
PBR	Passive Bistatic Radar
PCL	Passive Coherent Location
DVB-T	Digital Video Broadcasting - Terrestrial
GSM	Global System for Mobile Communications
RCS	Radar Cross Section
TMC	Target Motion Compensation
M-MTD	Maritime - Moving Target Detection
TDOA	Time Difference Of Arrival
DVB-S	Digital Video Broadcasting - Satellite
SAR	Synthetic Aperture Radar
ISAR	Inverse Synthetic Aperture Radar

LEO	Low Earth Orbit
CPI	Coherent Processing Interval
LOS	Line of Sight
DOA	Direction-of-Arrival
CA	Cell Average
CFAR	Constant False Alarm Rate
CUT	Cell Under Test
PRN	Pseudo Random Noise
RHCP	Right Hand Circularly Polarized
LHCP	Left Hand Circularly Polarized
ROI	Region Of Interest
MSC	Multistatic Compensation
QI	Quadratic Integrator
LRT	Likelihood Ratio Test

Abstract

The improvement of maritime traffic safety and security is a subject of growing interest, since the traffic is constantly increasing. In fact, a large number of human activities take place in maritime domain, varying from cruise and trading ships up to vessels involved in nefarious activities such as piracy, human smuggling or terrorist actions. The systems based on Automatic Identification System (AIS) transponder cannot cope with non-cooperative or non-equipped vessels that instead can be detected, tracked and identified by means of radar system. In particular, passive bistatic radar (PBR) systems can perform these tasks without a dedicated transmitter, since they exploit illuminators of opportunity as transmitters. The lack of a dedicated transmitter makes such systems low cost and suitable to be employed in areas where active sensors cannot be placed such as, for example, marine protected areas. Innovative solutions based on terrestrial transmitters have been considered in order to increase maritime safety and security, but these kinds of sources cannot guarantee a global coverage, such as in open sea. To overcome this problem, the exploitation of global navigation satellites system (GNSS) as transmitters of opportunity is a prospective solution. The global, reliable and persistent nature of these sources makes them potentially able to guarantee the permanent monitoring of both coastal and open sea areas.

To this aim, this thesis addresses the exploitation of Global Navigation Satellite Systems (GNSS) as transmitters of opportunity in passive bistatic radar (PBR) systems for maritime surveillance. The main limitation of this technology is

the restricted power budget provided by navigation satellites, which makes it necessary to define innovative moving target detection techniques specifically tailored for the system under consideration. For this reason, this thesis puts forward long integration time techniques able to collect the signal energy over long time intervals (tens of seconds), allowing the retrieval of suitable levels of signal-to-disturbance ratios for detection purposes.

The feasibility of this novel application is firstly investigated in a bistatic system configuration. A long integration time moving target detection technique working in bistatic range&Doppler plane is proposed and its effectiveness is proved against synthetic and experimental datasets. Subsequently the exploitation of multiple transmitters for the joint detection and localization of vessels at sea is also investigated. A single-stage approach to jointly detect and localize the ship targets by making use of long integration times (tens of seconds) and properly exploiting the spatial diversity offered by such a configuration is proposed. Furthermore, the potential of the system to extract information concerning the detected target characteristics for further target classification is assessed.

Chapter 1

Introduction

1.1 Background

Motivated by the well-known benefits of passive radars, over the last years the radar community put a lot of effort in investigating how to exploit existing transmissions to increase the levels of safety and security in the maritime domain. Indeed, the lack of a dedicated transmitter makes such systems inherently low cost, since only the receiver has to be developed. Moreover, they are much lighter than active systems and hence can be deployed in places where heavy active sensors cannot be installed, such as, for example, marine protected areas. As they do not transmit any signals, they allow covert operations, they are largely immune to jamming and, since the system is intrinsically bistatic, they can represent an effective anti-stealth defence option. Different kinds of terrestrial illuminators of opportunity have been proved able to increase safeguarding maritime security such as GSM [1] and WiMAX base stations [2]. One of the most promising passive radar technologies in this field considers the Digital Video Broadcasting-Terrestrial (DVB-T) transmitters [3]. These sources offer a sufficiently high-transmitted power allowing very long detection ranges and the potential of these illuminators to monitor maritime traffic has been proved at both theoretical and experimental levels. Nevertheless, terrestrial-based illuminators of opportunity cannot guarantee a global coverage, as for instance in open sea.

Global coverage can be obtained by switching to passive radar systems based on opportunistic satellite transmitters as the Global Navigation Satellite Systems (GNSS) or the many commercial communication satellites in geostationary/geosynchronous orbits (as for example for digital television broadcasting). Suitable GNSS candidates can be the Global Positioning System (GPS) [4], the GLObal NAvigation Satellite System (GLONASS) [5], Beidou [6], or the new European Galileo constellation [7]. From a passive radar perspective, GNSS signals are particularly attractive. First, the radar user has full knowledge of the transmitted waveform, which is also optimized for remote synchronization. Moreover, with their relatively large signal bandwidth it is possible to obtain a suitable resolution in the framework of the maritime surveillance. Noticeably, with respect to commercial communication satellites, GNSS offers a unique combination among global coverage, complete reliability and spatial/waveform diversity. Indeed, GNSS signals are available over the entire Earth's surface, even at the poles. Spatial diversity is obtained thanks to the availability of multiple satellites simultaneously illuminating the same area from different angles: typically, 6-8 satellites are made available by the single GNSS constellation so that up to 32 satellites could be exploited when all 4 GNSS systems will be operative. Waveform diversity is obtained thanks to the transmission of different signals (even in different frequency bands) from the single satellite. Remarkably, both spatial and waveform diversity can be captured by a single receiver inherently providing a multi-static radar system where multiple signals could be combined to increase the performance.

The above features of GNSS constellations, along with the highly time precise nature of the transmitted signals, stimulated their alternative utilizations for remote sensing purposes since more than two decades [8]. The analysis of the GNSS reflected signals (GNSS-Reflectometry) has brought to a number of well-established technologies to remotely sense the atmosphere and ionosphere, ocean, land surface and cryosphere [9][10]. In the field of radar sensors, the exploitation of GNSS signals

has been investigated from several years for passive synthetic aperture radar imaging [11]-[18], with the ultimate goal to achieve persistent local area monitoring. With specific regard to surveillance purposes, some studies have been conducted for the detection of aerial targets [19]-[21], whereas only few investigations have been carried out for maritime surveillance purposes. In particular, the feasibility to use GNSS signals has been investigated in [22]-[23] considering GNSS-R technology. Concerning radar technologies, in [24] the feasibility of maritime targets detection has been investigated using GPS signals with specific reference to a configuration comprising transmitter, airborne receiver and target aligned on the same direction so that a monostatic behaviour of the target can be assumed. The reported results provided a theoretical confirmation of the results in [25] where some experimental evidence of the detectability of a stationary target by means of GPS signal was given.

The major issue in using GNSS satellites as illuminators of opportunity is the very low level of electromagnetic field reaching the Earth' surface [26], which makes conventional techniques used for target detection inside terrestrial-based passive radar systems not directly applicable to the GNSS-based passive radar. To counteract the low level of signal to disturbance ratio in input at the receiver, target energy should be integrated over long integration times. One of the main issues arising with the increase of the integration time is the migration of the target trough the resolution cells, which needs to be compensated to do not compromise the detectability of the target. To extend the coherent processing interval (CPI) in the spite of the migration of the moving target through the resolution cells, a number of methods have been proposed, such as the Radon Fourier Transform [27], the Radon Fractional Fourier Transform [28] and the stretch processing [29]. However, it will be shown that the GNSS-passive radar may require integration times that can be up to several tens of seconds. Such long integration times are fundamentally possible due to GNSS coverage, but their exploitation implies the need of techniques tailored for the case of interest. Particularly, it should be noted that a full coherent

integration as in [27]-[29] is not feasible over such long dwells and therefore it is necessary to resort to hybrid coherent/non-coherent integration of the received signal.

Apart the global and persistent coverage enabled by GNSS, the unique feature of these systems is that they operate with large constellations. Remarkably, GNSS operate with code (or frequency) division multiple access schemes, so that a single receiver inherently forms a passive multistatic radar system. The multistatic configuration offers a number of benefits with respect to its bistatic (i.e., single satellite) counterpart. For example, in GNSS-based SAR imagery it has been shown that multi-perspective acquisitions can drastically improve the spatial resolution [16], [18] and enhance image information [30]. With respect to the maritime surveillance application, the availability of multiple emitters brings to three main added values: i) the possibility to estimate the ship Direction-of-Arrival (DOA) without having to consider multi-beam or array receiving systems; ii) the possibility to collect data samples over multiple bistatic links, potentially improving the system power budget; iii) the exploitation of a large spatial diversity, greatly alleviating the deleterious effects of target RCS scintillations [31].

Recently, it has been demonstrated that vessels at sea can be simultaneously detected by multiple satellites (even belonging to different constellations). In [32] the detected target instantaneous locations have been extracted by means of multilateration. In particular, the spherical intersection method [33] has been applied to a set of bistatic range and Doppler plots achieved by considering twelve GNSS emitters, showing that sufficient localization accuracy for practical purposes can be achieved. Nevertheless, it should be pointed out that even though this approach has been proved to be effective in target localization, it strictly requires the targets to be detected at the individual bistatic levels. Therefore, the localization procedure is subject to the detection of targets in a scenario where the power budget represents the fundamental bottleneck. Since the combination of the information

coming from the multiple bistatic links takes place after the bistatic detection thresholding, this approach cannot fully benefit of the available spatial diversity to reinforce the total target power.

In order to overcome the limitations described above, the main objective of this thesis is the development of innovative techniques specifically tailored for the GNSS-based passive radar systems for the detection, localization and classification of maritime moving targets.

1.2 Novel contributions

The work done for this thesis project fits within the field of maritime target detection, localization and features extraction in passive bistatic radar (PBR) systems based on GNSS: the work has been carried out mainly in the ambit of the European H2020 project spyGLASS "GALILEO-BASED PASSIVE RADAR SYSTEM FOR MARITIME SURVEILLANCE" [34]. The novelties and the main results obtained during this work are presented below.

As discussed above, the fundamental bottleneck of GNSS-based passive radar systems for target detection is the restricted power budget provided by navigation satellites, which makes it necessary to define innovative moving target detection techniques specifically tailored for the system under consideration. To this aim, initially a technique that exploits a single GNSS transmitter and a stationary receiver has been developed [34]-[38] and subsequently the case of multiple transmitters has been considered to jointly detect and localize the target [39]-[41].

First, the single-channel technique is proposed and results against synthetic and experimental datasets are presented to show the capability of the technique to integrate the signal energy over long time intervals (tens of seconds), allowing the retrieval of suitable levels of signal-to-disturbance ratios for detection purposes. Then the multi-channel technique is introduced, since the performance of the system can be improved by exploiting the multiple transmitters in addition to the

long integration time. It is also shown by means of synthetic and experimental results that the multistatic geometry allows the target localization.

Furthermore, a preliminary study is carried out to identify the dimensional class of the detected vessel [42]. A technique retriving the target length in range and cross-range domains is presented and tested against experimental data.

1.3 Thesis structure

The thesis is structured as follows:

Chapter 2 provides an overview of passive radar based on satellite illuminators of opportunity. After a brief introduction to the bistatic radar, the passive radar systems are described with a short presentation of the main satellite opportunity sources considered in recent years.

Chapter 3 puts forward single-channel M-MTD techniques able to integrate the reflect signal energy over long time intervals (tens of seconds) by properly correcting the target range and Doppler migration, allowing the target detection. First, the experimental confirmation of the feasibility of GNSS reflected signals acquisition to detect maritime targets in general bistatic geometries was demonstrated against a large target [namely, high radar cross section (RCS) targets] at relatively short receiver distance. Then, some experimental results against targets relatively small showed the effectiveness of the long-integration time techniques at enabling MTD for ships undetectable with the conventional (i.e., short integration time) algorithms and, at the same time, increasing the detection range.

Chapter 4 investigates the exploitation of both the long integration time and the multiple transmitters to enhance the detection performance and to enable the vessels localization. A multi-channel M-MTD technique is proposed in order to increase the signal-to-noise ratio (SNR) level and, at the same time, to measure the target DOA, thus providing a joint target detection and localization even of targets not detectable when the detection threshold is set at the bistatic level. Particularly,

a centralized detection method is considered implementing a single-stage to detect and localize the target. Theoretical and simulated performance analysis is proposed and also validated by means of experimental results considering Galileo transmitters and different types of targets of opportunity in different scenarios.

Chapter 5 deals with the extraction of features of detected maritime moving targets. The possibility to retrieve information about the size of the detected target in range and cross-range domain is investigated. A preliminary experimental study to demonstrate the potential of the system to extract information concerning the detected target characteristics is provided.

Conclusions summarize the main results of the study, which have led to this thesis; additionally, the conclusions are drawn and future activities are discussed.

Chapter 2

Passive Radar overview

The term RADAR was coined in 1940 by the US Navy as an acronym for RAdio Detection And Ranging, which describes its main functions. Radar is an electromagnetic sensor for the detection and determination of the position (distance, height and azimuth) and velocity of reflecting targets both fixed and mobile, such as aircraft, ships, vehicles, atmospheric formations or soil. The radar radiates electromagnetic waves that propagate at the speed of light. If the wave intercepts an object, its power is backscattered and some of reradiated energy is returned to the radar antenna. Radars have represented an element of remarkable importance in the technological development of the twentieth century, first for the military applications, then for the control of air and naval traffic, for environmental and meteorological applications, and finally for space applications in the field of terrestrial remote sensing and in the exploration of the solar system [43]. The conventional configuration for a radar is the monostatic configuration (Figure 2.1). In a monostatic radar the transmitter and receiver are co-located. Otherwise, the bistatic radar uses antennas at separate sites for transmission and reception. The general characteristics of bistatic radar are briefly discussed below considering also the passive radar systems, a specific case of bistatic radar.

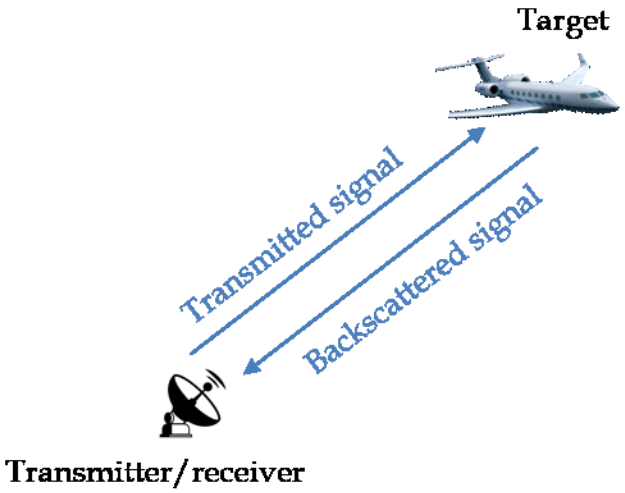

Figure 2.1 - Monostatic radar

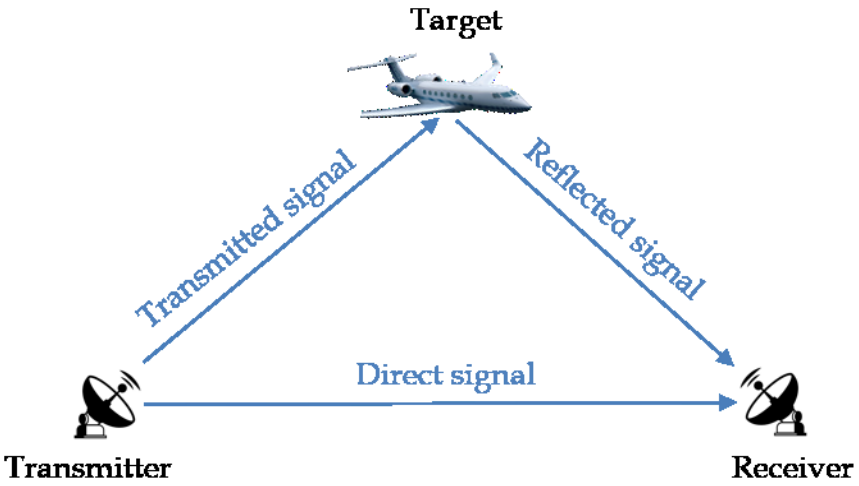

Figure 2.2 - Bistatic radar

2.1 Bistatic radar

Bistatic radar is defined as a radar using antennas for transmission and reception at sufficiently different locations and the antenna separation is usually a significant fraction of the target range [44]. A general configuration is depicted in

Figure 2.2. The transmitter and the receiver are separated by a distance L, called the baseline. R_T is the range from the transmitter-to-target and the angle θ_T is the transmitter look angle. R_R is the range from the receiver-to-target and the angle $\theta_R$is the receiver look angle. The angle $\beta = \theta_T - \theta_R$ between the transmitter and receiver with the vertex at the target is called bistatic angle. A bistatic radar measures the range sum $(R_T + R_R)$ for target location. Contours of constant bistatic range sum are ellipses, whose foci are transmitter and receiver sites. Typically, the range sum is calculated as $(R_T + R_R) = c\Delta T$, where ΔT is the time interval between reception of the transmitted signal and reception of the target echo. The target range from the receiver can be calculated as:

$$R_R = \frac{(R_T + R_R)^2 - L^2}{2(R_T + R_R + Lsin\theta_R)} \tag{2.1}$$

The bistatic radar equation is derived in the same way as the monostatic radar but taking into account that R_T and R_R are different, and so the antenna gains of the transmitting (G_T) and receiving antennas (G_R) that must be evaluated in the direction of the target:

$$(R_T R_R)_{max} = \sqrt{\frac{P_T G_T G_R \lambda^2 \sigma_b {F_T}^2 {F_R}^2}{(4\pi)^3 K T_0 F B L_T L_R (S/N)_{min}}} \tag{2.2}$$

where P_T is the transmitted power, P_n is the power noise, G_T and G_R are the transmitting and receiving antenna gain respectively, λ is the wavelength, σ_b is the bistatic cross-section, F_T the pattern propagation factor for transmitter-to-target-path, F_R the pattern propagation factor for target-to-receiver path, K the Boltzmann's constant, T_0 the receiving system noise temperature, B noise bandwidth of receiver's predetection filter, $(S/N)_{min}$ the signal-to-noise ratio required for the detection and L_T (L_R) transmitting (receiving) system losses (> 1) not included in other parameters. The constant SNR contours are called ovals of Cassini depicted in Figure 2.3. The signal-to-noise ratio is highest for targets close to the transmitter or close to the receiver.

When the transmitter, target and receiver are moving, the bistatic Doppler could be defined starting from the range sum as:

$$f_d = \frac{1}{\lambda}\frac{\partial}{\partial t}[R_T + R_R] \tag{2.3}$$

Doppler shift depends on the motion of target, transmitter and receiver, and in the general case the equations are quite complicated.

In the case when the transmitter and receiver are stationary and only the target is moving, the Doppler shift is given by:

$$f_d = (2V/\lambda)cos\delta cos(\beta/2) \tag{2.4}$$

where V is the target velocity, δ is the bistatic angle referred to the bistatic bisector.

In a bistatic radar the transmitter can be designed and controlled by the bistatic radar, as well as the monostatic case, or it can be a transmitter of opportunity designed for other functions. This kind of radars are called passive bistatic radar (PBR) or passive coherent location (PCL).

The receiver in a bistatic radar is undetectable, since it is passive, and potentially simple and cheap. Furthermore, bistatic radars may have counter-stealth capabilities, as the target shape is designed to reduce monostatic RCS, not bistatic RCS. However, the geometry is complex compared to monostatic geometry and the synchronization between the receiver and the transmitter is necessary.

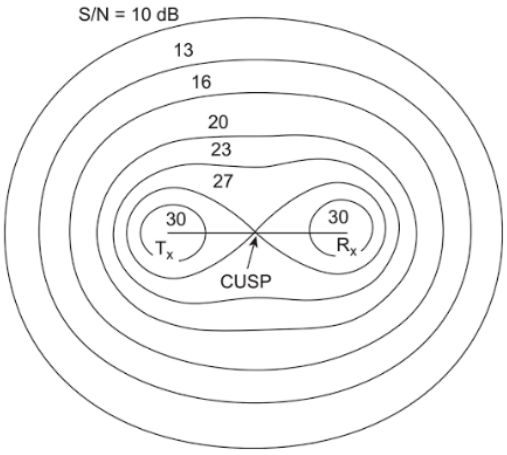

Figure 2.3 - Contour of constant SNR-ovals of Cassini, with $K = 30L^4$ being $K = ((R_T R_R)^2_{max}\ (SNR)_{min}$ the bistatic radar constant (from [44])

2.2 Passive bistatic radar

As mentioned before, PBR systems are a class of bistatic radar systems that do not send a dedicated electromagnetic signal, but instead they exploit electromagnetic signals emitted by other sources for other purposes. For this reason, only the receiver must be designed. Indeed, the lack of dedicated transmitter makes PCL very attractive for the following advantages:

- low cost of operation and maintenance;
- covert operation;
- non-additional demand on spectrum resources;
- small size and hence easier deployment in places where conventional radars cannot be fielded;
- reduced impact on the environment and reduced Electro-Magnetic pollution.

However, the PBRs have some disadvantages. The main drawback stays in the fact that the transmitted waveform is not under control of the radar designer. This entails low power level, time-varying characteristics and high sidelobes in the

ambiguity function that can mask targets. Target echoes can be masked also by the direct signal from the transmitter, the strong clutter or multipath echoes and from other strong targets echoes at short range.

The performances of the PBR systems are determined by the transmitted waveform, the position of the transmitter, the position of the receiver and the position and velocity of the target. As a consequence, the radar design and optimization are highly limited since many factors are not within the control of the radar designer.

2.3 Passive multistatic radar

Multistatic radar can be considered extensions of bistatic radar. A multistatic radar uses two or more transmitter-receiver pairs coupled together for target observation (Figure 2.4). It is also configured to combine data from different bistatic couple to improve the quality of target parameters estimates and to localize target exploiting the spatial diversity [45].

As already mentioned above, the bistatic range is the sum of transmitter-target and target-receiver ranges and the place of constant-range bistatic points is an ellipse. In the multi-static case multiple transmitter-receiver pairs are available, so it is possible to have multiple bistatic measurements. In this case the position of the target can be calculated as the intersection of the different ellipses in the plane. In three-dimensional space at least three ellipsoids are necessary to localize a target unambiguously. In passive radar, the target position is calculated by measuring time differences of arrival (TDOA). The locus of points of constant TDOA defines a hyperbola in the plane or a hyperboloid in three-dimensional space. The target can be located by finding the intersection of the hyperbolas or hyperboloids.

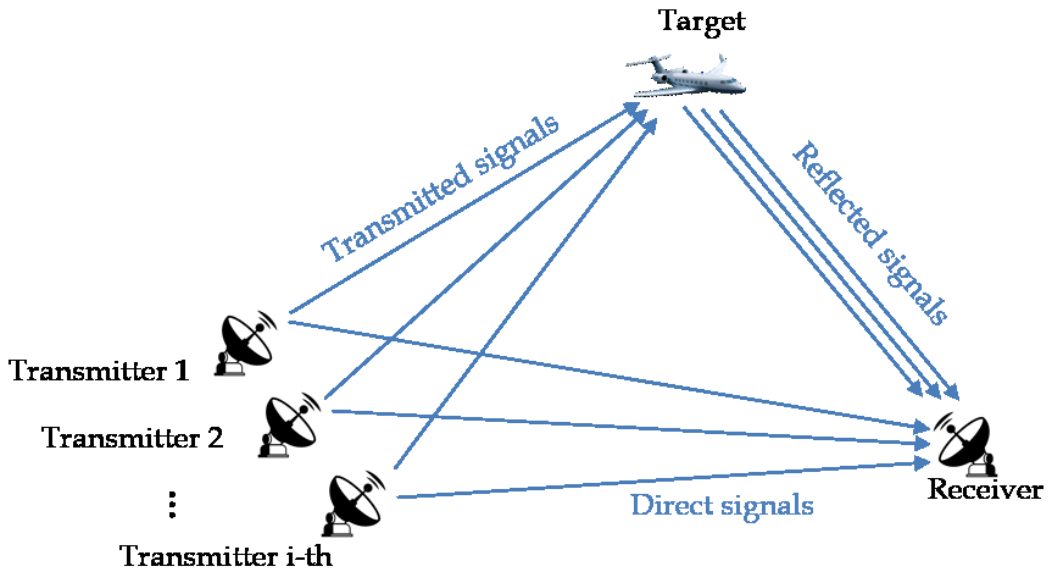

Figure 2.4 – Passive multistatic radar

2.4 Passive radar based on satellite illuminators of opportunity

The possibility of use electromagnetic energy emitted by existing communications, broadcasting, navigation satellites or radar satellites has been discussed in several studies. Traditionally, PBR based on terrestrial sources such as DVB-T and GSM have been largely investigated and proven to be effective due to their high powers: nevertheless, terrestrial-based passive radar cannot provide monitoring of areas such as the open sea. The global coverage offered by satellite illuminators makes them extremely appealing as gap fillers for those areas that cannot be reached by terrestrial transmissions such as the remote areas of the globe. However, one of the biggest issues of satellites for passive radar applications is the low level of power density reaching the Earth surface.

In the following a brief overview of the main satellite sources of opportunities considered until now is provided.

2.4.1 GNSS as illuminators of opportunity

Over the last decade, work pioneered at the University of Birmingham has demonstrated the feasibility in using passive bistatic SAR based on GNSS for Earth observation [12].

In addition to the well-known advantages of passive radars, which include low costs, covert operation and reduce environment pollution, GNSS represent an ideal choice also for their constant global coverage and for the availability of multiple sources. Furthermore, GNSS exhibit relatively large signal bandwidths, for Galileo E5 is approximately 20 MHz and can therefore provide sufficient range resolutions. A receiver used in passive bistatic SAR is very similar to a standard navigation receiver. The receiver can be stationary or mounted on aircraft on ground moving receiver and comprises two separate channels: the heterodyne channel (HC) and the radar channel (RC). The first channel is equipped with a low-gain antenna to record direct satellite signal for signal synchronization purpose. The second channel uses a high gain antenna to collect signal from the area under surveillance.

The range resolution depends on the signal bandwidth and on the acquisition geometry. Instead, to obtain a sufficiently high azimuth resolution in this mode a long dwell time is required [46]. As an example, dwell intervals of 300 s (5 min) yields an azimuth resolution of approximately 3-4 m for a fixed receiver, while for a ground moving receiver azimuth resolution of approximately 1 m can be achieved for dwell time greater than 30 s [12].

The feasibility of GNSS-based radar imaging was demonstrated by means of a receiving systems made at the University of Birmingham. Experiments were conducted with the received both fixed on the ground and onboard a ground moving vehicle or helicopter [47]-[49]. The experimental results, of which an example is shown in Figure 2.5, confirmed the validity of the experiments, indeed

in the images the buildings and the tree lines appear as high intensity echoes. At the same time, the grassy areas appear as areas of low reflectivity areas in the images.

In [16], the spatial diversity inherent in GNSS-based SAR has been investigated to improve image spatial resolution.

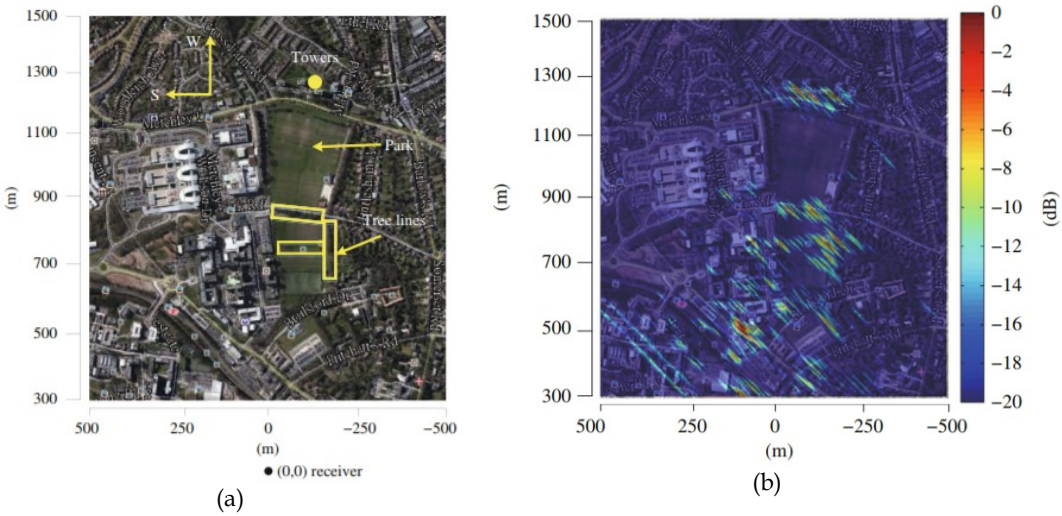

Figure 2.5 – (a) Google Earth photograph of the target size, (b) GNSS-based SAR image superimposed on imaging scene (from [49])

2.4.2 DVB-S as illuminators of opportunity

Recent works have shown the possibility of exploiting broadcasting signals (such as DVB-S and DVB-S2) as illuminators of opportunities for passive ISAR imaging. The exploitation of telecommunication geostationary satellites as opportunity sources is very attractive for their constant and extensive coverage, even in open sea areas. DVB-S transmits in Ku-band providing a bandwidth suitable for achieving medium/high range resolutions.

The use of DVB-S for ISAR imaging was proposed in [50]. The feasibility to obtain images of vessels of acceptable quality using telecommunication geostationary satellites as illuminators of opportunity and a stationary device mounted on the coast as receiver was demonstrated.

The possibility of obtaining ISAR images from DVB-S signals has been demonstrated in [51] and [52] with experimental results. Despite the low range resolution, the experimental results demonstrate that these passive ISAR images can be exploited for identification and classification purpose [53].

2.4.3 LEO as illuminators of opportunity

Transmitters in low earth orbit (LEO) were considered in the field of bistatic SAR. The spatial separation between transmitter and receiver has advantages and disadvantages in bistatic SAR. The advantages include the availability of additional information regarding the imaged scene and the targets in the scene, the potential improvement of the SNR value and the spatial resolution, the robustness to jamming and the possibility to exploit opportunity transmissions. The disadvantages are mainly related to the greater complexity of the system operation and data processing. In [54] the case of hybrid spaceborne–airborne observations is considered. The X-band spaceborne–airborne bistatic SAR experiment is presented, where the radar satellite TerraSAR-X in LEO is used as transmitter and the German Aerospace Center's (DLR) airborne radar system F-SAR is used as receiver. The experiment includes an accurate synchronization procedure (performed in processing steps) necessary to make high-resolution imaging feasible. A comparison of the monostatic TerraSAR-X and bistatic TerraSAR-X/F-SAR images has shown some interesting properties. The bistatic image has revealed an advantage in terms of resolution and SNR and, in the total absence of range ambiguities, it has shown however a variation in spatial resolution and in SNR. Instead, a more homogeneous behavior in terms of SNR is shown in the monostatic image. The differences in scattering mechanism and information content demonstrate the capabilities of bistatic SAR to be a valuable complement to existing monostatic systems.

The exploitation of TerraSAR-X as a transmitter was also considered in [55]. The bistatic spaceborne/airborne SAR experiments with the radar satellite

TerraSAR-X as a transmitter and the airborne SAR sensor Phased Array Multifunctional Imaging Radar (PAMIR) of the Fraunhofer Institute for High Frequency Physics and Radar Techniques (FHR) as a receiver are considered. The major differences between the FHR and DLR experiments are the data acquisition and synchronization strategy, the signal bandwidth, and the capability of beam steering of the PAMIR system. The comparison of the bistatic SAR images with the corresponding monostatic images of PAMIR and TerraSAR-X has shown considerable differences regarding shadowing, foreshortening, and scattering effects. These differences can be exploited, e.g., for classification and image interpretation. Therefore, it is shown that the hybrid bistatic SAR is a worthwhile and helpful addition to current monostatic SAR.

Chapter 3

GNSS-based radar system overview

The concept of the GNSS-based radar for maritime targets detection is shown in *Figure 3.1*. The transmitters of opportunity are GNSS satellites while the receiver is in a remote location above the sea. The receiver could be mounted on a buoy or on a balloon. The receiver is equipped with two RF channels. The former (referred to as reference channel) uses a low-gain antenna pointed toward the sky to record the direct signals from GNSS satellites, whereas the latter (surveillance channel) employs a higher-gain antenna pointed toward the sea area to be surveyed and collecting the resulting signal reflections. Since GNSS operate on frequency or code division approaches, the receiver can separate the signals emitted by different sources, and each bistatic link can be separately processed.

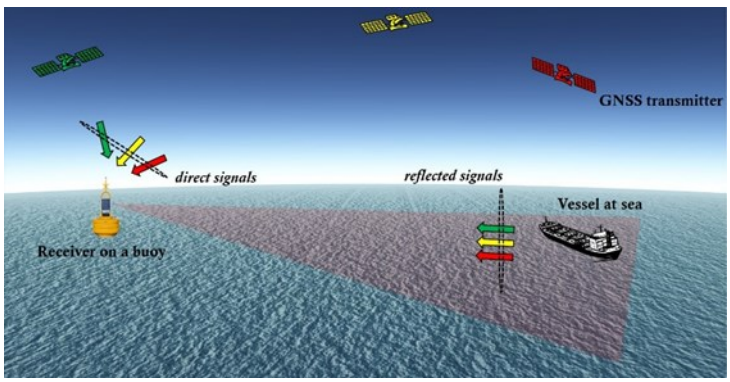

Figure 3.1 - System concept for GNSS-based radar for maritime surveillance

3.1 System acquisition geometry

The overall system geometry is sketched in Figure 3.2 showing the (O, x, y, z) cartesian reference system, which is obtained as a rotation of the East-North-Up (ENU) reference system making the x-axis coinciding with the projection on the ground plane (x, y) of the pointing direction of the surveillance antenna. Without loss of generality, assume the origin of the reference system on the projection onto the ground plane (x, y) of the receiver position. Let M be the number of satellites in visibility and let T_a be the aperture time. Since the focus is on ship targets and a flat Earth geometry can be assumed (because of the relatively small size of the observed area), the height of the target can be neglected. Let $\boldsymbol{TX}_m(u) = [x_m(u), y_m(u), z_m(u)]^T$, $\boldsymbol{RX} = [0,0,0]^T$ and $\boldsymbol{TG}(u) = [x_t(u), y_t(u), 0]^T$ denote respectively the mth transmitter, receiver and target instantaneous positions at time u within the interval $\left[-\frac{T_a}{2}, \frac{T_a}{2}\right]$. The paths mth transmitter to target, target to receiver, and mth transmitter to receiver (i.e., the mth baseline) are therefore $R_{T_m}(u) = |\boldsymbol{TX}_m(u) - \boldsymbol{TG}(u)|$, $R_R(u) = |\boldsymbol{TG}(u) - \boldsymbol{RX}|$, and $R_{B_m}(u) = |\boldsymbol{TX}_m(u) - \boldsymbol{RX}|$, respectively. Further, it is useful to define the following angles. $\phi_m(u)$ is the clockwise angle on the ground plane $(Z = 0)$ between the radar LOS and the mth satellite projection on the ground plane; $\theta_m(u)$ is the out-of-plane angle between the ground plane and the mth satellite; finally, $\phi_t(u)$ is the clockwise angle on the ground plane between the radar LOS and the target, namely the target DOA. Therefore, the transmitter and satellite coordinates can be written as

$$\boldsymbol{TX}_m(u) = \begin{bmatrix} R_{B_m}(u)\cos\theta_m(u)\cos\phi_m(u) \\ R_{B_m}(u)\cos\theta_m(u)\sin\phi_m(u) \\ R_{B_m}(u)\sin\theta_m(u) \end{bmatrix}$$
$$\boldsymbol{TG}(u) = \begin{bmatrix} R_R(u)\cos\phi_t(u) \\ R_R(u)\sin\phi_t(u) \\ 0 \end{bmatrix} \tag{3.1}$$

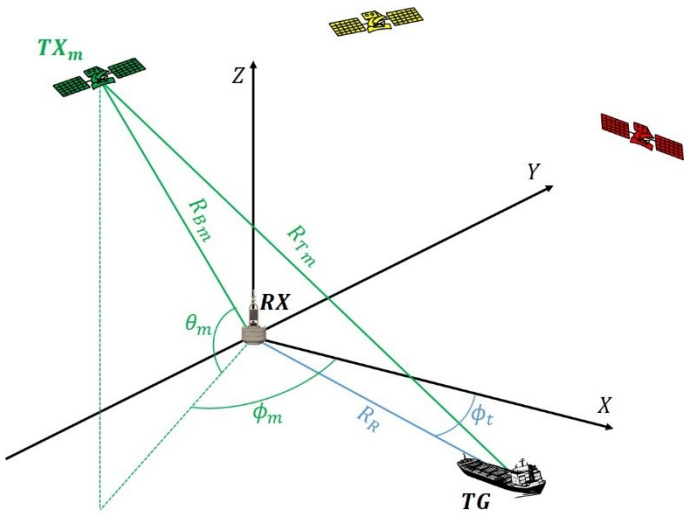

Figure 3.2 - System geometry

Since in the passive radar systems range compression is achieved by matched filtering with a reference signal compensating the instantaneous delay between transmitter and receiver, the bistatic range history of the target is given by

$$R_m(u) = R_{T_m}(u) + R_R(u) - R_{B_m}(u) \tag{3.2}$$

and its Doppler frequency is obtained as

$$\mathrm{f_{d_m}}(u) = -\frac{1}{\lambda}\dot{R}_m(u) \tag{3.3}$$

being λ the central wavelength associated to the exploited signal.

In case a scenario comprising a single GNSS transmitter and a stationary receiver is considered, the eq. (3.6) and (3.7) become:

$$R(u) = R_T(u) + R_R(u) - R_B(u) \tag{3.4}$$

$$\mathrm{f_d}(u) = -\frac{1}{\lambda}\dot{R}(u) \tag{3.5}$$

3.2 System link budget

A basic performance analysis is included here to highlight some key characteristics of the considered system. Particularly, performance is investigated in terms of achievable maximum radar range as a function of the overall available dwell time for assigned false alarm rate and detection probability levels. The analysis is carried out under the following assumptions, [26]; (i) noise limited performance; (ii) input signal to noise power ratio value does not change in the considered observation time; (iii) Swerling 0 target model.

Concerning the target model, it is worth to recall that the Swerling 0 indicates a constant target cross section not fluctuating inside the considered dwell time, which is a bold assumption. However, for performance evaluation, the dwell time is divided in N frames of duration T_f: coherent integration is assumed inside the single frame while non-coherent integration is considered among the N frames. This implies that target radar cross section (RCS) needs to be constant inside the frame while frame-to-frame variations can be tolerated. Since Swerling II performance is close to Swerling 0 when integrating a high number of measurements, the derived performance can be regarded also as representative of situations involving a fluctuating target cross section whose amplitude follows a Rayleigh distribution with rate of change in the same order of frame duration.

$(SNR)_{NCI}$ denotes the signal to noise power ratio (SNR) required to achieve a specific detection probability P_d given a desired false alarm rate P_{fa} when N frames are non-coherently integrated: the signal to noise power ratio at the single frame level, SNR_f, needed to achieve the desired performance is related to $(SNR)_{NCI}$ by

$$(SNR)_{NCI} = SNR_f \cdot I(N) \tag{3.6}$$

where $I(N)$ is the non-coherent integration improvement factor. For the square-law detector, $I(N)$ can be approximate by means of the following empirical formula

$$I(N)|_{dB} = 6.79(1 + 0.253P_d)\left[1 + \frac{log_{10}(1/P_{fa})}{46.6}\right] \cdot (log_{10}N)(1 - 0.14log_{10}N + 0.0183log_{10}^2N) \quad (3.7)$$

which is accurate to within about 0.8 dB over a range of about 1 to 100 for N, 0.5 to 0.999 for P_d and 10^{-10} to 10^{-2} for P_{fa}, [56].

The value of the signal to noise power ratio for the non-fluctuating target detection problem to achieve the desired P_d and P_{fa} can be evaluated by means of the Albersheim's equation, [57]

$$SNR_f = A + 0.12AB + 1.7B$$
$$where\ A = ln\frac{0.62}{P_{fa}}, \qquad B = ln\frac{P_D}{1 - P_D} \quad (3.8)$$

Finally, the signal to noise power ratio at frame level can be evaluated as

$$SNR_f = SNR_{input} \cdot T_f B \quad (3.9)$$

where SNR_{input} is defined as $SNR_{input} = \frac{P_{Rx}}{P_{Noise}}$ being $P_{Rx} = \frac{P_{DenGnd} \cdot \sigma}{4\pi R_2^2 L} A_{Rx}$ the power of the target returns and $P_{Noise} = kT_0FB$ the disturbance noise power. In the previous relations: P_{DenGnd} represents the power density reaching the target (W/m^2) evaluated from the minimum power level received on the ground by a 0 dBi receiving antenna as specified by Galileo standard, [7], σ the target radar cross section, A_{Rx} the effective area of the surveillance antenna, L the system losses, k the Boltzman constant, T_0 the standard temperature, F the receiver noise figure and B the exploited bandwidth. Figure 3.3 shows the maximum radar range for $P_{fa} = 10^{-3}$ and P_d=0.75 as a function of the overall dwell time for a target with 30 dBm^2 RCS and for two values of the frame duration T_f (T_f=1 sec, so that a maximum of 50 frames are non-coherently integrated, and T_f=5 sec, so that a maximum of 10 frames are integrated), for a receiving system whose parameters are similar to those used for experimentation (section 4.3) and are reported in Table 3.I. From the figure, it can be verified that the achievement of appreciable performance generally requires

the integration of the target returns over long time intervals up to several tens of seconds. Obviously, such integration requires the definition of suitable target models introduced in the following section.

TABLE 3.I - RECEIVER SYSTEM PARAMETERS

Parameter	Value	unit
Surveillance antenna area	0.195	m^2
Antenna aperture efficiency	0.7	-
Noise figure	1.5	dB
Operating bandwidth	10.230	MHz
System losses	2	dB

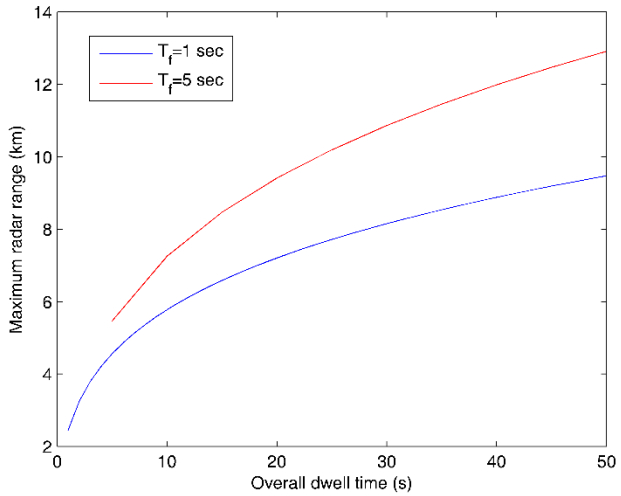

Figure 3.3 - Maximum radar range as a function of overall integration time.

3.3 Target model and time constraints

Aiming at performing an integration of the received data for detection purposes, it is of interest to analyze the impact of target motion on the target phase history to analytically derive the time constraints for selecting an appropriate model

for the received signal phase. To this purpose, the phase of the received signal is approximated in Taylor series (around $t = 0$) as follows

$$\phi(t) \approx -\frac{2\pi}{\lambda}\left\{R(0) + \alpha t + \frac{1}{2}\beta t^2 + \frac{1}{6}\gamma t^3 + \frac{1}{24}\delta t^4\right\} \tag{3.10}$$

where the coefficients α, β, γ, δ can be expressed as a function of the kinematic parameters described above (section 3.1). Based on the criterion that higher order terms of the phase can be neglected if they give rise to a phase variation during the coherent processing interval less than $\pi/4$, two fundamental constraints can be derived related to T_{lin} and T_{quad}. The former defines the maximum CPI for which the phase in eq. (3.10) can be considered as linear: since this infers a constant Doppler frequency, for CPI values lower than T_{lin}, the coherent integration can be realized by means of a Fourier Transform; the latter defines the maximum CPI for which the phase in eq. (3.10) can be considered as quadratic: if the inequalities $T_{lin} < CPI < T_{quad}$ hold, in the coherent integration the Doppler rate has to be compensated by means of dechirping-like methods. For CPI values greater than T_{quad}, more sophisticated phase compensation methods should be taken into account. Nevertheless, as it will be shown ahead, T_{quad} is often greater than values of common interest for the CPI in most practical situations. In order to evaluate T_{lin} and T_{quad}, the upper bounds T_2, T_3 and T_4 related to second, third and fourth order terms are firstly derived as

$$\begin{aligned}
&\frac{2\pi}{\lambda}|\beta|\frac{t^2}{2}\Big|_{t=\frac{T_2}{2}} \le \frac{\pi}{4} \quad \rightarrow \quad T_2 = \sqrt{\frac{\lambda}{|\beta|}} \\
&\frac{4\pi}{\lambda}|\gamma|\frac{t^3}{6}\Big|_{t=\frac{T_3}{2}} \le \frac{\pi}{4} \rightarrow \quad T_3 = \sqrt[3]{\frac{3\lambda}{|\gamma|}} \\
&\frac{2\pi}{\lambda}|\delta|\frac{t^4}{24}\Big|_{t=\frac{T_4}{2}} \le \frac{\pi}{4} \quad \rightarrow \quad T_4 = \sqrt[4]{\frac{48\lambda}{|\delta|}}
\end{aligned} \tag{3.11}$$

Accounting for typical operating conditions, it is considered that order terms higher than the quartic one give rise to negligible phase variations. Also, as it will be shown further, in every practical situation it always results in $T_2 < (T_3, T_4)$, whereas depending on target position and velocity, it may result in $T_3 > T_4$ or the other way; therefore, we can write

$$T_{lin} = T_2$$
$$T_{quad} = \min[T_3, T_4] \tag{3.12}$$

Table 3.II shows the values of T_{lin} and T_{quad} as a function of the target distance (from RX) at aperture center for different constant target velocities and directions θ (measured clockwise from y-axis), thus referring to the case of a not maneuvering target such as a ship in open sea. For the shown results the same configuration of TX-RX described in section 4.2 has been used. From Table 3.II it can be observed that:

- Strict limitations on T_{lin} (and T_{quad}) arise for those targets having a not negligible cross-range velocity component (with respect to receiver LOS) while for targets moving radially a linear approximation suffices;
- The constraints become more strict as the target speed increases and the distance from the receiver decreases;
- The linear approximation could be not sufficient to allow the coherent integration of the target returns over a time interval of few seconds that requires a second order approximation.

The above constraints will be used in the following to set the CPI value used in both single-channel and multi-channel maritime moving target detection techniques.

TABLE 3.II - ANALYSIS OF CONSTRAINTS ON THE CPI

target distance		200 m		500 m		1000 m		2000 m	
target velocity		T_{lin}	T_{quad}	T_{lin}	T_{quad}	T_{lin}	T_{quad}	T_{lin}	T_{quad}
5 kn	$\theta = 0°$	2.75	29.38	4.3	58.41	5.95	98.24	8.09	>100
	$\theta = 45°$	3.87	11.92	6	21.93	8.23	34.9	10.96	55.52
	$\theta = 90°$	61.9	>100	60.73	>100	58.94	>100	55.8	>100
10 kn	$\theta = 0°$	1.38	14.69	2.17	29.21	3.04	49.12	4.21	82.61
	$\theta = 45°$	1.95	5.961	3.05	10.98	4.24	17.43	5.82	27.69
	$\theta = 90°$	43.96	>100	43.54	>100	42.86	>100	41.6	>100
20 kn	$\theta = 0°$	0.7	7.3	1.09	14.06	1.54	24.56	2.15	41.3
	$\theta = 45°$	0.98	2.98	1.54	5.5	2.16	8.72	3	13.84
	$\theta = 90°$	31.06	>100	30.91	>100	30.67	>100	30.2	>100

Chapter 4

Single-channel M-MTD techniques

It is well known that long integration time allow to increase the detection performance either for weak and/or manoeuvring targets or in case of radar with limited power budget. The main problem considering a long time is the target migration through the resolution cells. In the literature, different algorithms have been defined for active radar systems for long non-coherent integration times, such as Hough transform (HT) [58]-[60]. Whereas, other techniques contributes to the purpose of long dwell coherent integration, such as Keystone transform (KT) [61] or the multistage algorithm proposed in [62] that successively estimates unknown target phase components. In order to reduce the complexity of a long integration, the coherent and non-coherent integration have been jointly considered in [63] by dividing the entire dwell time. In the field of passive radar, some techniques able to compensate target migration have been developed [64]-[66] in order to increase the coherent integration time.

In this chapter, the need of very long integration times (in the order of several tens of seconds) for detection purposes in GNSS-based passive radar is demonstrated and a new technique able to integrate the target returns over long time intervals is presented. To cope with the long integration time, the technique adopts a multistage approach comprising a coherent integration inside shorter intervals (named frames) and a non-coherent integration of the frames in the

integration window, and compensates the target migration at both intra-frame and inter-frames level. The adaptation to the unknown target motion conditions is obtained by resorting to proper banks, being each branch in bank matched to a specific motion: to allow the design of the bank, specific criteria are analytically derived and provided. The performance of the proposed technique is first investigated from a theoretical point: specific focus is on the analysis of the achievable integration gain and of the behaviour with respect to the ambiguous detections due to the use of the bank. To support the theoretical investigations, results from experimental campaigns are reported and discussed as well. As such, reported results aim at showing the relative improvement in SNR and detection range between conventional, short integration time techniques and the one proposed here, rather than the absolute SNR and detection range expected from a GNSS-based radar system employing the proposed technique. In the same sense, the algorithm described here are not only applicable to GNSS but to any bistatic radar system with a restricted power budget. In this frame, two experimental trials have been conducted: the first one (using GLONASS transmitter) involved a small cooperative fishing boat equipped with GPS to provide an accurate reference ground truth for performance analysis and comparison; the second one (using Galileo transmitter) involved multiple opportunity targets with different size following arbitrary trajectories with reference ground truth provided by the AIS (Automatic Identification System) receiver used in the acquisitions. Obtained results against experimental data prove the feasibility of the conceived system and the effectiveness of the proposed technique.

4.1 Basic plane-based technique

The complete processing chain, sketched in Figure 4.1, aims at performing the integration over the full time aperture T_a and provides at the output the detection map. Since the interval T_a can be quite long (i.e. tens of seconds), a multistage approach is chosen comprising a coherent integration inside shorter intervals of

duration T_f (here named frame and therefore representing the CPI) and a non-coherent integration of the N (N=T_a/T_f) frames. The overall processing comprises the following main stages:

1. Signal Synchronization, which tracks the parameters of the exploited direct signal to allow the regeneration of a noise-free replica of the reference signal to be used for range compression, [36].
2. Range matched filtering, which compresses the surveillance signal, [26]. Despite the received reference and surveillance signals are continuous in time, they are formatted according to an equivalent fast-time τ/slow time u scheme, accounting for a fictitious pulse repetition interval PRI that can be matched to the GNSS primary code length. The range-compressed data in the (τ, u) domain can be written as

$$s_{rc}(\tau, u) = \Lambda[\tau - R(u)/c] \cdot \exp\{j[2\pi f_d(u)\tau + \varphi(u)]\} \quad (4.1)$$

where $\tau \in [0, PRI]$ and $u \in \left[-{}^{T_a}/_2, {}^{T_a}/_2\right]$, $\Lambda(\cdot)$ is the cross correlation function between the reference and surveillance signal and $R(u)/c$, $f_d(u)$ and $\varphi(u)$ are the instantaneous difference between direct and reflected signals in terms of delay, Doppler and phase. A comment is in order concerning the mixed phase term $2\pi f_d(u)\tau$: being the reference and surveillance signals continuous in time, the aforementioned term accounts for the motion of the target during the single PRI. However, this term can be neglected considering the low values of typical Doppler frequencies of maritime targets and involved PRI.

3. Target integration, which receives as input the range-compressed data and provides in output an integrated map related to the entire dwell time T_a where the target can be likely detected thanks to the recovery of a suitable signal energy. The integration stage includes two main steps:

a. Compensated RD maps formation: this step receives as input the range compressed signal and provides as output the sequence of the N maps, $\boldsymbol{RD}_n^{TMC}$ n=-

N/2,…,N/2-1, after target motion compensation (TMC). Each compensated map coherently integrates the contributions from the target over an interval equal to T_f after correcting for target migration occurring inside the frame due to target motion. Moreover, inter-frames migration is also compensated in this step so that the same target is located in the same position in the sequence of the N_f maps.

b. Compensated RD maps integration: thanks to the previous step, the target returns can be properly integrated thus obtaining the final integrated map, i.e.

$$\boldsymbol{RD}^{INT} = \frac{1}{N}\sum_{n}|\boldsymbol{RD}_n^{TMC}|^2 \tag{4.2}$$

Thanks to the integration processing gain, the moving target can likely compete with the disturbance contributions and therefore be detected, by applying a 2D CA-CFAR (Cell Averaging Constant False Alarm Rate) detector.

4. 2D CA-CFAR and clustering, which receives in input the RD map and provides in output the detection map. The 2D CA-CFAR (Cell Averaging Constant False Alarm Rate) and two clustering stages (intra branch clustering and inter-branches clustering) necessary to obtain the final detection map are detailed in the following.

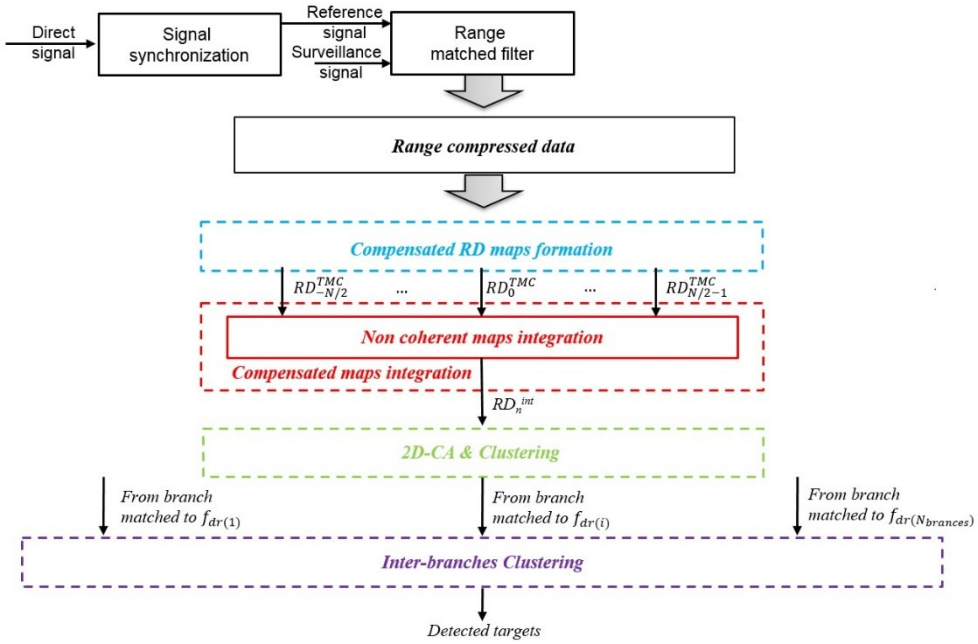

Figure 4.1 - Overall processing chain.

4.1.1 Long Time Range-Doppler technique

The technique is developed under the assumption that a linear approximation of the Doppler history suffices, according to an unknown slope represented by the Doppler rate. Based on the analysis in section 3.3, this assumption is reasonable for integration times up to some tens-one hundred seconds.

TMC works directly on the data strip obtained by selecting the proper slow-time interval of duration T_f:

$$s_{rc}^{n}(\tau, u) = s_{rc}(\tau, u) \cdot rect_{T_f}(u - u_n) \tag{4.3}$$

In this case, Doppler migration can occur both inside the single frame and through the frames. Specifically, Doppler migration inside the frame is described by the law

$$\delta f_d^n(f_{dr}, u) = f_{dr} \cdot (u - u_n) \cdot rect_{T_f}(u - u_n) \tag{4.4}$$

while the Doppler migration from the n-th frame to the reference one (n=0) can be written as

$$\Delta f_d^n(f_{dr}) = f_d^n - f_d^0 = f_{dr} n T_f \tag{4.5}$$

f_{dr} being the Doppler rate of the target corresponding to motion condition of interest. Due to the coarse range resolution, range migration is assumed occurring only among the frames and (after compensation of Doppler migration) described by

$$\Delta R^n(f_d, f_{dr}) = R^n - R^0 = -\lambda \left[f_d n T_f + f_{dr} \frac{(nT_f)^2}{2} \right] \tag{4.6}$$

Therefore, Doppler migration is corrected in the (range R, slow-time u) domain by multiplying by a phase term comprising both sources of migration in (4.4) and (4.5), whereas range migration is compensated by multiplying the n-th map in the (range frequency f_r, Doppler frequency f_d) domain for a phase term according to (4.6). Following the previous description, the "compensated RD maps formation" block in *Figure 4.1* is detailed in Figure 4.2. This provides a set of N range Doppler compensated maps ($\boldsymbol{RD}_n^{TMC}$) where targets moving according to the condition under test have been correctly aligned to their range-Doppler position occupied at the reference time instant. The N maps resulting from TMC are non-coherently integrated (to reduce the fluctuations of the disturbance background) thus obtaining the final integrated map.

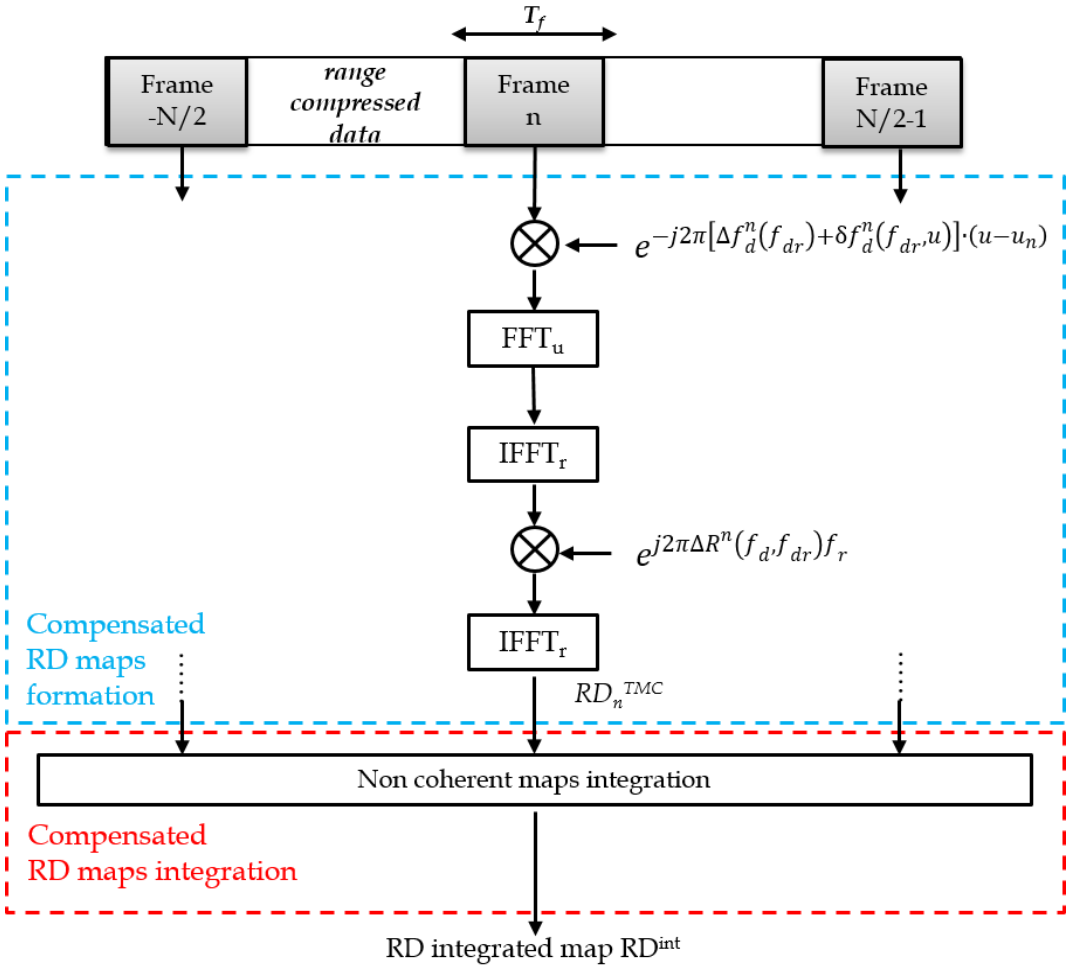

Figure 4.2 - Basic plane target motion compensated map formation technique.

4.1.2 Filters bank design criteria

As it has been already underlined, it should be pointed out that the procedure described above depends on the unknown target motion parameters. In particular, the presented techniques will provide in output a set of $\boldsymbol{RD}^{INT}(r, f_d; f_{dr})$, one for each tested Doppler rate. Therefore, a completely adaptive technique is obtained by resorting to a filter bank performing the formation of the compensated maps according to specific sets of values. Suitable criteria for the sampling of the Doppler rate axis needs to be defined. Particularly, for sake of simplicity, a target moving at

almost constant speed is here considered: this simplifying hypothesis appears reasonable for not maneuvering targets such as ships sailing at cruising speed. Nevertheless, the proposed approach could be easily generalized to cope with different situations.

The bounds on the spanned interval $[-f_{dr_{max}}, +f_{dr_{max}}]$ can be set according to the maximum considered Doppler rate (for example corresponding to a target at the minimum distance moving at the highest tangential speed); the sampling step over this interval has to assure a residual Doppler variation between the center and the extreme of the dwell time below $1/(2T_f)$: this results in a constraint given by:

$$\delta f_{dr} \leq \frac{1}{N_f T_f^2} \tag{4.7}$$

providing a uniform sampling.

4.1.3 2D CA-CFAR and clustering

The 2D CA-CFAR detector is applied using a sliding window centred around the cell under test, CUT, as sketched in Figure 4.3. M cells of the window, indicated as background ring in Figure 4.3, are used to estimate the test statistic $\hat{I}$ that is multiplied by a constant gain G to obtain the adaptive detection threshold $\lambda_{CA} = G \cdot \hat{I}$. A small guard ring is left around the CUT to avoid extended targets contributing to the test statistic. G value is set according to the desired value of false alarm rate. Detection is assessed if the intensity in the CUT, $I(CUT) = RD(CUT)$, is greater than the threshold λ_{CA}. For the CA technique the test statistic $\hat{I}$ is the mean of the intensities of the M reference cells in the background ring. Size of background ring and of guard ring are specified in terms of number of (range and Doppler) resolution cells.

The 2D-CA is followed by a clustering stage (intra branch clustering) which extracts the Regions Of Interest (ROIs) from the detected map while discarding false targets. To this purpose the clustering stage identifies all the connected components

(i.e. segments) in the binary image returned by the 2D-CA and removes isolated detected pixels due to false alarms. This step provides in output a list of targets detected at f_{dr} specified of the bank as above characterized in terms of Range-Doppler position and intensity peak value.

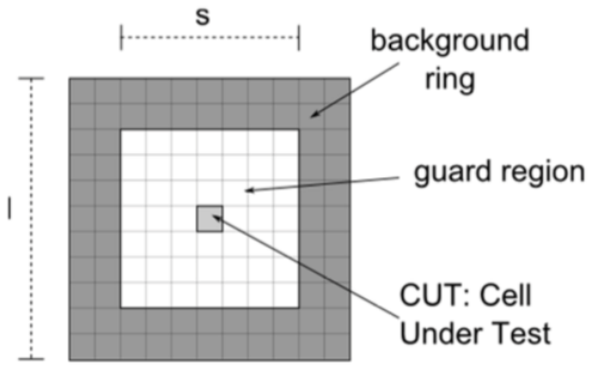

Figure 4.3 - Scheme of the sliding window used for the CA technique.

The output of this stage are the detected maps obtained for each branch of the Doppler rate bank. The obtained maps are provided in input to the inter-branches clustering in order to fuse results coming from different branches in the final detection map. To this purpose this stage has to maintain the targets detected at their actual Doppler rate value while at the same time rejecting the associated ghosts namely those detections coming from an actual target but detected at the wrong branch. Particularly the accomplishment of the migration correction driven by a wrong value of the Doppler rate, as it will be explained more in detail in the section 4.2, entails that:

- Doppler migration inside the batch is not correctly compensated;
- Doppler and range migration among the batches are not correctly corrected.

The former effect entails a blurring effect at the single RD map formation level, whereas the latter results in different positions of the target in the $\boldsymbol{RD}_n^{TMC}$ maps.

In the final integrated map the target energy is spread in over multiple resolution cells in an area of deterministic shape (section 4.2) around the actual

target position. This deterministic shape of the ghosts is exploited by the post detection logic for ghosts removal.

4.2 Theoretical performance analysis

The effectiveness of the proposed detection technique is tested and demonstrated in this section against synthetic data: main satellite and processing parameters are listed in Table 4.I while receiver parameters are as in Table 3.I. A satellite of the Galileo constellation has been considered as transmitter of opportunity, whose estimated trajectory was obtained from a GNSS satellite tracking website [67]. A ship navigating in the field of view of the surveillance antenna is considered, with position $\boldsymbol{TG^0} = (1200m, 100m, 0m)$ at the reference time, moving at a velocity of 10 kn with heading 45° with respect to the x direction, corresponding to a bistatic range and Doppler position equal to 1493 m and -16.33 Hz. The target RCS has been set equal to 100 m^2. Concerning the disturbance background, the noise is assumed white Gaussian according to parameters in Table 3.I. Therefore, not any strategy for suppression of sea clutter has been taken into account here. This follows from the assumption that the system is mainly noise-limited rather than clutter-limited, as a consequence of: i) the restricted power budget provided by GNSS; ii) the long dwells considered, acting as a whitening filter with respect to the background distribution. It could be shown that such a hypothesis is well in line with the experimental datasets collected during the field trials whose results are presented in the next section. In addition, possible interfering e.m. sources have been neglected taking into account that i) signals that do not match with the Pseudo Random Noise (PRN) code of the useful signal will be discarded during the matched filtering and ii) the proposed long integration time techniques are expected to spread possible interference over multiple resolution cells.

TABLE 4.I - SATELLITE AND PROCESSING PARAMETERS

Parameter		Value	unit
Satellite	Satellite number	GSAT0103	-
	Ranging code	PRN19 (E5a-Q primary code)	-
	Satellite azimuth (relevant to North)	61.6~62.1	deg
	Satellite elevation (relevant to receiver)	70.7~70.8	deg
	Power density at ground level	-135	dBW/m^2
Processing parameters	Sampling frequency	50	MHz
	Equivalent pulse repetition interval	1	ms
	Central frequency	1176.450	MHz
	Operating bandwidth	10.230	MHz
	Dwell time	30	s

First, let us consider a conventional approach to detect the moving target consisting in looking for the peak in the RD map obtained over a short CPI. After the range-compression has been performed, we could select a time interval around the reference time of the acquisition short enough to ensure that the target reflectivity is constant and migration negligible. By means of a slow-time FFT, the corresponding RD map is achieved. As examples, Figure 4.4 shows the obtained results for intervals durations equal to 1 s and 3 s. In the figures, 0 dB represents the mean noise background power level and the black star markers denote the target range and Doppler actual location. As it is apparent, it is not possible to individuate any bright spot that can be associated to the target. Namely, the coherent integration gain achieved over limited time windows did not suffice to detect the target. The results obtained by using the proposed long integration time technique are provided in two cases: in the former, T_f=1 s and N = 30 frames are non-coherently integrated; in the latter, T_f=3 s and N = 10 frames are non-coherently integrated. For each value of Doppler rate under test, the $\boldsymbol{RD}^{INT}(R, f_d; f_{dr})$ map is obtained according to the selected frame duration. Figure 4.5 shows the integrated RD maps

when the TMC has been accomplished using the actual target Doppler rate (equal to 0.0395 Hz/s). We can observe that the technique allowed retrieving a suitable signal to disturbance power ratio to isolate the target from the background. These maps can be compared with the short time RD maps shown in Figure 4.4: the integration of multiple RD maps, along with the TMC according to the actual Doppler rate, can enable the detection of the target otherwise inhibited in the single RD maps. Figure 4.6 shows the range and Doppler cuts around the peak position, along with the curve resulting from the integration performed skipping the TMC procedure (blue dotted line). We can observe that also for this technique the TMC represents a mandatory step to correctly concentrate the target energy during long dwells. In addition, as before, higher SNR and better Doppler resolution are achieved considering longer coherent processing intervals.

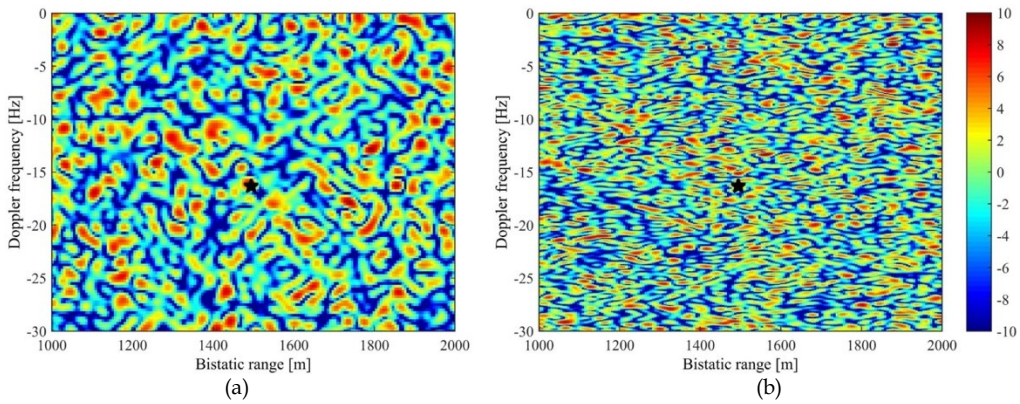

Figure 4.4 - RD maps obtained over individual CPIs – a) CPI = 1s, b) CPI = 3s.

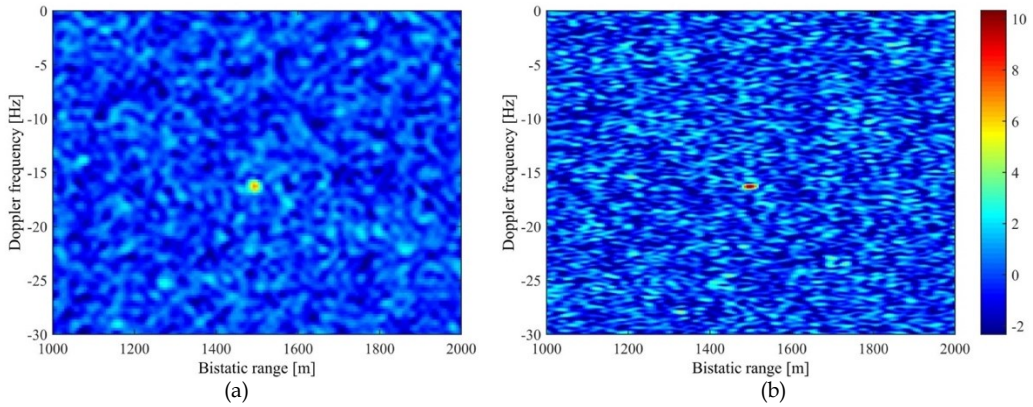

Figure 4.5 - Integrated RD map for the actual Doppler rate – a) T_f = 1 s, b) T_f = 3 s.

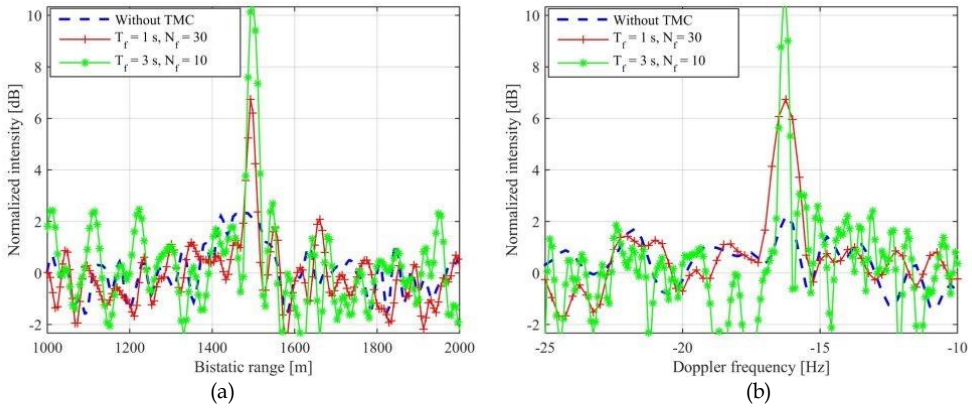

Figure 4.6 - Cross-sections around the actual target position – a) Bistatic range cross-section, b) Doppler cross-section.

An analysis in noise-free background is now provided to show clearly the effect of TMC accomplished according to different Doppler rate values. The unknown target Doppler rate make necessary to inspect all the $\boldsymbol{RD}^{INT}$ maps pertaining different Doppler rates. Despite values of the Doppler rates different from the actual one result in a perturbed TMC, depending on the particular conditions, detections could occur in more $\boldsymbol{RD}^{INT}$ maps pertaining different Doppler rates. Figure 4.7 shows $\boldsymbol{RD}^{INT}$ maps obtained for five different values of the Doppler rate. As for the previous analysis, these maps have been obtained in noise-free conditions and 0 dB represents the highest intensity value, which has

been obtained for the map pertaining the actual Doppler rate reported in Figure 4.7 (a). The accomplishment of the TMC procedure driven by a wrong value of the Doppler rate entails that i) Doppler migration inside the frame is not correctly compensated, from eq. (4.4), ii) Doppler and range migration from the n-th to the reference frame are not correctly corrected, from eqs. (4.5) and (4.6). The former effect entails a blurring effect at the single compensated map formation level, whereas the latter results in different positions of the target in the $\boldsymbol{RD}_n^{TMC}$ maps so that in the final integrated map a further blurring effect can be observed (see Figure 4.7 (b-e)), with the energy spread over multiple cells. The black dotted rectangle in the figure highlights the area of the basic plane where the target energy can be spread. This can be obtained by evaluating the maximum co-registration errors in range and Doppler position obtained at the border of the processed dwell time and respectively equal to $\frac{|f_{dr}-f_{dr}^o|T_a^2\lambda}{8}$ and $|f_{dr}-f_{dr}^o|T_a/2$ being in this case f_{dr}^o the actual target Doppler rate and f_{dr} the generic value used by the technique.

The ghosts generated are located around the actual target position. This characteristic, combined with the deterministic shape of the ghost, could be exploited by a proper post detection logic for ghost removal.

As a final comment, the technique was derived and tested considering a target undergoing translation motion only. Actually, we do not expect more complex kinematics to prevent the detection capability provided by the presented long integration time technique. If a target experiences yaw, pitch and roll along with translational motion, target will slightly spread in the range-Doppler domain around the position occupied by target fulcrum (i.e. the center of rotation). However, considering the available range resolution, the short CPIs and wavelength of GNSS waveforms (way worse than the ones usually involved in target imaging, where rotations play their major role), we expect the RD cluster of points pertaining to the target to be small, thus not preventing energy collection and consequent target detection. Indeed, it is worth noticing that the long integration

concept at the basis of the proposed techniques still holds since it adaptively compensate the translation motion thus aligning the clusters corresponding to different frames around the same position. Therefore, the aligned clusters can be non-coherently integrated, even in presence of such rotation motions, thus enabling target detection.

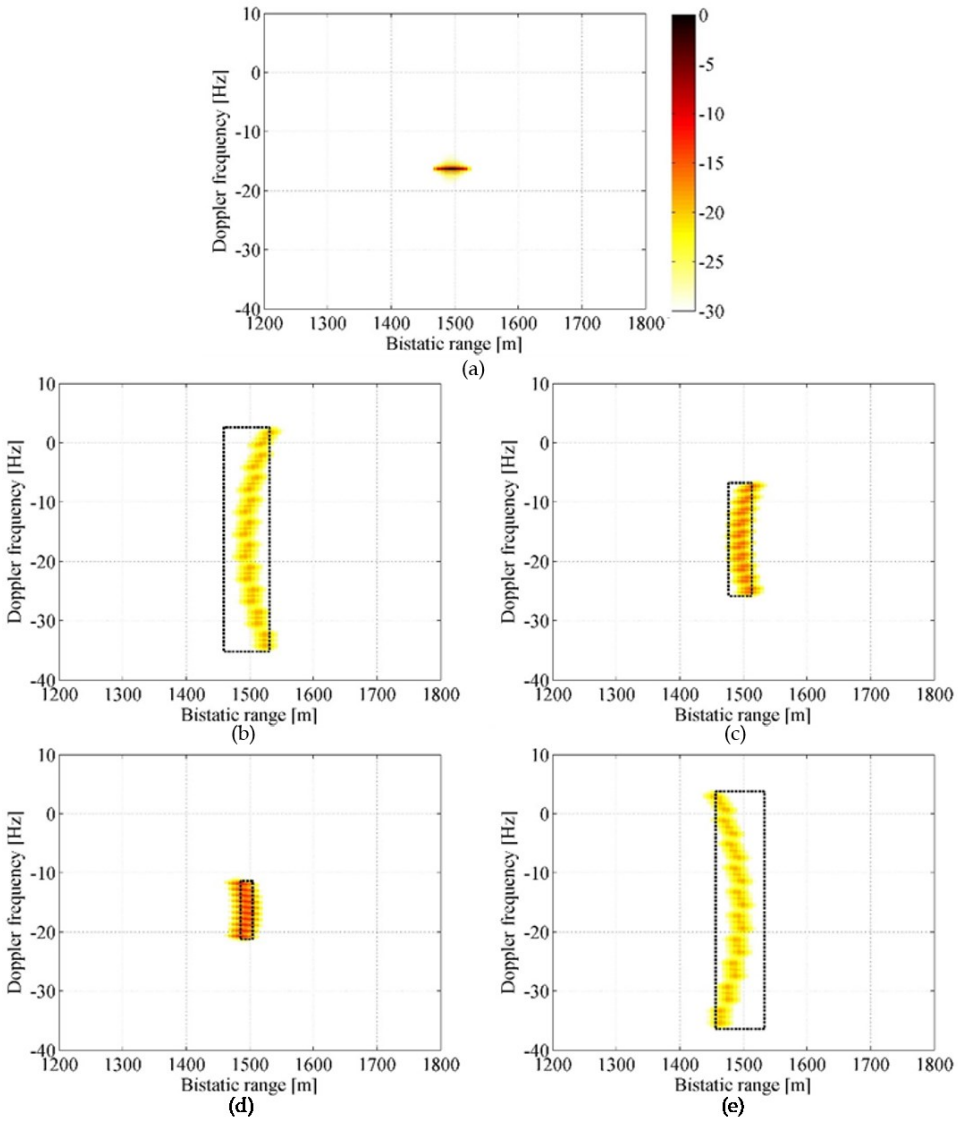

Figure 4.7 - Basic plane maps for different values of the tested Doppler rate. a) $f_{dr} = f_{dr_{TgT}}$ *=-0.0395 Hz/s; b)* f_{dr} *=-1.3000 Hz/s; c)* f_{dr} *=-0.6778 Hz/s; d)* f_{dr} *=0.2889 Hz/s; e)* f_{dr} *=1.3000 Hz/s.*

4.3 Experimental results

To prove the effectiveness of the proposed algorithm, three proof of concept measurement campaigns have been conducted inside the H2020 SpyGLASS project by means of the experimental receiver developed at University of Birmingham and shown in Figure 4.8. It should be stressed that the experimental receiver was scientific equipment, thus not specifically tailored for the type of application considered in this thesis. For this purpose, experiments were done with the receiver on the shore, and targets of substantially varying dimensions were used. Therefore, the overall purpose of these experiments was to confirm the functionality of the proposed techniques and to quantify their relative performance, rather than investigating the absolute detection performance of a GNSS-based radar system, which is a separate topic.

The receiver itself was equipped with two RF channels for recording both the direct and surveillance signals, respectively. A low gain antenna was used to record data from all available satellites feeding the reference channel and representing the direct signal for the following bistatic processing; as GNSS signals are right hand circularly polarized (RHCP), the reference antenna was RHCP. The surveillance channel acquired the weak radar signal through a high-gain antenna steered toward the surveilled area; to minimize the direct path interference, a left hand circularly polarized (LHCP) antenna was used.

Figure 4.8 - Experimental receiving hardware.

4.3.1 Experimental validation on high size target

The first experimental campaign was planned and conducted using Galileo satellites as transmitters of opportunity and the passive receiver situated at the eastern coastal area of Plymouth harbour in UK. Target of opportunity was the commercial Brittany ferry running in schedule. Figure 4.9 (a) shows the data acquisition geometry during the measurement. Figure 4.9 (b) gives a photograph of the ferry taken during experiments. The length of the ferry is approximately 184 m, and its beam is 25 m. The real track of the ferry was found in the Automatic Identification System (AIS) and used as the ground truth for comparison with the experimentally tracked results. Two satellites in view of the receiver were successfully synchronised. Their azimuths and elevations were marked in Figure 4.9 (a). The experimental parameters are shown in Table 4.II, as well as the specific parameters used for signal processing.

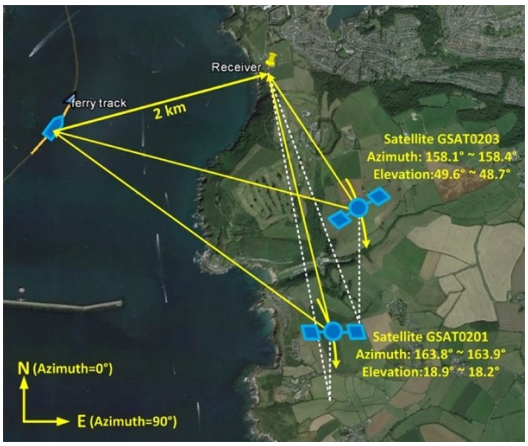

(a)

(b)

Figure 4.9 - (a) Schematic diagram of the experimental GNSS-based radar data acquisition geometry, and (b) the optical photograph of the ferry.

TABLE 4.II - EXPERIMENTAL AND SIGNAL PROCESSING PARAMETERS

Parameter		Value
Sat 1	Number	GSAT0201
	Ranging code	PRN18 (E5a-Q primary code)
	Bistatic angle	97° ~ 85°
	Azimuth (relevant to North)	163.8° ~ 163.9°
	Elevation (relevant to HC antenna)	18.9° ~ 18.2°
Sat 2	Number	GSAT0203
	Ranging code	PRN26 (E5a-Q primary code)
	Bistatic angle	91° ~ 83°
	Azimuth (relevant to North)	158.1° ~ 158.4°
	Elevation (relevant to HC antenna)	49.6° ~ 48.7°
Carrier frequency		1176.45 MHz
Sampling frequency		50 MHz
Dwell time		145 second
Pulse repetition interval		1 millisecond
Coherent processing interval		2.5 second
Non-coherent processing interval		10 second

Firstly a statistical analysis of the background noise is conducted here to verify that the system is noise-limited with Gaussian distribution, as assumed in 5.2. The analysis is performed on a RD map referring to a single frame obtained with a CPI of 3 s. The noise samples are selected on the RD map in an area without targets. The noise sample values for the phase (I) and quadrature (Q) components are compared in Figure 4.10 with a Gaussian distribution. As can be seen, the components I and Q have a zero-mean Gaussian distribution and variance related to the disturbance power. In Figure 4.11 the noise samples after square law detector are compared with an Exponential distribution. The image in logarithmic scale shows that the noise samples follow the Exponential distribution as expected.

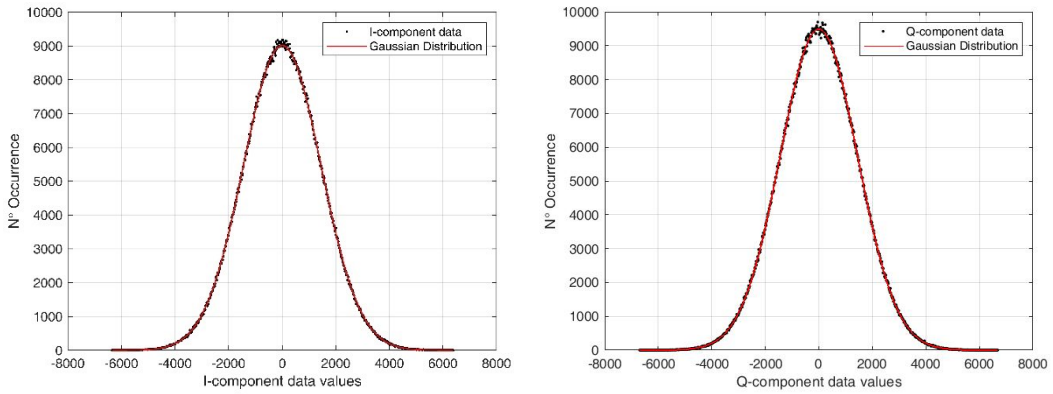

(a) (b)

Figure 4.10 - Gaussian distribution and background samples (a) I-component and (b) Q-component

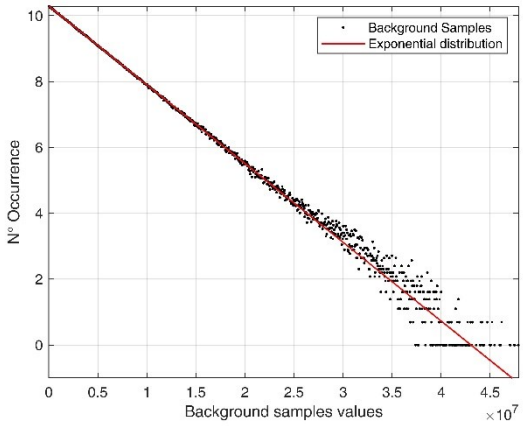

Figure 4.11 - Exponential distribution and background samples after square law detector

A further analysis is performed on the integrated RD map. After non-coherent integration, the distribution of noise samples will be a Gamma with a shape factor F equal to N. In this case the RD^{INT} map is obtained by the non-coherent integration of N=10 frames applying the TMC procedure. As evident in Figure 4.12, the Gamma distribution with shape factor F=N=10 provides a good fit with the noise samples. Therefore, it can be said that the initial hypothesis is correct.

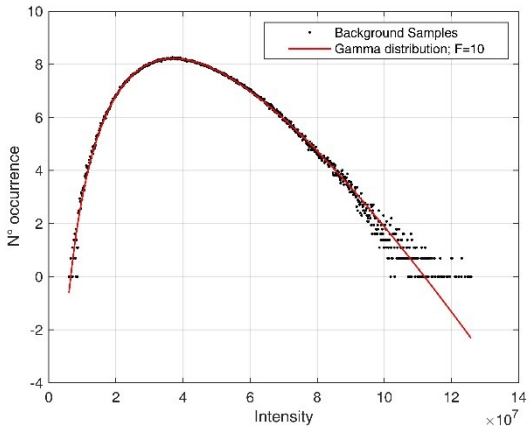

Figure 4.12 - Gamma distribution and background samples after non coherent integration of N=10 frames

Some experimental results are shown in order to validate the proposed technique. The results in Figure 4.13 are obtained selecting a data stream of 50 s centered on 60 s from start acquisition time from acquisition of satellite 2, because it provided the worst signal to background ratio i.e. better than satellite 1 to show the potentiality of the technique. Within this interval, the target Doppler frequency is no more constant, resulting in a Doppler rate different from zero.

This interval is segmented in consecutive batches 2.5 s long, and the resulting 20 RD maps are then integrated. The obtained integrated maps are shown in Figure 4.13. Maps are expressed in dB and each map has been normalized to its maximum value. Figure 4.13 (a) shows the map obtained by directly integrating the set of RD maps, i.e. by skipping the TMC step. As it is apparent, the motion of the target entailed a range and Doppler migration over the long integration time, resulting in a spread of the target energy over different range-Doppler cells of the integrated map. The map obtained by considering also the TMC and provided by the branch of the bank providing best matching with the target kinematic is shown in Figure 4.13 (b). As evident, the long time range-Doppler technique has been able to properly integrate the target contributions in the individual maps repositioning them in the same location, thus providing a higher energy concentration. This can

be well observed looking at the bottom boxes of Figure 4.13, highlighting the target position (it should be pointed out that, for sake of better visualization, the zooms have displayed with a color scale with 10 dB of dynamic normalized to the peak value of the ferry return in the TMC integrated map). As a consequence of the enhanced energy concentration provided by the TMC, a gain in terms of signal to background ratio can be obtained, as evidenced by looking at the range and Doppler cuts around the target peak position of the compensated map in Figure 4.14.

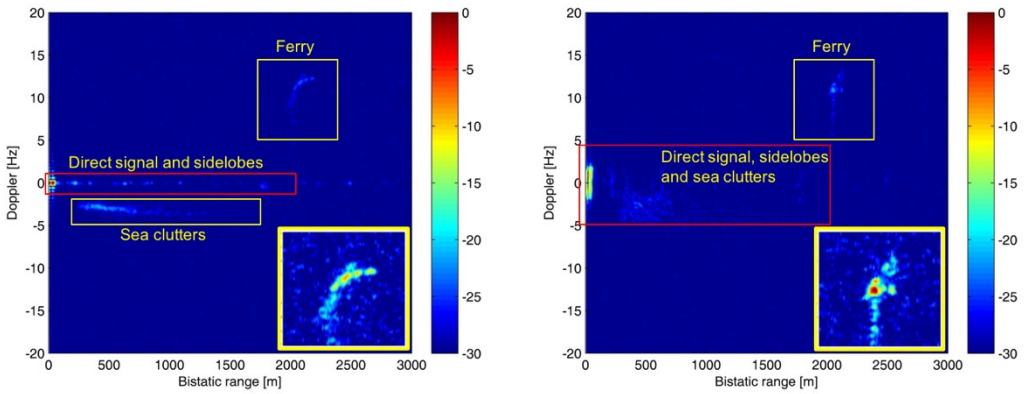

Figure 4.13 - Experimental results of satellite 2 - integration of 20 consecutive RD maps with (a) and without (b) target motion compensation, with a total data acquisition time of 50 s.

A second important benefit arising from the TMC procedure concerns the clutter. Indeed, if on one hand the Doppler rate-based processing allows building up the useful signal energy, on the other hand it reduces the amount of clutter energy per cell by spreading it over multiple cells, as it is apparent looking at the sea clutter returns highlighted in Figure 4.13 and the corresponding Doppler cuts in Figure 4.15.

Despite this specific acquisition concerns a not particularly fast target with high size and high RCS and therefore it does not strictly require a very long integration time to make the target detectable, these results show the general validity of the long time technique in this particular kind of a passive radar system.

Indeed, if targets with low RCS were acquired by the system, integration over several tens of seconds would be mandatory to obtain an improvement of SNR able to make the detection possible.

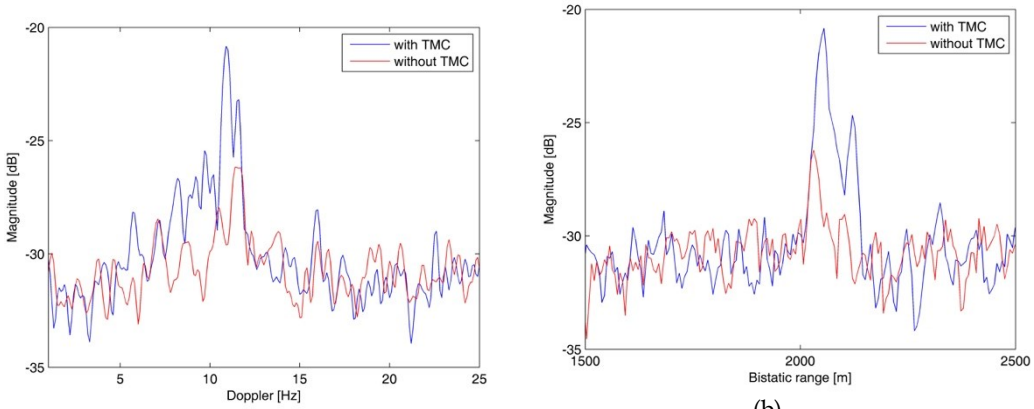

Figure 4.14 - Experimental ferry range (a) and Doppler (b) cross-sections for the long time range-Doppler technique.

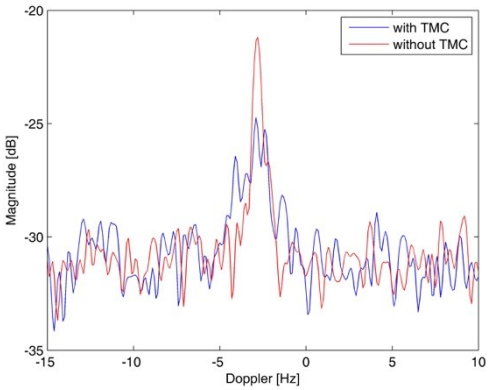

Figure 4.15 - Doppler cross-sections of the sea clutter background.

In Figure 4.13(b), the peak position moves accordingly to the real target motion. This suggests the possibility to track the target position over the available dwell time. The RD histories are obtained considering an integration window

sliding along the overall acquisition time with an interval of 1s. Each RD map is obtained by considering a CPI of 2.5 seconds. For each one, the peak position corresponding to the target is recorded as detected bistatic range and Doppler position and the red curves in Figure 4.16 and Figure 4.17 have been obtained. The detected range and Doppler history are compared with the ground truth provided by the AIS data.

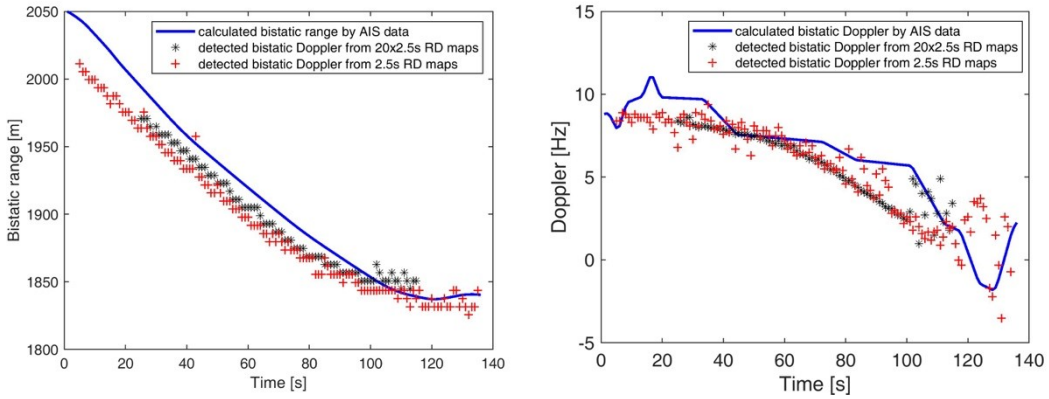

(a) (b)

Figure 4.16 - (a) Comparison of bistatic ranges for satellite 1. (b) Comparison of bistatic Doppler for satellite 1

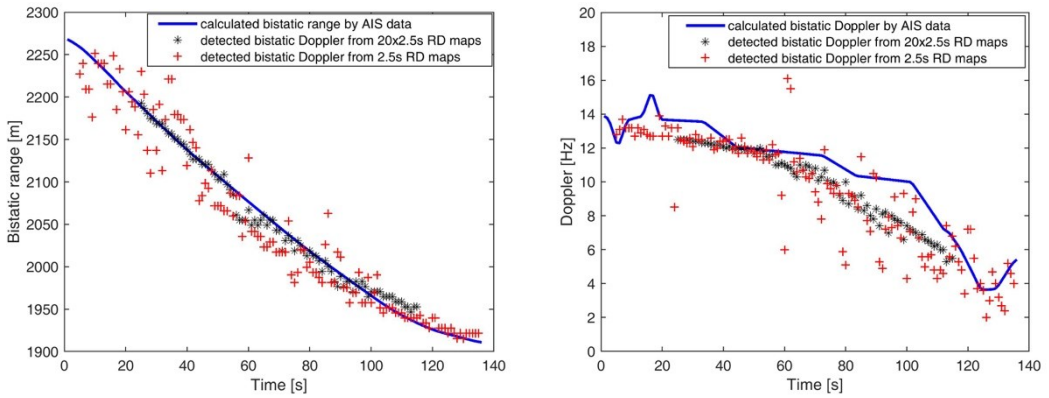

(a) (b)

Figure 4.17 - (a) Comparison of bistatic ranges for satellite 2. (b) Comparison of bistatic Doppler for satellite 2

Because of its high RCS, the considered target becomes visible above clutter level for both satellites integrating over limited observation times where, depending also on the particular target kinematic parameters, the TMC is not essential. However, when targets with lower RCS are considered, the increasing of the observation time is needed to assure super-clutter visibility conditions, and in such a case the TMC step is mandatory, as discussed in previous section. In Figure 4.16 and Figure 4.17, a second set of RD histories is shown (black curves) by considering the following processing. A time window of 50 s is considered moving along the observation time with a step of 1 s. Batches of duration 2.5 s are considered, and therefore 20 batches are integrated after the TMC procedure has been applied for each position of the time window accounting for the nominal value of the Doppler rate. Thus, 96 integrated maps are obtained for the available 145 s of dwell time. As it is apparent, the scatterer plots obtained from the long time integration technique show a lower dispersion of the target tracks than the corresponding plots resulting from the only coherent integration over short time, because of the enhanced concentration of the target energy provided by the TMC step. For this long time processing, the RMS of the range difference and Doppler difference with respect to the AIS data are respectively 13.2 m and 1.5 Hz for satellite 1 (versus 18.4 m and 1.9 Hz for the red curves when evaluated over the same time interval) and 10.6 m and 1.5 Hz for satellite 2 (versus 26.0 m and 2.6 Hz). This analysis further demonstrates the effectiveness of the long time technique to collect the signal energy over long integration times, being a mandatory condition to counteract the restricted power budget provided by GNSS. Obviously, a correct localization of the target on the ground plane could be obtained by exploiting multiple measurements made available from the exploitation of multiple satellites.

The combination of the detection maps corresponding to the different integration window of 50 s is shown in Figure 4.18. each detection map was obtained by applying the 2D CA-CFAR detector and the clustering stages.

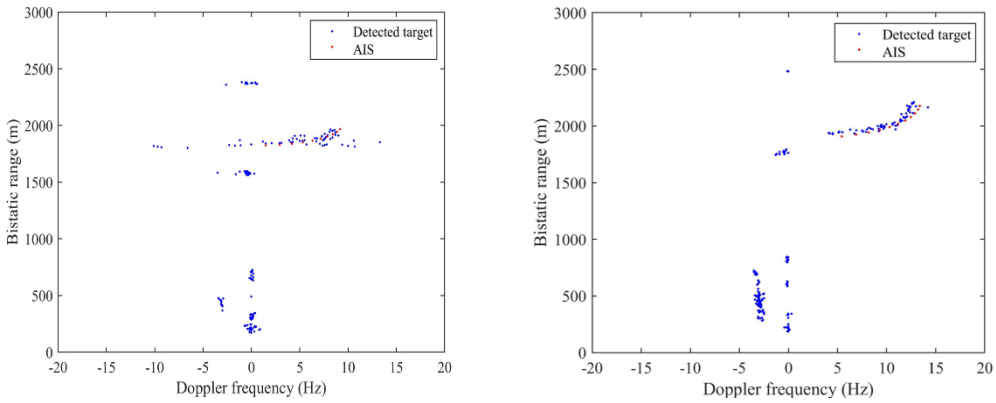

Figure 4.18 - Final detection map by applying 2D CA-CFAR (a) for satellite 1, (b) for satellite 2

4.3.2 Experimental campaign with cooperative target

The second experimental campaign was conducted near Aberystwyth (UK). GLONASS was selected as transmitter of opportunity and returns from a cooperative target was acquired, as shown in Figure 4.19 (a). This target was a small fishing boat, approximately 10 m long. Such a vessel was used in the first instance because it was possible to rent and equip it with a GPS receiver, while following a desirable trajectory on a straight line from the sea and towards the shore. This allowed us to be aware of the acquisition scenario, which is depicted in Figure 4.19 (b). The target was approaching the receiver with a velocity of about 5 kn, persisting in the main lobe of the receiver antenna for most of the acquisition time. Figure 4.19 (c) shows the recorded target speed components.

(a)

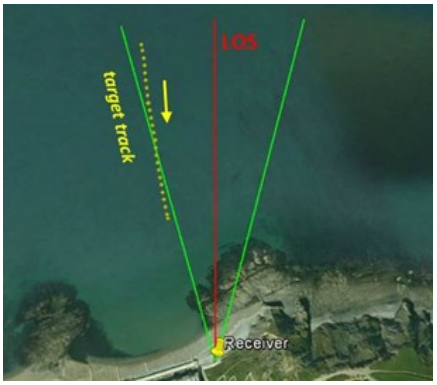

(b)

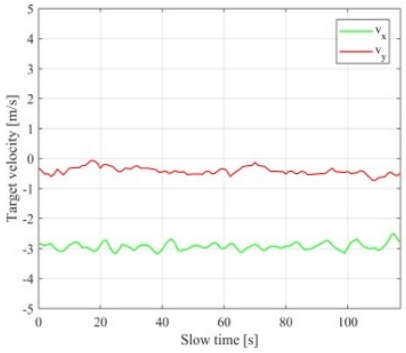

(c)

Figure 4.19 - Experimental campaign – a) cooperative target, b) acquisition geometry, c) recorded target speed.

Table 4.III shows transmitter and processing parameters. In particular starting from an acquisition length of 118 s, T_f has been set to 3 s, while the non-coherent integration time has been set to 60 s. Indeed, in this case, we foresee the necessity of long integration times and TMC, differently from the case presented in previous section, where the high RCS of the acquired ship allows it to be detectable even with short coherent integration time.

Figure 4.20 (a) shows the RD map achieved with a coherent integration of 3 s. From this figure, the presence of the direct signal well concentrated around the zero range and zero Doppler frequency position along with its side lobes can be

seen. Its cancellation along with the stationary background could be considered, [68], but here we retained it to compare it with the amplitude levels of clutter and target.

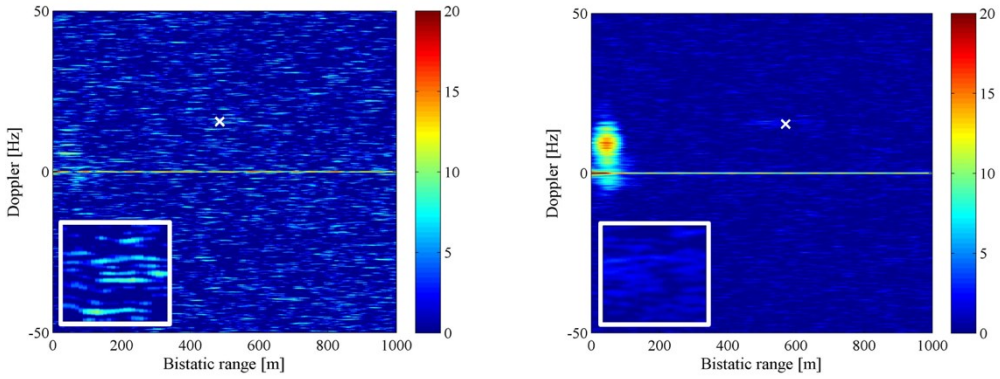

(a) (b)

Figure 4.20 - (a) Single RD map (3 sec); (b) Integration of 20 RD maps (3 sec each) without TMC.

TABLE 4.III - EXPERIMENTAL AND SIGNAL PROCESSING PARAMETERS OF THE FIRST MARITIME ACQUISITION CAMPAIGN

Parameter		Unit	Value
Satellite	number	-	732
	carrier frequency	MHz	1603.6875
	Chip rate	MHz	5.11
	azimuth (clockwise from N)	deg	3.0 ~ 6.8
	elevation (relevant to HC)	deg	73.2 ~ 73.1
Processing parameters	sampling frequency	MHz	50
	pulse repetition interval	ms	1
	dwell time	s	118
	frame duration	s	3
	non-coherent integrated frames	-	20

While a strong and well visible return is present around 50 m in range and spreading over several Doppler positions that can be related to clutter, the target return, whose actual GPS position is marked with the white '×' in the figure, is buried under the disturbance level and therefore not visible, as it is apparent from the enlargement around the true target position shown in the white box. The short CPI of 3 s does not guarantee an effective integration gain, therefore a longer integration is mandatory. The RD map resulting from the direct non-coherent integration over a longer time, but without TMC, is shown in Figure 4.20 (b) purely for visualization purposes and to compare it to the case comprising TMC. Although the disturbance fluctuations have been reduced, it is not possible to see the target return, which is an expected result since over this time the target has moved over several resolution cells.

Results obtained using long time RD technique are shown in Figure 4.21. Each image is obtained by performing a coherent integration step over 3 s frames yielding $N = 20$ motion compensated local maps that are finally non-coherent integrated. The three images are normalized to the mean disturbance level and each one corresponds to a different start time, 0 s, 30 s and 58 s for sub-figures (a), (b) and (c), respectively. Particularly Figure 4.21 shows the output of the long-time RD technique corresponding to the Doppler rate value providing the maximum SNR. As it is apparent from the zooms in the white boxes of the area around the true target position, target return is well visible above the disturbance level, implying the recovery of a SNR level suitable for detection. Moreover, the effect of a more favourable link budget is also evident as the considered start time increases: indeed, the target was approaching the radar receiver, therefore higher target power is expected as the integration window slides over the whole acquisition.

As explained before, the proposed procedure operates under the hypothesis that a second order approximation is sufficient to accurately describe the variation with time of the target distance from the radar. To verify that this hypothesis holds

in the experimental study case, the long time RD technique is performed exploiting the a priori information available from the GPS records of the target. To this purpose, in the range and Doppler frequency coregistration steps, the TMC has been performed exploiting the actual differences between the target range and Doppler frequency at the current frame time with respect to the target range and Doppler frequency at the reference time instead of the quantities shown in Figure 4.2. Figure 4.22 shows the range and Doppler frequency cuts of the target response when a priori information on the target motion is used for the integration window starting at 58 s. From a visual inspection there is a good correspondence between the target response pertaining to the proposed technique (red curves) and the ones pertaining to the exploitation of the a priori information of the target motion (blue curves), thus confirming that at least in this specific case the hypothesized motion model matches the actual target dynamics.

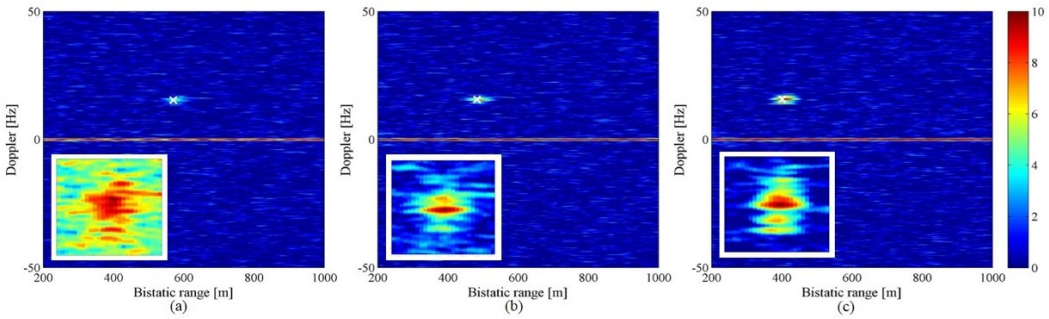

Figure 4.21 - Experimental RD integrated maps over T_a = 60 s. a) start time = 0 s, b) start time 30 s, c) start time 58 s.

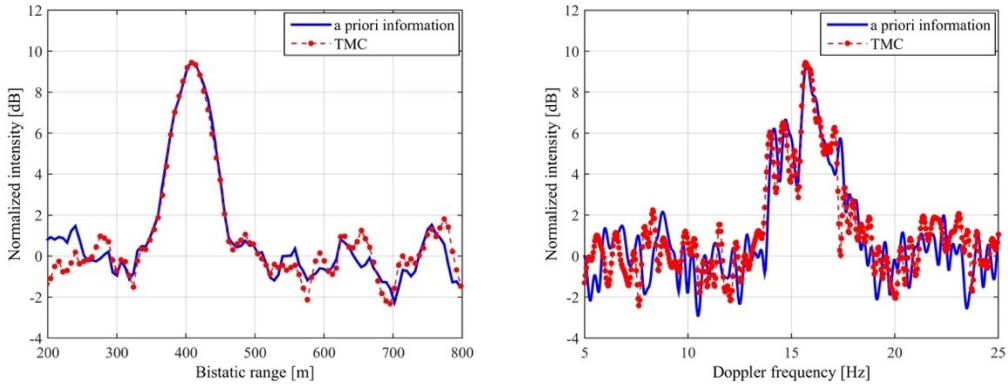

(a) (b)

Figure 4.22 - Comparison between results obtained with basic plane-based technique and GPS measurement at start time 58 s. Bistatic range (a) and Doppler frequency (b) cuts.

Above results confirm the effectiveness of the proposed techniques at collecting the signal energy over long integration times (~1 min). In order to provide a meaningful quantification of the improvement of the detection performance arising from the exploitation of the proposed long integration time techniques, the SNR obtained for an increasing number of aligned and integrated RD maps is evaluated. We recall that the non-coherent integration of the correctly aligned maps allows accumulating the target energy over the dwell time, while, in contrast, it reduces the fluctuations of the disturbance contribution. Therefore, for a given number of integrated maps, we define the level of signal to disturbance ratio as

$$SNR = \frac{P_s - P_n}{\sigma_n} \tag{4.8}$$

where P_s is the obtained signal power, P_n and σ_n are respectively the mean and the standard deviation of the disturbance background. We considered a set of $N = 19$ compensated maps aligned to the central position of the considered interval. The Doppler rate driving the alignment has been selected as the one providing the maximum signal power in the final integrated maps. Different integrated maps have been then obtained by combining $n_f = 1,3,\dots,19$ maps around the central map. For each value of n_f, P_s has been estimated as the peak

power of the range and Doppler cell corresponding to the actual target location as provided by the GPS ground truth, whereas the disturbance statistic has been evaluated by considering a window containing disturbance contributions only. In this analysis, we focus on the part of the target track most far from the receiver, with the target located at a bistatic range of 522 m at the reference position, since it provides the lower input signal power. The blue markers in *Figure 4.23* represent the estimated SNR as a function of the number of integrated maps. We point out that for $n_f < 5$ it was not possible evaluating the SNR. This is because for those cases, the high fluctuating background mixes up with the target energy, making not straightforward the evaluation of P_s. Therefore, in this specific scenario, we needed the integration of at least 5 compensated maps to clearly isolate the target from the background. The black dotted curve represents the retrieved SNR achieved by using in (4.8) the mean value of P_s (averaged over the different integrated maps where the target was clearly identifiable from the background, $n_f > 5$): the results in the figure allow us to roughly evaluate the improvement of the recovered SNR moving from a single to n_f integrated and properly aligned maps.

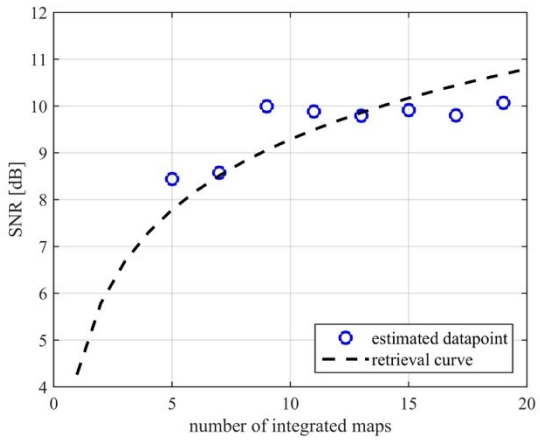

Figure 4.23 - Estimated SNR as a function of the number of integrated RD maps.

4.3.3 Experimental campaign with opportunity target

A third acquisition campaign was conducted near the Portsmouth International port (UK). Galileo satellites were exploited as transmitters of opportunity, focusing on the E5a-Q band signal. The receiving hardware was again located on the shore Figure 4.24 (a). In particular, during the trial, two opportunity targets were in the field of view of the surveillance antenna: the passenger ferry 'St Faith' (length: 77.05 m, beam: 17.2 m, draught: 2.48 m) and the catamaran 'HSC Wight Ryder I' (length: 41 m, beam: 12 m, draught: 1.60 m), of which optical photographs are shown in Figure 4.24 (b) and (c), respectively. The real tracks of these vessels were found in the Automatic Identification System (AIS) and used as the ground truth for comparison with the experimental results. The experimental and processing parameters are listed in Table 4.IV.

TABLE 4.IV - EXPERIMENTAL AND SIGNAL PROCESSING PARAMETERS OF THE SECOND MARITIME ACQUISITION CAMPAIGN

	Parameter	Unit	Value
Satellite	number	-	GSAT0202
	carrier frequency	MHz	1176.450
	Chip rate	MHz	10.230
	azimuth (clockwise from N)	deg	64.86 ~ 62.00
	elevation (relevant to HC)	deg	24.87 ~ 24.06
Processing parameters	sampling frequency	MHz	50
	pulse repetition interval	ms	1
	overall observation interval	s	286
	frame duration	s	3
	non-coherent integrated frames	-	1/5/10/20

Figure 4.25 (a) shows the combination of 95 RD maps obtained considering an integration window sliding along the overall observation interval with step of 3 s. Each RD map is obtained by considering $T_f = 3$ s and N=1; the combined RD map in Figure 4.25 (a) is obtained by assigning at each range-Doppler position the highest intensity achieved at that position for all the considered Doppler rate values and integration windows. In this figure 0 dB represents the background floor evaluated in the final map. As it is apparent, both targets are visible in this map. The near target, 'HSC Wight Ryder I', is at a bistatic range of about 620 m and the far target, 'St Faith' in the red frame, is visible until 2656 m. As evident from Figure 4.25 (a), during the overall acquisition target 'St Faith' shows a considerable variation in peak intensity: the main source of this variation is likely due to changes in the target radar cross section since the involved dynamic range cannot be explained by simply considering the attenuation related to the changing distance.

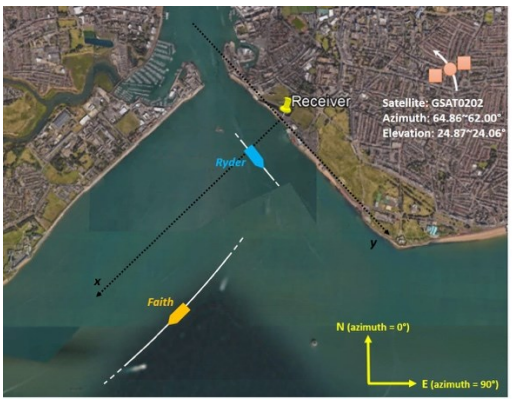

(a)

(b)

(c)

Figure 4.24 - Second maritime experimental campaign – a) acquisition geometry, b) non-cooperative target 'St Faith', c) non-cooperative target 'HSC Wight Ryder I'.

The target 'St Faith', moving towards the receiver with an almost radial motion, is chosen to demonstrate the capability of long integration time technique to improve the maximum radar range. Figure 4.25 (b), (c), (d) show the progressive improvement obtained by applying the basic plane-based technique respectively for $N = 5, 10$ and 20 and by setting again $T_f = 3$ s. As evident, the maximum detectable range increases with increasing the integration time. As an example, for the case $N = 20$, Figure 4.26 shows the final map obtained by combining the detection maps corresponding to the different integration windows. Each detection map was obtained by applying to each integrated map provided by the bank a 2D-CA-CFAR detector and by cascading a clustering stage for ambiguous detections removal. As it is apparent, the bright returns visible in Figure 4.25 (d) correspond to a track in Figure 4.26 in good agreement with the ground truth provided by AIS.

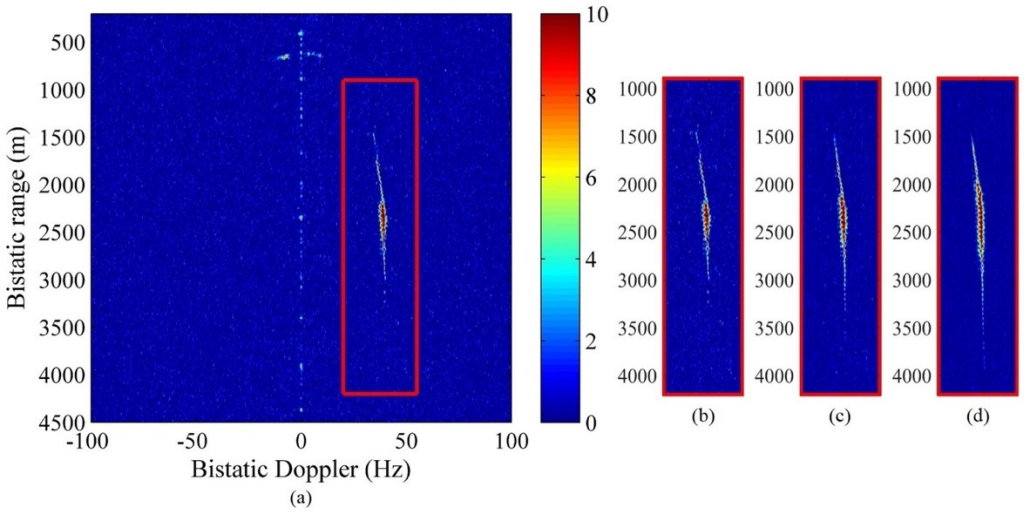

Figure 4.25 - RD tracks concerning the target 'St Faith' over 286 s dwell time – a) $N = 1$, b) $N = 5$, c) $N = 10$, d) $N = 20$.

To quantify the performance improvement achievable by increasing the integration window, Table 4.V lists the maximum radar range at which the target is detected for the considered cases (having set $P_{fa}=10^{-3}$). Particularly, these values are

defined as the starting point from which the target track is observable with continuity. In the same table are also reported:

- the experimental integration gain measured from maximum radar range improvement as the squared value of the ratio of maximum range when N>1 to maximum range when N=1;
- the experimental RCS variation measured between slow time instant when target is at the maximum range concerning case N=1 and slow time instant when target is at the maximum range concerning N>1: in evaluating this quantity a normalization has been applied taking into account the different attenuations related to the different range values. As apparent from results in the table (and also from images in Figure 4.26), target RCS shows a considerable variation with increasing values as slow time increases.
- the experimental overall integration gain obtained as the combination of the two above components;
- the theoretical integration gain value as from eq. (3.7) and, as a more relaxed reference, a possible interval of values between $[\sqrt{N},\ N]$.

From shown results, it is possible to observe that the experimental overall integration gain is well in line with theoretical predictions: particularly part of the integration gain available when increasing N is used to compensate the loss in RCS observed in this particular acquisition and part is exploited for the maximum radar range improvement. A higher maximum range improvement could be achieved for those cases involving a more stable RCS value. Noticeably, target 'St Faith' is detected up to 4 km. Further performance improvement could be obtained by exploiting multiple transmitters, which is the subject of the next chapter.

TABLE 4.V - MAXIMUM RADAR RANGE

	$N = 1$	$N = 5$	$N = 10$	$N = 20$
Maximum Range $R_{max}(N)$, [m]	2656 ($u_{N=1}$=155 sec)	2986 ($u_{N=5}$=122 sec)	3310 ($u_{N=10}$=89 sec)	3915 ($u_{N=20}$=30 sec)
Experimental Maximum Range Gain $[R_{max}(N)/R_{max}(N=1)]^2$ „ [dB]	-	1.1	1.9	3.4
Experimental RCS variation $\sigma(u_{N=1})/\sigma(u_N)$, [dB]	-	5.7	7.9	7.3
Experimental Integration Gain $I_{exp}(N) = [R_{max}(N_f)/R_{max}(N=1)]^2 \cdot \sigma(u_{N=1})/\sigma(u_N)$, [dB]	-	6.7	9.8	10.7
Theoretical Integration Gain I(N), eq. (4), [dB]	-	5.6	7.7	9.7
Theoretical Integration Gain Interval $[\sqrt{N}, N]$, [dB]		[3.5, 7]	[5, 10]	[6.5, 13]

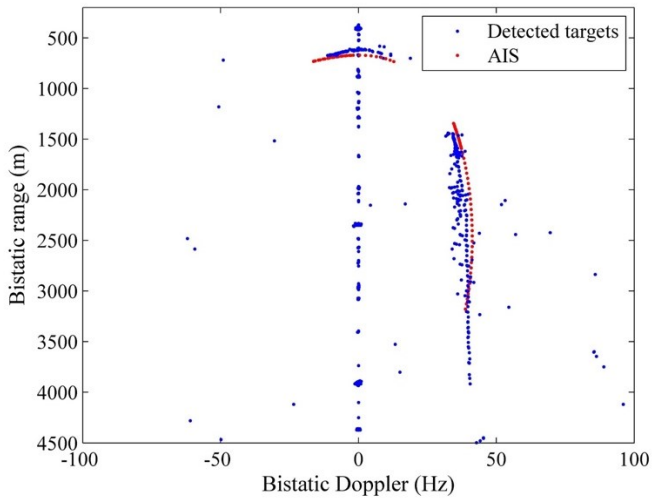

Figure 4.26 - Final detection map by applying CA-CFAR detector ($N = 20$).

Chapter 5

Multi-channel M-MTD technique

In this chapter is presented an approach for the exploitation of the multistatic configuration in order to increase the signal-to-noise ratio (SNR) level and, at the same time, to measure the target DOA, thus providing a joint target detection and localization even of targets not detectable when the detection threshold is set at the bistatic level. Particularly, is considered a centralized detection method implementing a single-stage to detect and localize the target. This may potentially outperform the conventional two-stage process where independent decisions are taken at each bistatic link and subsequently the localization is performed by multilateration, thanks to the achievement of the spatial diversity gain [69]. To achieve such a purpose, the signals collected by a single receiver over long dwell times and over multiple baselines are integrated in both the temporal and space domains to form a long-time and multistatic RD map. Such a map is obtained through a non-coherent combination of the RD maps achieved over short and consecutive Coherent Processing Intervals (CPIs) over all the available baselines. If the target energy is properly integrated over the individual RD maps, the total target power can be effectively increased, while at the same time the disturbance background fluctuations reduced thus improving the final SNR.

To properly combine the contributions over the long dwells and the multiple baselines, ad hoc range&Doppler migration compensation techniques as well as

time&space integration strategies need to be applied. Concerning migration compensation, two sources have to be taken into account. The former is a migration over the temporal domain, i.e. the range and Doppler migration that the target experiences in each baseline due to its motion. The latter is a migration over the space domain, due to the different RD positions observed in the multiple bistatic geometries. To cope with these problems, a (time&space) migration compensation technique is proposed that realizes an energy alignment among the RD maps pertaining the successive CPIs at each individual baseline and remaps the different bistatic range and Doppler planes into a common monostatic equivalent plane. Regarding the integration over the time and space domains, firstly an optimum technique is derived and then a suboptimum approach is also considered. For both approaches the theoretical performance, in terms of false alarm and detection probability, are derived, investigated and compared analyzing the increase available from the exploitation of the time and/or space domains and showing that the suboptimum scheme yields limited losses in many cases of practical interest. In addition, since the mapping of the target bistatic range and Doppler history in the equivalent monostatic plane depends on the target DOA, a bank structure is adopted being each branch of the bank matched to a specific DOA value. The information provided by the bank is thus exploited to estimate the target DOA and range and DOA information are then used to localize the detected target. Criteria to design the bank are provided and localization capabilities are investigated and proved by means of synthetic datasets. Finally, results from experimental campaigns (using up to four Galileo transmitters) are reported and discussed clearly demonstrating the effectiveness of the proposed approach.

5.1 Joint target detection and localization with multistatic radar

This section introduces the proposed processing chain that aims at performing an integration over the full aperture T_a and over all the M baselines. The block diagram of the proposed technique is depicted in Figure 5.1. The final goal is

to obtain an integrated RD map, where the target can be detected and jointly localized in the Cartesian plane. The main idea is to obtain a RD map for each frame and for each baseline and then to perform the integration. To achieve these purposes, the range&slow-time data undergo a processing comprising three main stages: target motion compensation, multistatic compensation, and space-time integration, as described in the following.

The range&slow-time (r, u) data pertaining the nth frame and the mth satellite can be obtained from the eq. (4.3) by converting the fast time dimension into bistatic range as $r = c \cdot \tau$:

$$s_{m,n}(r,u) = A_{m,n} \cdot \exp\left\{-j\frac{2\pi}{\lambda}R_m(u)\right\} \cdot \Lambda[r - R_m(u)] \cdot rect\left[\frac{u - nT_f}{T_f}\right] \tag{5.1}$$

where $A_m(u)$ represents the complex amplitude backscattered by the target when illuminated by the mth satellite.

The bistatic range (3.2) can be expanded in Taylor series around the reference time instant pertaining the reference frame. Assuming not maneuvering ships, a second order expansion generally suffices, leading to

$$R_m(u) \approx R_m^0 + \dot{R}_m u + \ddot{R}_m \frac{u^2}{2} \tag{5.2}$$

It is also worth to point out that from (5.2), the target bistatic Doppler history is obtained as

$$f_{u_m} = -\frac{1}{\lambda}\left[\dot{R}_m + \ddot{R}_m u\right] = f_{dc_m} + f_{dr}\, u \tag{5.3}$$

where f_{dc_m} denotes the bistatic Doppler position pertaining the mth baseline at the reference instant, and f_{dr} denotes the target Doppler rate; in the latter, the dependence on index m has been neglected taking into account the large distance between the transmitters and both the receiver and target (namely, $\ddot{R}_m \approx \ddot{R}\ \forall m$), [38].

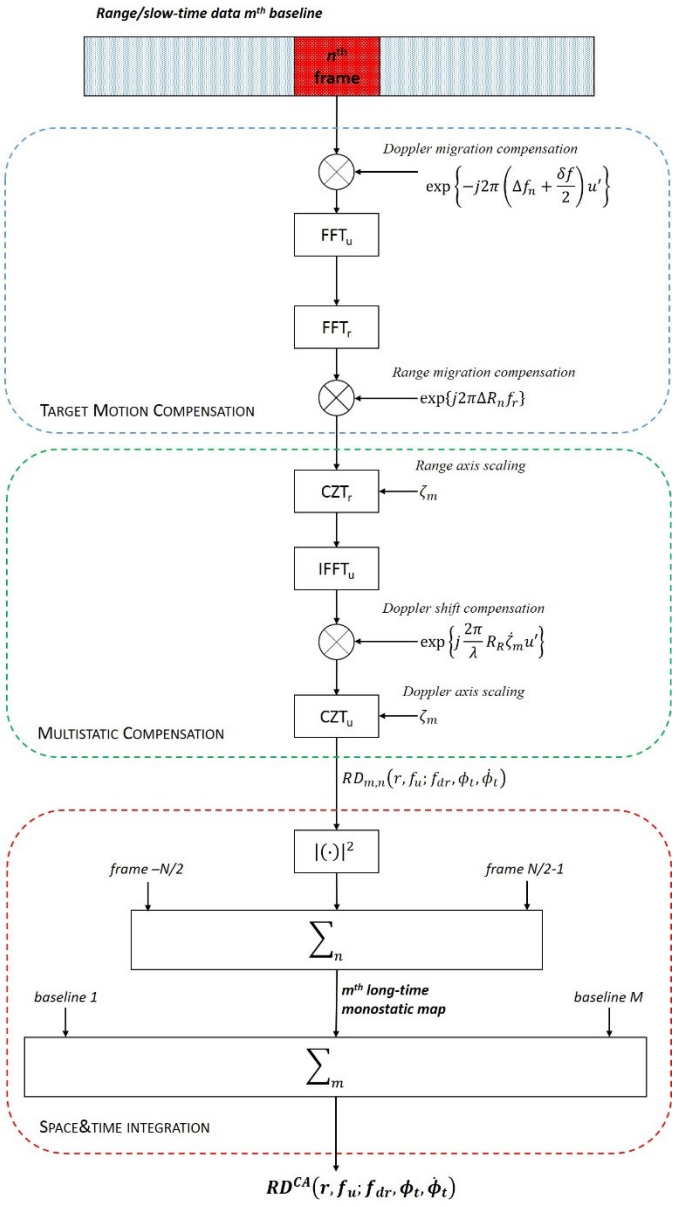

Figure 5.1 - Processing chain

5.1.1 Target motion compensation

The first stage of the proposed technique has been investigated in section 4.1.1 considering a single baseline, thus the proposed technique can be regarded in first instance as a proper generalization of the long time maritime MTD technique. However, as aforementioned, both the long-time and multiple baselines

integrations will allow to improve the SNR and the spatial diversity will enable the target localization.

The TMC described in 4.1.1 is separately applied to the stream data pertaining the mth baseline. It is interesting to note that the TMC is identically obtained for all the M bistatic links. Indeed, Doppler migration depends only on the Doppler rate, while the range migration depends on both target Doppler and Doppler rate. Since the Doppler-dependent term of the range migration can be adaptively compensated by varying the Doppler centroid in the (f_r, f_u) domain, the whole procedure depends only on the target Doppler rate that is the same for all the baselines, (5.6).

In the bistatic case (M=1), a quadratic integrator follows the TMC thus obtaining a long-time RD map. In this map the moving ship has better chances to compete with the disturbance contributions and therefore it may be detected by applying a proper threshold detector. In the multistatic case, the technique in 4.1.1 is hence potentially able to provide for a target M measures of its bistatic ranges. Therefore, the target can be subsequently localized by means of multilateration techniques [32]. Nevertheless, such an approach strictly requires the detection of the target at the individual bistatic level and therefore low RCS and/or far targets will give rise to missed detections. The characteristics of multiple low-power transmitters of the system under consideration makes of significant importance to exploit the available target power in input to the receiver to improve the SNR and enable the detections of low observable targets. This can be obtained by considering the integration of the RD maps not only at the frame level, but at the multi-baseline level as well. However, as well as different frames experience a different range&Doppler location of the target energy because of its motion, different baselines experience a different position due to the different transmitters' position. The alignment of the target energy over the multiple bistatic links is referred to as Multistatic Compensation (MSC) and it is described in the following section. As

depicted in Figure 5.1, this stage is fed with the motion compensated maps in the fast frequency/Doppler domain.

5.1.2 Multi-transmitter technique

The goal of the MSC is to map the target energy in a domain that does not depend on the specific bistatic geometry, namely on the index m. Such a domain is the target-to-receive range&Doppler plane, namely the domain pertaining the target-to-receive distance R_R (hereinafter referred to as monostatic range) and the related Doppler frequency $f_{u_R} = -\frac{1}{\lambda}\dot{R}_R$ (hereinafter, monostatic Doppler).

With this objective in mind, the bistatic range (3.1) is rewritten as $R_m(u) = R_R(u) + \Delta R_m(u)$, where the term $\Delta R_m(u) = R_{T_m}(u) - R_{B_m}(u)$ represents the transmitter contribution to the bistatic range history of the target. Then, $\Delta R_m(u)$ is expanded in Taylor series around the receiver position, arresting the series at the first order, carrying to (the dependence on the slow-time has been hereinafter omitted for sake of simplicity)

$$\Delta R_m \approx -\frac{x \cdot x_m + y \cdot y_m}{\sqrt{x_m^2 + y_m^2 + z_m^2}} = -R_R \cdot [\cos(\theta_m)\cos(\phi_m - \phi_t)] \tag{5.4}$$

Therefore, R_m can be approximated as

$$R_m \approx R_R \cdot [1 - \cos(\theta_m)\cos(\phi_m - \phi_t)] = R_R \cdot \zeta_m(\phi_t) \tag{5.5}$$

where $\zeta_m(\phi_t)$ is a target DOA-dependent scale factor. Hence, the bistatic Doppler is easily obtained as

$$f_{u_m} \approx f_{u_R} \cdot \zeta_m(\phi_t) - \frac{R_R}{\lambda} \cdot \dot{\zeta}_m(\phi_t, \dot{\phi}_t) \tag{5.6}$$

where $\dot{\phi}_t$ is the rate of the target DOA and

$$\begin{aligned} \dot{\zeta}_m(\phi_t, \dot{\phi}_t) = {} & [\sin(\theta_m)\cos(\phi_m - \phi_t)] \cdot (\dot{\theta}_m + \dot{\phi}_m) \\ & - [\cos(\theta_m)\sin(\phi_m - \phi_t)] \cdot \dot{\phi}_m \end{aligned} \tag{5.7}$$

Based on (5.5) and (5.6), the MSC converts the bistatic range in the monostatic range and the bistatic Doppler in the monostatic Doppler. To achieve this purpose, three steps are implemented as follows.

a. Range axis scaling – Eq. (5.5) shows that the bistatic range is scaled version of the monostatic range with a scale factor depending on the target DOA. Thus, the bistatic range can be converted into the monostatic one by means of a stretching (or shrinkage) of the bistatic range axis. This can be efficiently implemented by making use of the Chirp Zeta Transform (CZT) [70]. We recall that for a L-samples sequence, the CZT on the unit circle in the z-plane at points with constants angular spacing $2\pi\alpha/L$ allows to stretch ($\alpha > 1$) or shrink ($\alpha < 1$) the output axis spacing (while for $\alpha = 1$ the CZT coincides with the Discrete Fourier Transform of the sequence). Therefore, the fast frequency axis can be converted in the monostatic range by setting the angular spacing $2\pi\frac{\zeta_m(\phi_t)}{L_r}$, being L_r the number of samples in the fast frequency domain.

b. Doppler shift compensation – From (5.6)) it can be observed that the bistatic Doppler is approximately a DOA-dependent scaled version of the monostatic Doppler plus a shift depending on the target distance from the receiver, its DOA and its DOA rate. The Doppler shift can be compensated by operating a slow-time IFFT to transit in the monostatic range and slow-time domain and multiplying in this domain the data pertaining each range cell for a phase term according to $-\frac{R_R}{\lambda}\cdot\dot{\zeta}_m(\phi_t,\dot{\phi}_t)$.

Doppler axis scaling – After the Doppler shift compensation, the bistatic Doppler axis can be scaled by resorting again to the CZT. Let L_u be the number of slow-time samples in a single CPI (i.e., T_f/T_c), the slow-time data can be converted to monostatic Doppler by applying a slow-time CZT computed again on the unit circle in the z-plane with angular spacing between the points equal to $2\pi\frac{\zeta_m(\phi_t)}{L_u}$.

It has to be noted that while the frame alignment depends on the Doppler rate f_{dr}, the MSC depends on the target DOA ϕ_t and its rate $\dot{\phi}_t$. Likewise the TMC, a completely adaptive MSC procedure needs to resort to a filter bank structure with different values of these parameters.

5.1.3 Filter bank design criteria

The criteria for the sampling of the Doppler rate axis is the same shown in the previous Chapter (4.1.2). The sampling of the DOA and $\dot{\phi}_t$ axes need to be defined. The minimum and maximum DOA are defined according to the surveillance antenna beam, while the sampling of the DOA axis has to be chosen in order to ensure a positioning error in range and Doppler less than the range and Doppler resolution cell, respectively. The requirement in range results in the following constraint:

$$\delta\phi_t \leq \frac{c}{BR_R}\frac{(1 - cos\theta_m \cos(\phi_m - \phi_t))}{\cos\theta_m \, sin(\phi_m - \phi_t)} \tag{5.8}$$

while the condition in Doppler gives the following sampling step:

$$\delta\phi_t \leq \frac{(1 - \cos\theta_m \cos(\phi_m - \phi_t))}{T_f f_u \cos\theta_m \, sin(\phi_m - \phi_t)} \tag{5.9}$$

The more stringent condition provides an appropriate sampling step.

The bounds on the interval $\left[-\dot{\phi}_{t_{max}}, \dot{\phi}_{t_{max}}\right]$ can be set according the maximum variation of the target DOA, which can be set according to the maximum tangential velocity and the minimum target-to-receiver distance. The sampling step of $\dot{\phi}_t$ has to assure a residual Doppler error lower than the resolution cell ($1/T_f$). Starting from this assumption, the constraint is given by:

$$\delta\dot{\phi}_t \leq \frac{\lambda}{T_f \cos\theta_m \, sin(\phi_m - \phi_t) \, R_R} \tag{5.10}$$

For the nth frame and mth link, the RD map following the TMC and MSC procedures for a specific tried $\left(f_{dr}, \phi_t, \dot{\phi}_t\right)$ is denoted as $RD_{m,n}\left(r, f_u; f_{dr}, \phi_t, \dot{\phi}_t\right)$. As

it will be explained in the next section, the combination of the MN maps allows achieving a space&time integration gain as a function of these parameters, enabling the estimation of detected target location.

5.1.4 Space&time integration

After the TMC and the MSC, the $RD_{m,n}$ maps resulting from a given branch of the bank have to be integrated into an individual map where the detection procedure can take place. Thus, the question arises as how to combine the maps pertaining to the different frames and baselines. To answer the question, we can derive a combination criteria based on a Likelihood Ratio Test (LRT) by formulating a usual detection problem as the choice between null hypothesis $\mathcal{H}_0$ (target does not exist at the selected range and Doppler cell) and alternative hypothesis $\mathcal{H}_1$ (target does exist at the selected range and Doppler cell). Let $r_{m,n}$ be the hypothesized range and Doppler cell pertaining the nth frame and the mth bistatic channel after that the data have been time- and space- aligned (namely, we are focusing on the $RD_{m,n}$ maps pertaining the actual $f_{dr}, \phi_t, \dot{\phi}_t$). The binary hypothesis test can be written as

$$\begin{aligned} &\mathcal{H}_0: \ r_{m,n} = w_{m,n} \\ &\mathcal{H}_1: \ r_{m,n} = A_{m,n} + w_{m,n} \end{aligned} \tag{5.11}$$

$w_{m,n}$ is the disturbance background. In this work, it is modelled as white Gaussian characterized by power σ_w^2, namely $w_{m,n} \sim \mathcal{CN}(0, \sigma_w^2)$ where $\mathcal{CN}$ denotes the complex normal distribution. This assumption can be justified taking into account the very low power budget provided by GNSS satellites, making the system mainly noise-limited rather than clutter limited [38]. It could be also shown that this hypothesis is in agreement with the experimental data presented in section 5.3.

$A_{m,n}$ represents the complex amplitude of the signal (for the sake of simplicity and without loss of generality, the deterministic improvement factor pertaining the coherent integration gain has been here included in $A_{m,n}$). At the individual baseline level, its variation among the different frames is assumed to follow a Swerling I model. Let σ_m^2 be target mean power observed at the mth bistatic link, $A_{m,n}$ can be

modeled as a zero-mean complex normal random variable with variance σ_m^2, i.e., $A_{m,n} \sim \mathcal{CN}(0, \sigma_m^2)$. As a consequence of the different perspectives provided by different satellites, σ_m^2 generally varies among the different baselines (i.e., it varies with m).

From the above model, the likelihood ratio test (LRT) detector $\mathcal{L}$ can be derived as shown in Appendix A, leading to

$$\mathcal{L} = \sum_m \left\{ \eta_m \sum_n \left| r_{m,n} \right|^2 \right\} \underset{\mathcal{H}_0}{\overset{\mathcal{H}_1}{\gtrless}} t_h^{LRT} \tag{5.12}$$

where t_h^{LRT} is the threshold set by the desired probability of false alarm,

$$\eta_m = \frac{SNR_m}{SNR_m + 1} \tag{5.13}$$

and SNR_m is the ratio σ_m^2 / σ_w^2. Eq. (5.12) shows that $\mathcal{L}$ is the cascade of a quadratic integrator over the frame domain ($\sum_n \left| r_{m,n} \right|^2$) followed by a weighted sum over the multiple baselines according to a coefficient η_m depending on the local SNR. As it could be expected, greater weight has to be applied to the best baseline in terms of SNR, so, ultimately, to the bistatic geometry observing the higher bistatic target RCS.

It can be observed that although a quadratic integrator is applied at both the temporal and spatial domain, there is a relevant difference between the two cases: while the returned powers from a target in the multi-frame maps pertaining an individual baseline are expected to fluctuate around the same average value, by observing a complex target such as a ship by widely separated perspectives, strong variations of the backscattered energy toward the receiver could be easily experienced. Therefore, the maps pertaining different baselines should be combined taken into accounts the different levels of reliability according to the local SNR [71]. Obviously, it is unrealistic assuming a priori knowledge of the SNR and the detector (5.12) is assumed as a benchmark of the achievable performance.

A practical (but suboptimum) detector can be obtained by realizing a full quadratic integration in both time and space domains, corresponding to the decision rule (5.12) by setting $\eta_m = 1$ for all the baselines with a proper threshold. The final map resulting from the quadratic integrator (QI) for each tested triad $(f_{dr}, \phi_t, \dot{\phi}_t)$ is given by

$$RD^{QI}(r, f_u; f_{dr}, \phi_t, \dot{\phi}_t) = \frac{1}{MN} \sum_m \sum_n \left| RD_{m,n}(r, f_u; f_{dr}, \phi_t, \dot{\phi}_t) \right|^2 \qquad (5.14)$$

Thanks to the energy alignment over the temporal frames and over the multiple bistatic links, the target energy builds up in the RD^{QI} map corresponding to the actual target kinematics. The time integration gain (related to the TMC) along with the space integration gain (related to the MSC), provides a SNR enhancement such that the moving target can likely compete with the disturbance contributions and therefore be detected. It has to be noted that the QI detector is a suboptimum version of the LRT. Particularly, it still realizes the optimum combination in time domain levels, while the absence of a weighting process among the different baselines is expected to provide worse results than the LRT, especially for those cases where a strong variation of the RCS over the different perspectives is experienced. The detection performance of the QI will be compared to the optimum represented by the LRT in section 5.2.

Along with the detection of the target, the proposed technique aims at its simultaneous localization. The joint detection and localization of the target relies on the consideration that the time&space integration gain is a function of the tested $(f_{dr}, \phi_t, \dot{\phi}_t)$. Therefore, the selection of the branch of the bank providing the maximum integration gain provides a direct estimate of the target kinematics. In practice, for each target detected at the generic Doppler rate f_{dr}^*: (1) the corresponding area of interest T is identified in the range&Doppler plane; (2) the estimated values of the target DOA and DOA derivative are obtained as follows

$$\left(\hat{\phi},\hat{\dot{\phi}}\right)=\max_{\phi_t,\dot{\phi}_t} G\left(\phi_t,\dot{\phi}_t\right)=\max_{\phi_t,\dot{\phi}_t}\{\max RD^{QI}\left(r,f_u;f_{dr}^{*},\phi_t,\dot{\phi}_t\right)\quad (r,f_u) \in T,\left(\phi_t,\dot{\phi}_t\right)\in S\} \tag{5.15}$$

being S the subset of the branches where detections arise. The estimated DOA is then combined with the range at which the target is detected (representing the target-to-receiver distance R_R) to retrieve its Cartesian coordinates (3.1).

It has to be noticed that in the case of close multiple targets, the risk of merging information coming from different targets is high, carrying to the ambiguities usually referred to as ghost targets. The ghost problem is inherent to each multistatic radar system and proper strategies for its handling should be also considered. This could be a challenging task that requires specific efforts and therefore it is not treated here. Nevertheless, it is worth to mention that the large number of satellites is expected to be a key element to provide ghost rejection capability, since the target-to-target interaction giving rise to a ghost solution with a particular couple of satellites will give rise to a different ghost solution by considering different satellites; thus, with a sufficiently large formation of transmitters the ambiguities are expected to vanish.

5.2 Performance analysis

5.2.1 Detection performance

In order to investigate the potential improvement in detection performance by exploiting the integration over the time and space domains, we refer to the $RD_{m,n}$ maps assuming ideal TMC and MSC. For sake of convenience and without loss of generality, we consider the QI operator realizing a sum (in place of a mean) of the range and Doppler cell under test (CUT) over the N frames and M bistatic links. We explicitly point out that with such an assumption, the QI operator coincides with the $\mathcal{L}$ detector in (5.12) by setting $\eta_m = 1\ \forall m$.

First, the probability of false alarm (P_{fa}) for the LRT and QI operators to be used to compute the detection thresholds are presented. Then, close-form expressions for the probability of detection (P_d) for both the detectors are provided. Full analytical details are provided in Appendix B.

Let t_h^{LRT} and t_h^{QI} be the set thresholds for the LRT and QI detectors, respectively, the corresponding P_{fa} are given by

$$P_{fa}^{LRT} = 1 - C_A \cdot \sum_{k=0}^{\infty} \delta_{A_k} \frac{\gamma\left(MN + k, {t_h^{LRT}}/{\sigma_w^2} \over \eta_{min}\right)}{\Gamma(MN + k)} \tag{5.16}$$

$$P_{fa}^{QI} = 1 - \frac{\gamma\left(MN, {t_h^{QI}}/{\sigma_w^2}\right)}{\Gamma(MN)} \tag{5.17}$$

For a desired false alarm rate, numerical inversion of (5.16) and (5.17) provides t_h^{LRT} and t_h^{QI}. It should be noted that for practical purposes, (5.16) can be replaced with a truncated version considering the first K' elements of the infinite series according to a desired accuracy. The corresponding P_d for the two detectors are equal to

$$P_d^{LRT} = 1 - C_B \cdot \sum_{k=0}^{\infty} \delta_{B_k} \frac{\gamma\left(MN + k, {t_h^{LRT}}/{\sigma_w^2} \over SNR_{min}\right)}{\Gamma(MN + k)} \tag{5.18}$$

$$P_d^{QI} = 1 - C_C \cdot \sum_{k=0}^{\infty} \delta_{C_k} \frac{\gamma\left(MN + k, {t_h^{QI}}/{\sigma_w^2} \over SNR_{min} + 1\right)}{\Gamma(MN + k)} \tag{5.19}$$

In eqs.(5.16)- (5.19) , $\Gamma(\cdot)$ is the Gamma function and $\gamma(a, b) = \int_0^b t^{a-1}e^{-t}dt$ is the lower incomplete Gamma function; SNR_{min} is the lowest average SNR level

observed in the M bistatic channel and η_{min} is the corresponding weight (5.13); parameters C_j and δ_{j_k} $(j = A, B, C)$ are reported in Appendix B,. It is worth to notice that in the special case of equal average SNR observed at the M baselines, $C_j = 1$, $\delta_{j_0} = 1$ and $\delta_{j_{k>0}} = 0$, therefore (5.16), (5.18) and (5.19) reduces at common expressions of P_{fa} and P_d for gamma variates.

In a first case study, we assume that the target power fluctuates frame-to-frame according to a Swerling I model with the same average value among the different links (i.e., $\sigma_m^2 = \sigma^2 \; \forall m$). We explicitly point out that in this particular case both LRT and QI detectors realize an unweighted sum of the data, thus their performance coincide. Figure 5.2 shows the probability of detection as a function of the SNR pertaining the individual baseline (average SNR observed in a single frame). Threshold has been set to achieve a false alarm ratio of 0.001. Full lines represent the theoretical P_d, while red markers show the corresponding result achieved by Monte Carlo simulations (10000 independent trials for each tested SNR). From the figure, we can observe as the detection performance progressively enhances by increasing the number of integrated maps, wheatear they are multi-frame maps pertaining a single satellite, single frame maps pertaining multiple satellites, or multi-frame and multi-satellite maps. For example, only high-RCS targets at relatively short ranges able to provide SNR greater than 15 dB could be detected with $P_d > 0.9$ in the map achieved over a short time (namely, single frame) exploiting an individual satellite. The non-coherent integration of N = 10 motion compensated maps allows to achieve the same detection performance for considerably lower RCS (and/or at higher ranges) targets, with a required single map average SNR equal to 4.2 dB. By further considering the integration of multiple baselines we can reduce the required SNR at -1 dB and -2.5 dB considering M = 5 and M = 10 satellites, respectively. Therefore, a large integration gain is made available by properly exploiting the multiple satellites simultaneously illuminating the scene, which enables the detection of targets not observable with the individual

bistatic geometry, even exploiting a long integration time. Moreover, the improvement of the performance enabled by multiple satellites can be also used to reduce the number of integrated frames. It should be pointed out that the temporal integration gain provided by the TMC could be affected by not negligible target maneuvers, resulting in higher order terms of the Doppler migration. By trading part of the integrated frames with a greater number of satellites, the robustness of the TMC can be improved making it less sensitive to possible signal model mismatches due to more complex target motions.

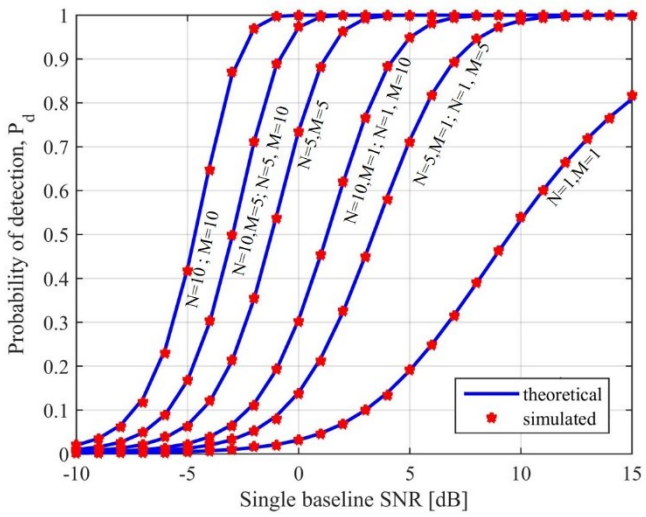

Figure 5.2 - Multi-frame and multi-baseline probability of detection.

As already underlined, the different illumination angles due to the multiple transmitters can result in large variations of the target RCS. The detection performance of the QI operator is here tested and compared to the ideal performance achieved by the LRT for a few scenarios considering different variation of the average RCS observed by the multiple bistatic geometries. N = 5 frames and M = 5 satellites are considered. The average RCS observed by the mth baseline during the integration time is set according to the rule $\sigma_m = a_m \bar{\sigma}$, where a_m are weighting coefficients such that $\sum_m a_m = M$. Therefore, the average target power

observed in each frame by the multistatic system is $M\bar{\sigma}$. Figure 5.3 shows the theoretical and simulated probability of detection (for P_{fa} set to 0.001) for the LRT and QI detectors as a function of the single baseline reference SNR (i.e., $\bar{\sigma}/\sigma_w$) for different spread of the target RCS over the baselines. The weight coefficients defining the entity of the RCS variations are shown in the boxes in the bottom of the figures. Figure 5.3 (a) shows the case of a smooth spreading (a coefficients are 0.33, 0.67, 1, 1.33, 1.67) and as it is apparent LRT and QI detectors obtain very similar performance. In Figure 5.3 (b) a larger spreading has been considered (a coefficients are 0.1, 0.1, 0.1, 4.96, 0.1). In particular, this scenario would represent the situation in which the energy backscattered from the target is much stronger for some particular bistatic angle than other perspectives. Obviously, in such a case the main diversity gain consists in the higher chances to intercept the favorable bistatic angles. In terms of detector performance, we can observe that LRT provides some improvement moving from the smooth to the strong RCS angular spread while the QI experiences some losses. However, these variations are rather limited, and the QI loss with respect the optimum performance are not greater than about 2 dB, thus proving the robustness of the QI operator against the RCS angular spread.

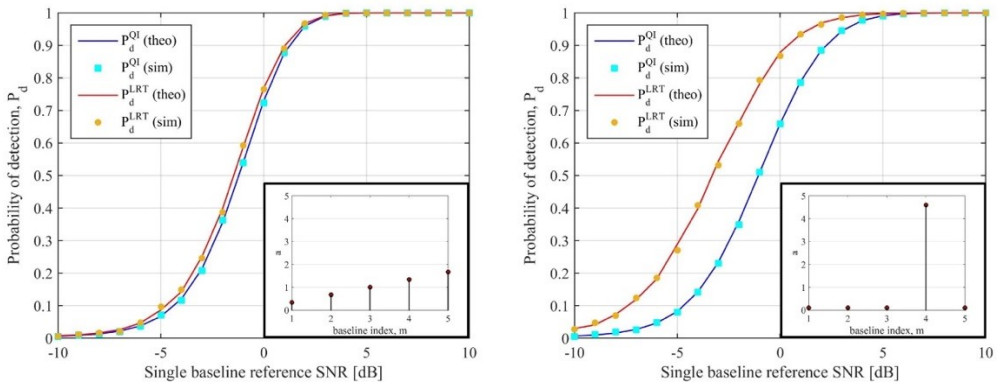

Figure 5.3 - LRT and QI detection performance for target RCS experiencing a smooth (a) and a strong (b) angular spread.

5.2.2 Localization capabilities

The possibility to localize the detected target in the local reference system is here tested against synthetic data. Four satellites of Galileo constellation are considered as transmitters of opportunity, exploiting signals transmitted in the E5a band. The satellites trajectories were obtained from a GNSS satellite tracking website [67] and the main parameters are listed inFigure 5.4. At the reference time instant, the target is moving in the surveyed area at the distance of 1500 m from the receiver with a direction of arrival $\phi_t = 10°$. The target velocity is 7 kn with heading 45°, corresponding to a DOA rate $\dot{\phi}_t$ =0.079°/s. The entire dwell time is set to be 30 seconds, segmented in N = 10 frames of duration T_f = 3 s.

To show clearly the localization capability of the proposed technique, the analysis is provided in noise-free conditions accounting for a target with constant RCS . Figure 5.4 shows the function G in (5.15) obtained by considering two transmitters (sat. 1 and sat. 2 in Table 5.I) for three different values of the Doppler rate; in particular, Figure 5.4 (a) is the slice obtained for the actual value of the Doppler rate $f_{dr} = -0.011$ Hz/s, while Figure 5.4 (b) and Figure 5.4 (c) pertain wrong f_{dr} values (-0.100 Hz/s and -0.333 Hz/s, respectively). In the figures, 0 dB denotes the target power evaluated at the individual RD map level. Therefore, a maximum gain of 13 dB can be obtained when all the frames and baselines contributions are correctly aligned. It can be observed that such a value is reached in the slice pertaining the actual Doppler rate in correspondence of the actual angular values $(\phi_t, \dot{\phi}_t)$. Therefore, a direct estimate of the target cross-range velocity component and its direction of arrival is provided; combining the latter information with the retrieved monostatic range the target localization is achieved. Comparing the three figures, it is interesting to note the different levels of background in the slices pertaining the different Doppler rates. Indeed, it represents the integration gain resulting from the multi-frame combination only: therefore, the highest value is obtained for the actual Doppler rate, providing best TMC

performance. When the TMC is performed with wrong Doppler rate values, both Doppler migration inside the frame and range and Doppler migration among the frames are not correctly compensated. Due to the target energy spread over multiple cells, the multistatic compensation procedure cannot relocate the target contributions around a single position and therefore a spread of the integration gain over multiple $(\phi_t, \dot{\phi}_t)$ couples is observed. To better highlight the effect of the Doppler rate on the achieved integration gain, Figure 5.5 shows the integration gain variation as a function of the Doppler rate offset Δf_{dr} between the tested and the actual Doppler rate by fixing the actual values of ϕ_t and $\dot{\phi}_t$. As it is apparent, the maximum is obtained for $\Delta f_{dr} = 0$ Hz/s.

Likewise, the multilateration approach, it is expected that the capability of the proposed technique to localize the target depends on the degree of spatial diversity offered by the selected transmitters. If a single couple of transmitters is selected, it makes sense that higher the difference in bistatic iso-range contours provided, higher the accuracy of the estimated DOA. Figure 5.6 shows three different actual Doppler rate slices of G functions achieved under three different conditions. Figure 5.6 (a) and (b) show G when the couple (sat. 1, sat. 2) and (sat. 3, sat. 4) have been selected, respectively. It could be shown that sat. 3 and sat. 4 have a larger difference in bistatic iso-ranges than sat. 1 and sat. 2. Consequently, the MSC is able to better concentrate the target energy in a smaller region in the $(\phi_t, \dot{\phi}_t)$ plane, as it can be observed comparing the two images, implying a greater accuracy in the DOA estimation. Figure 5.6 (c) shows G when all the satellites have been selected, where the higher integration gain due to the greater number of consider baselines is easily observed. Therefore, increasing the number of considered satellites can not only achieve a greater SNR, but also improving the quality of the detected target localization thanks to the higher energy concentration in the $(\phi_t, \dot{\phi}_t)$ plane.

TABLE 5.I - SIMULATED SCENARIO – SATELLITES PARAMETERS

	Parameter	Unit	Value
Satellite 1	Number	-	GSAT0204
	Azimuth angle (at reference instant) ϕ_1	deg	-110.70
	Azimuth angle rate $\dot{\phi}_1$	deg/s	0.0057
	Elevation angle (at reference instant) θ_1	deg	53.57
	Elevation angle rate $\dot{\theta}_1$	deg/s	0.0056
Satellite 2	Number	-	GSAT0206
	Azimuth angle (at reference instant) ϕ_2	deg	-81.81
	Azimuth angle rate $\dot{\phi}_2$	deg/s	-0.0106
	Elevation angle (at reference instant) θ_2	deg	53.74
	Elevation angle rate $\dot{\theta}_2$	deg/s	0.0006
Satellite 3	Number	-	GSAT0210
	Azimuth angle (at reference instant) ϕ_3	deg	-25.72
	Azimuth angle rate $\dot{\phi}_3$	deg/s	-0.0053
	Elevation angle (at reference instant) θ_3	deg	9.16
	Elevation angle rate $\dot{\theta}_3$	deg/s	-0.0002
Satellite 4	Number	-	GSAT0214
	Azimuth angle (at reference instant) ϕ_4	deg	54.01
	Azimuth angle rate $\dot{\phi}_4$	deg/s	-0.0036
	Elevation angle (at reference instant) θ_4	deg	35.92
	Elevation angle rate $\dot{\theta}_4$	deg/s	-0.0045

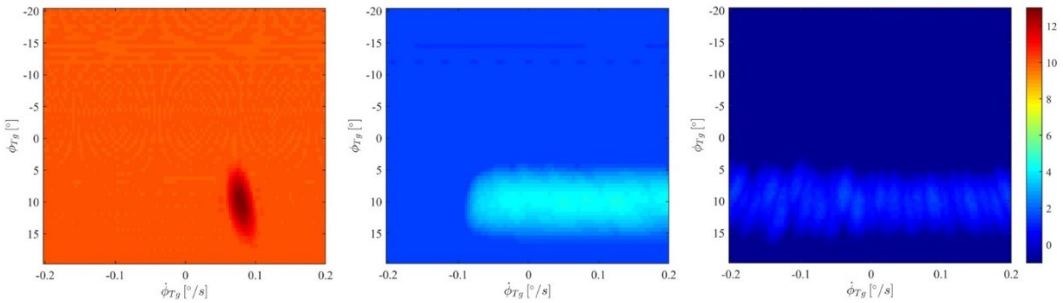

(a) (b) (c)

Figure 5.4 - Integration gain (dB scale) for (a) $f_{dr} = -0.011$ Hz/s (actual value), (b) $f_{dr} = -0.100$ Hz/s and (c) $f_{dr} = -0.333$ Hz/s.

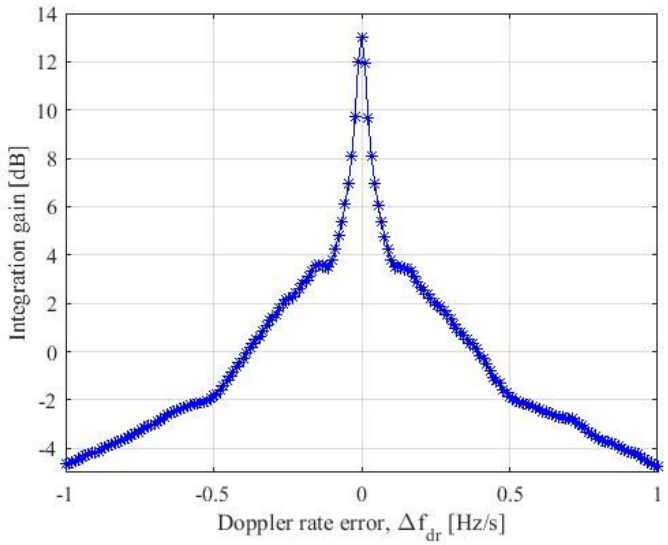

Figure 5.5 - Integration gain as a function of the Doppler rate error for the actual DOA and DOA rate.

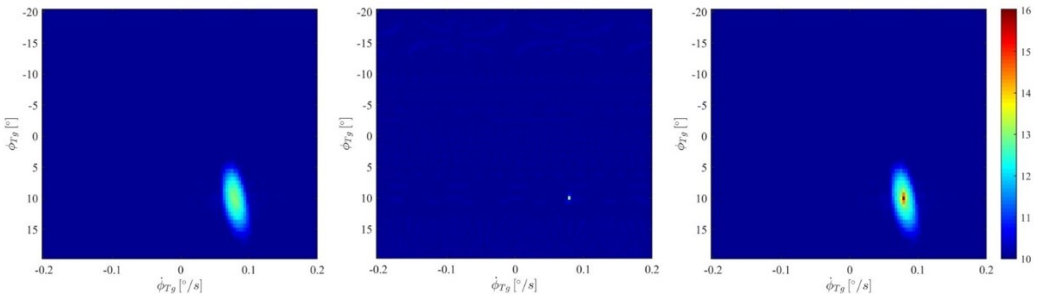

(a) (b) (c)

Figure 5.6 - Integration gain (dB scale) considering (a) M = 2 (sat.1 and sat. 2, low spatial diversity), (b) M=2 (sat. 3 and sat. 4, large spatial diversity), (c) M = 4.

5.3 Experimental results

An experimental campaign was conducted inside the H2020 SpyGLASS project, [34]. Proof-of-concepts experiments were conducted in two different scenarios: river shipping and port operations. Galileo satellites have been exploited and more in detail the pilot signals transmitted on the frequency band E5a (carrier frequency: 1176.45 MHz). The passive receiver was equipped with two channels to collect direct and reflected signals. Particularly, the reference channel used a low-gain antenna while the surveillance channel used a higher gain antenna pointed toward the surveyed area. In order to have a reference ground truth for comparison, the following analysis focuses on targets of opportunity equipped with Automatic Identification System (AIS) whose messages were recorded during all the acquisitions.

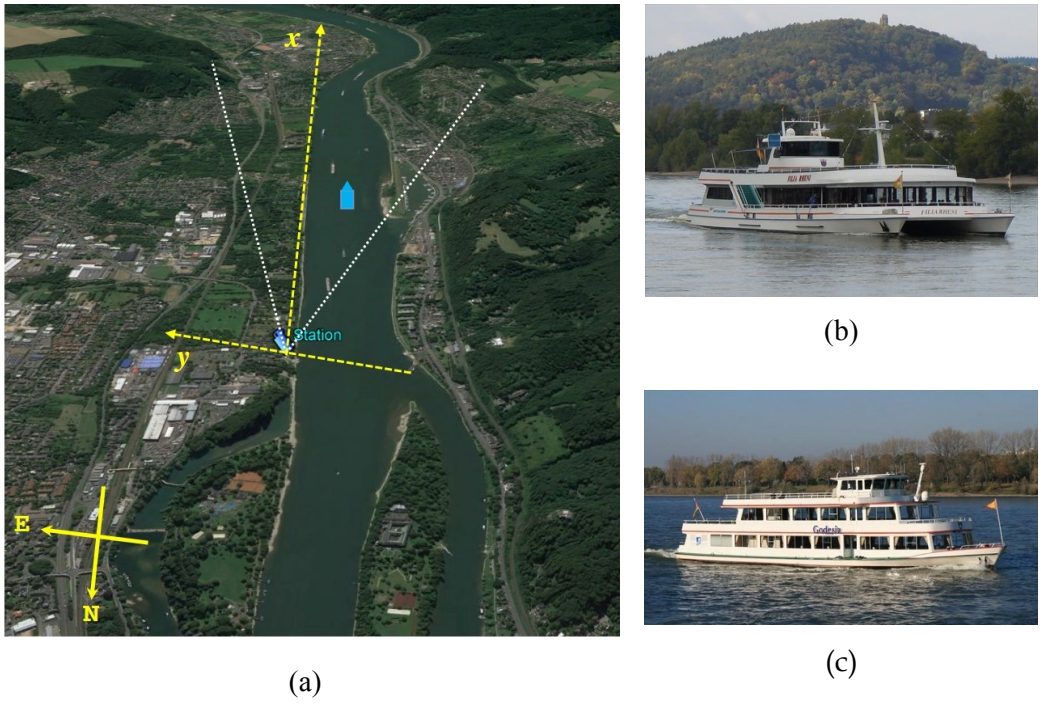

Figure 5.7 - River navigation experimental trials. (a) Acquisition geometry. (b) 'Filia Rheni' optical photograph [72]. (c) 'Godesia' optical photograph [72].

TABLE 5.II - SHIPPING RIVER EXPERIMENTAL CAMPAIGN – TRACKED SATELLITES

Parameter		**Unit**	**Value**
Satellite 1	Number	-	GSAT0210
	Ranging code	-	E01 (E5a-Q)
	Azimuth angle	deg	164.38 ~ 163.75
	Elevation angle	deg	9.17 ~ 9.14
Satellite 2	Number	-	GSAT0214
	Ranging code	-	E05 (E5a-Q)
	Azimuth angle	deg	-115.90 ~ -116.32
	Elevation angle	deg	36.02 ~ 35.48

5.3.1 Scenario 1: River shipping

In the first experimental campaign the receiver was located on the Rhine riverside near Bonn, observing the vessel traffic mainly composed by barges, car ferries and cruise ships. Figure 5.7 (a) shows the geometry of the acquisition, during which the surveillance antenna was pointed toward South. In a two mins long acquisition, the two passenger ferries 'Filia Rheni' (Figure 5.7 (b)) and 'Godesia' (Figure 5.7 (c)), with size (length overall × breadth extreme) equal to 42m × 11m and 38.6m × 8.6m, respectively, were moving away from the receiver. Two Galileo satellites were correctly tracked during the acquisition, whose parameters are listed in Table 5.II.

Figure 5.8 shows the RD maps pertaining a single frame for the two acquired satellites. The 0 dB denotes the mean background disturbance level. As it is apparent, in both the images we cannot observe any bright spots that can be associated with a target. The short CPI considered did not suffice to bring the target out from the disturbance background, highlighting the necessity to achieve a further integration gain by exploiting longer integration times and multiple baselines.

Figure 5.9 shows the bistatic multi-frame RD maps obtained by the non-coherent integration of N = 10 frames by applying the TMC (and skipping in this case the MSC) and selecting the branch of the Doppler rate bank providing the highest SNR. Particularly, the highest SNR is reached on the same branch for both targets: this is in agreement with the recorded AIS information stating that the Doppler rate difference between the two targets was lower than the step in (4.7). In Figure 5.9 (a) pertaining sat. 1, two bright spots are well visible. Comparing with the AIS information, these correspond to 'Filia Rheni' and 'Godesia'. In Figure 5.9 (b), pertaining sat. 2, only one clear intensity peak can be observed, corresponding to 'Filia Rheni', while 'Godesia' seems being not detectable in this bistatic map, likely due to a lower bistatic RCS resulting from sat. 2 perspective.

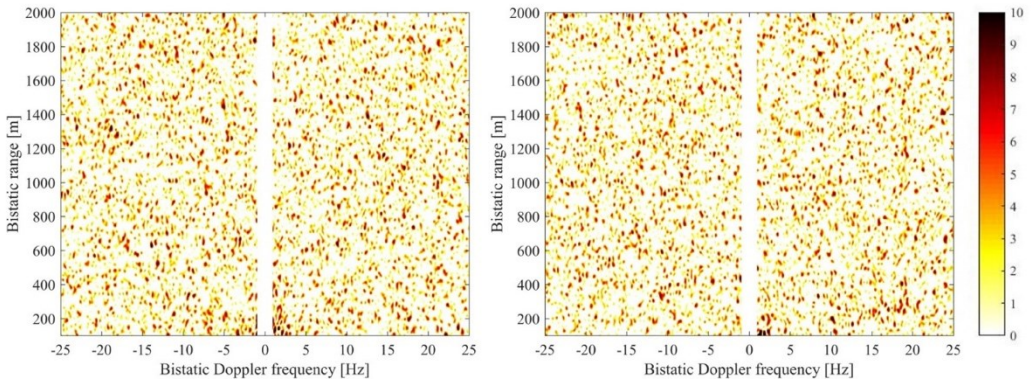

(a) (b)

Figure 5.8 - Bistatic single frame RD maps. (a) sat. 1. (b) sat. 2.

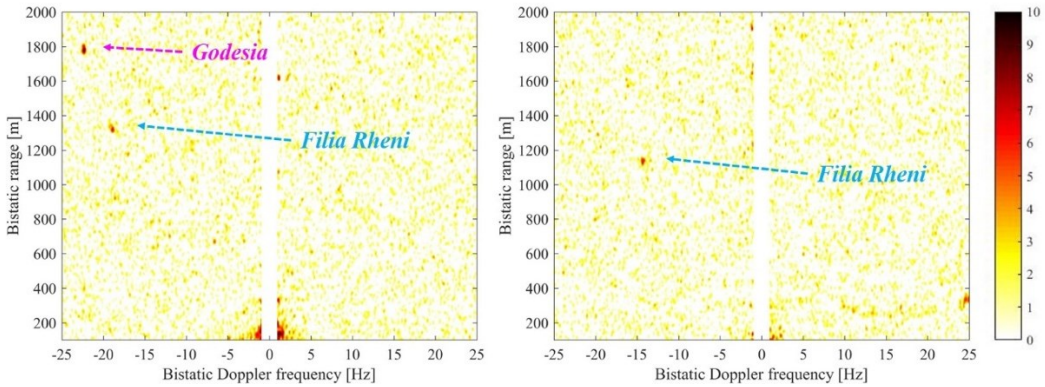

(a) (b)

Figure 5.9 - Bistatic multi-frame RD maps. (a) sat. 1. (b) sat. 2.

In the long-time bistatic RD maps in Figure 5.9, 'Filia Rheni' energy was concentrated around the positions (1314 m, -18.9 Hz) and (1129 m, -14.3 Hz) for sat.1 and sat. 2, respectively. As a consequence, the two maps cannot be directly summed to improve the SNR. The whole procedure comprising both TMC and MSC has been then applied to the data for the Doppler rate maximizing the SNR. Figure 5.10 shows the resulting RD maps when the 'Filia Rheni' angular values provided by (5.15) have been considered. In the figure, the axes represent the range and Doppler pertaining the target-to-receiver distance and where 0 dB denotes again the mean

disturbance level. In particular, Figure 5.10 (a) and b show the long-time monostatic maps. The blue boxes highlight the area where the target energy is expected and we can observe that after the MSC it locates around the same position (725m, -9.8 Hz). Therefore, SNR improvement can be obtained in the corresponding long-time multistatic RD map, shown in Figure 5.10 (c). Comparing the three images, a lower level of the disturbance fluctuations can be appreciated in the multistatic image, while the peak power is the mean of the peak powers in the individual long-time bistatic images. Even though the exploitation of a single couple of bistatic links does not allow to considerably enhance the detection performance of the system, the provided results shows the effectiveness of the method: by considering a larger number of transmitters, even considering multiple fully lunched constellations, the SNR improvement could suffice to enable detections of lower observable targets.

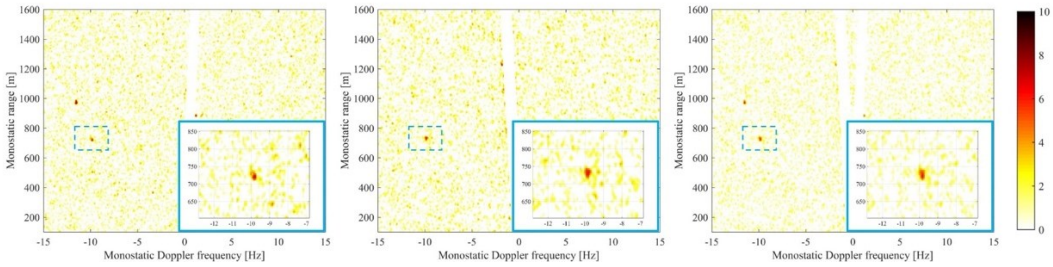

Figure 5.10 - Space-aligned long-time bistatic and multistatic RD maps corresponding to 'Filia Rheni' actual kinematics. (a) long-time monostatic map sat. 1. (b) long-time monostatic map sat. 2. (c) long-time multistatic map.

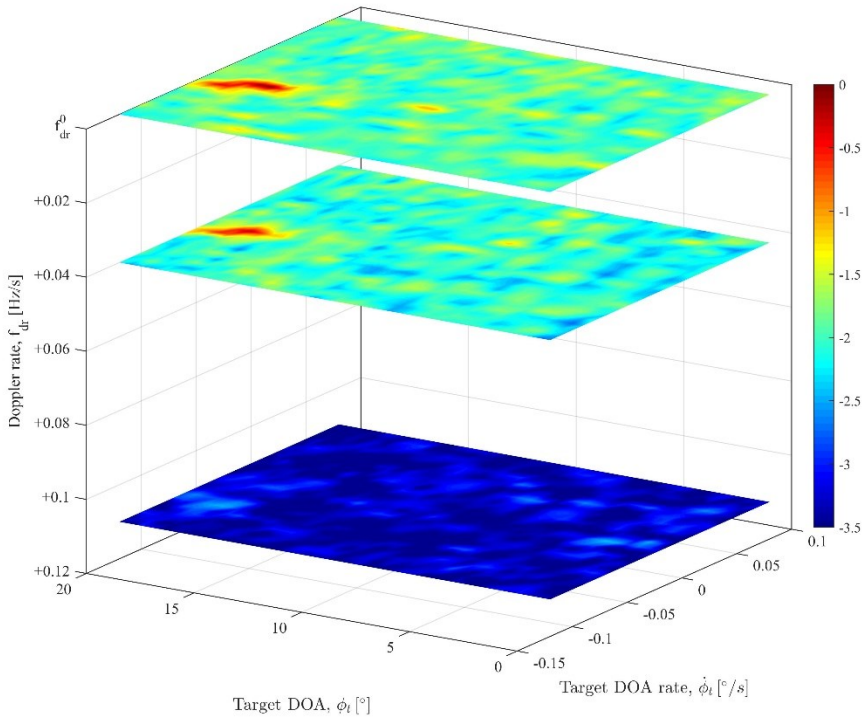

Figure 5.11 - 'Filia Rheni' integration gain cost function $G(f_{dr}, \phi_t, \dot{\phi}_t)$.

As well as the improvement of the detection performance, the proposed method enables the joint localization of the target by looking for the tested angular values providing the maximum gain. Particularly, Figure 5.11 shows the function G in (5.15) (in log-scale) for three different values of the tested Doppler rate when the first 30 s of the acquisition have been selected (T_f = 3 s, N = 10). The figures have been normalized to the maximum value, which is found in the slice on the top corresponding to the nominal Doppler rate f_{dr}^0. Moving to the bottom slices (increasing offset with respect to f_{dr}^0), we can observe a lower mean level due to the worse temporal integration gain provided by the TMC according to wrong values of the Doppler rate. At the same time, the spatial integration gain provided by the MSC reaches its maximum in correspondence of a specific couple $(\phi_t, \dot{\phi}_t)$ in the slice pertaining f_{dr}^0. Such couple is retained as the estimated values of the target

DOA and its rate of change. From the estimated monostatic range and DOA the target Cartesian coordinates are obtained. Figure 5.12 shows the estimated instantaneous target positions obtained by means of this procedure applied over consecutive integration windows with an interval of 10 s between two consecutive windows. In particular, Figure 5.12 (a) shows the estimated track in the (x, y) plane, whereas Figure 5.12 (b) reports the same information in the geographical plane. As it is apparent, a good agreement between the estimated track and the AIS ground truth has been obtained, with a Root Mean Square Error (RMSE) between the two trajectories of about 20 m, namely even lower than the target maximum extension.

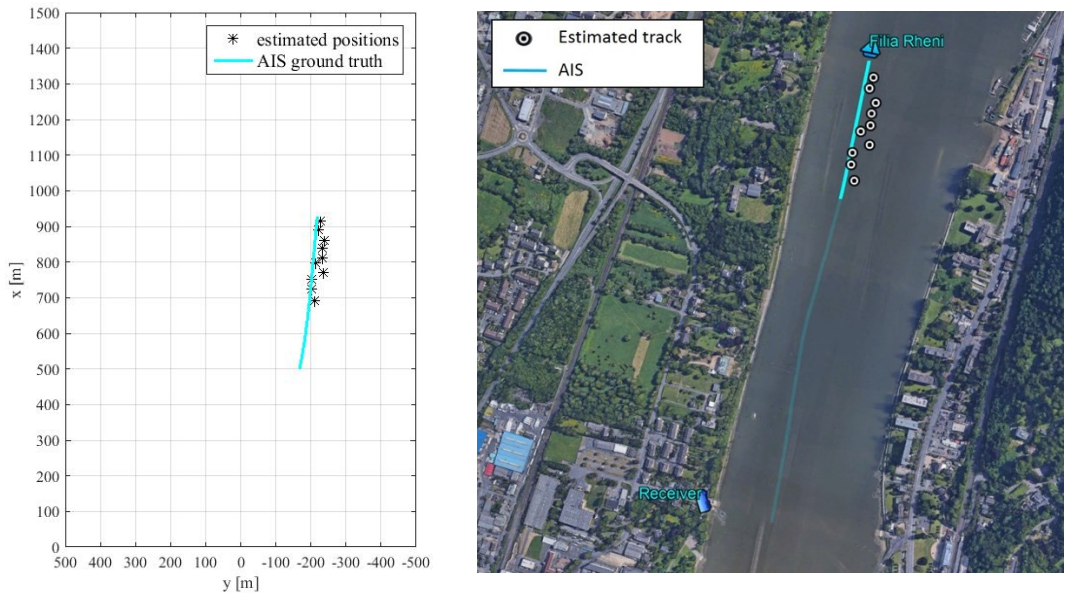

(a) (b)

Figure 5.12 - 'Filia Rheni' track. (a) Cartesian plane. (b) Geographical plane.

5.3.2 Scenario 2: Port operations

The second acquisition campaign was conducted in the premises of the Marghera Port, Italy. The receiver was located at the entrance of the port area, acquiring the signals scattered by the commercial vessels sailing in the port entry/exit channel, see Figure 5.13 (a). Marghera Port is a commercial harbour and therefore the large majority of passing vessels were massive container ships and tankers. Figure 5.13 (b) shows an optical photograph of one of such targets, 'Fairpartner' (143.1m × 26.6m), which was observed entering in the port terminal in a 3 mins long acquisition during which four Galileo satellites were correctly tracked. Table 5.III lists the parameters of the tracked satellites.

(a) (b)

Figure 5.13 - Port operations experimental trials. (a) Acquisition geometry. (b) 'Fairpartner' optical photograph [72].

Due to the large size of the considered target of opportunity, it is expected that even a conventional short time MTD approach can suffice to detect the target. Figure 5.14 shows the single frame bistatic RD maps (T_f = 3 s) for the different baselines, where the target position provided by the AIS data is highlighted by the black dotted circle. It can be seen that with the sat. 1, a large SNR is achieved, with a peak power of about 30 dB above the mean disturbance level. Nevertheless, by considering the remainder satellites, much lower peak powers are obtained. The

target is barely visible with sat. 2 and sat. 3, while it is completely buried in the disturbance background with sat. 4. The different SNR levels observed at the different bistatic channels are a further confirmation of the diversity gain provided by the GNSS, where the multiple perspectives enhance the possibility to detect a target.

TABLE 5.III - PORT OPERATIONS EXPERIMENTAL CAMPAIGN – TRACKED SATELLITES

Parameter		Unit	Value
Satellite 1	Number	-	GSAT0206
	Ranging code	-	E30 (E5a-Q)
	Azimuth angle	deg	159.45 ~ 158.95
	Elevation angle	deg	49.04 ~ 50.26
Satellite 2	Number	-	GSAT0207
	Ranging code	-	E07 (E5a-Q)
	Azimuth angle	deg	-51.83 ~ -51.14
	Elevation angle	deg	65.84 ~ 66.84
Satellite 3	Number	-	GSAT0211
	Ranging code	-	E02 (E5a-Q)
	Azimuth angle	deg	67.91 ~ 66.36
	Elevation angle	deg	49.67 ~ 49.23
Satellite 4	Number	-	GSAT0208
	Ranging code	-	E08 (E5a-Q)
	Azimuth angle	deg	102.13 ~ 103.46
	Elevation angle	deg	56.15 ~ 55.26

As a proof-of-concept experiment, let us suppose that signals from sats. 2, 3 and 4 only have been acquired. It could be shown that a longer integration time would make possible to reinforce the target power in the individual bistatic links,

enabling the target detections in all the long-time bistatic RD maps. However, as highlighted by the analysis in section 5.2.1, the number of integrated frames could be in principle traded with multiple baselines to reach comparable detection performance, increasing the robustness of the TMC. We consider here the combination of the three single-frame RD maps after the MSC pertaining the actual target angular values, providing the single-frame multistatic map shown in Figure 5.15. As clearly visible, the incoherent summation of the aligned maps lowers the fluctuations of the disturbance background while, at the same time, strengthening the target energy: a clear spot is visible in the figure surrounded by a 'calm' background, so that a high probability of target detection is expected even for low false alarm rate values. In particular, Table 5.IV lists the probability of detection obtained for these short-time RD maps in the bistatic and in the multistatic cases resulting from the theoretical formulations reported in section 5.2.1 evaluated for the estimated local SNRs (assuming they correspond to the average values). It can be seen that, even setting a low probability of false alarm, high detection rates can be obtained in the multistatic map, whereas the strong background fluctuations in the bistatic images entail low probability to detect the target. In addition, the P_d^{QI} is close to the maximum P_d^{LRT} foreseen by the LRT, thus proving the effectiveness of the QI operator to be used in practical applications.

TABLE 5.IV - ESTIMATED PROBABILITY OF DETECTION FOR 'FAIRPARTNER' SHORT-TIME BISTATIC AND MULTISTATIC RD MAPS

P_{fa}		sat.2	sat.3	sat.4	sat.2+sat.3 +sat.4
10^{-3}	QI	66.7 %	64.3 %	56.2 %	95.8 %
	LRT	67.3 %	64.5 %	57.2 %	95.9 %
10^{-4}	QI	58.2 %	55.5 %	46.4 %	92.9 %
	LRT	58.4 %	55. 8%	46.6 %	93.0 %
10^{-5}	QI	50.9 %	47.9 %	38.2 %	89.6 %
	LRT	51.4 %	48.5 %	38.4 %	89.8 %

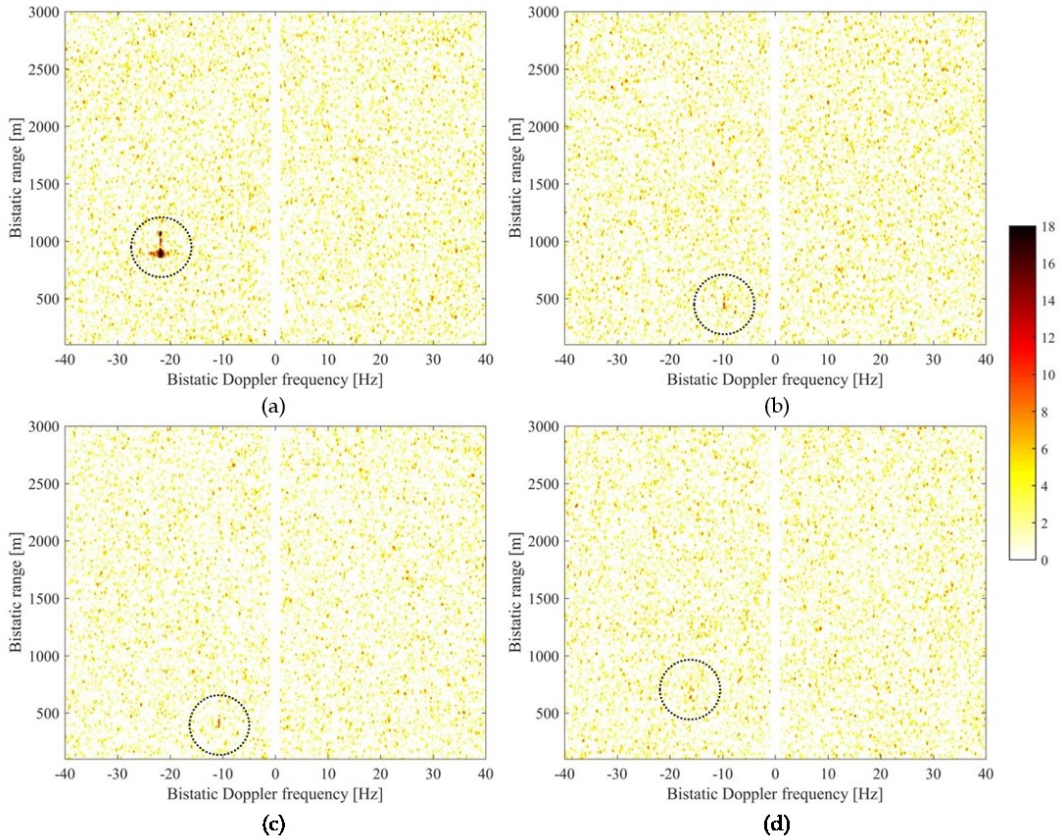

Figure 5.14 - 'Fairpartner' single frame bistatic RD maps. (a) sat. 1. (b) sat. 2. (c) sat. 3. (d) sat. 4.

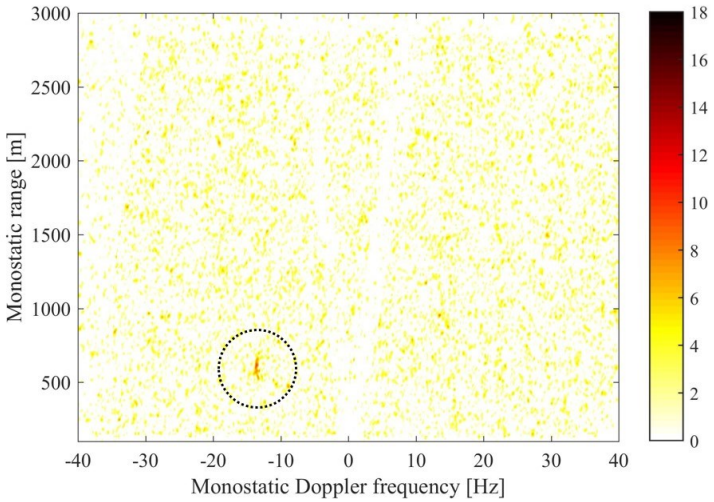

Figure 5.15 - 'Fairpartner' single frame multistatic RD map using satellites 2,3,4.

Finally, Figure 5.16 (a) shows the estimated positions of 'Fairpartner' reported in the geographical plane and compared with the AIS ground truth. The short-time (N = 1) maps provided by all the available satellites have been employed, considering successive integration windows with interval 10 s. The good agreement between the actual and estimated track confirms the effectiveness of the localization capability of the technique. In particular, a RMSE of about 38 m was found, further validating the proposed approach. A further improvement could be achieved considering also an integration over multiple frames: N = 10 is chosen here as example. The estimated tracks for the two cases (N = 1 and N =10) are compared in the Cartesian plane (Figure 5.16 (b)). An improvement in the track estimation can be observed by exploiting both the space and time domains, as confirmed also by the RMSE reducing at about 24 m.

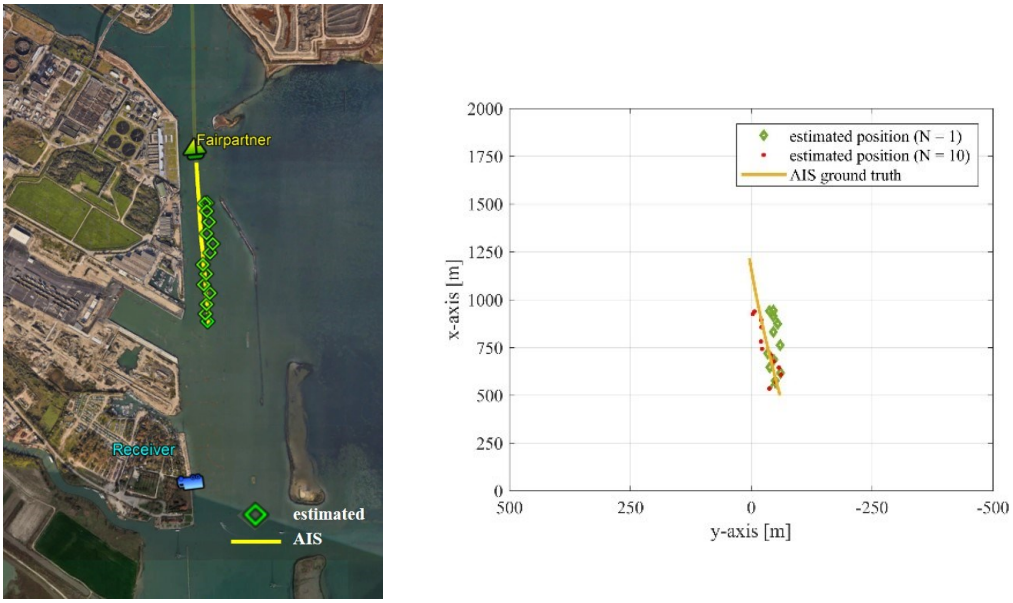

(a) (b)

Figure 5.16 - 'Fairpartner' estimated positions. (a) Geographical plane (N = 1). (b) Cartesian plane.

Chapter 6

Features extraction

In this Chapter, the possibility to extract features of the detected targets is being investigated. Usually, after a target is detected, the radar user attempts to identify it by making use of automatic target recognition procedures, and this goal can be achieved by ship imagery obtained with the well-known principle of the Inverse Synthetic Aperture Radar (ISAR) [73]. With this objective in mind, an experimental study has been conducted to show that, depending on the type of target motion, the range occupation or the Doppler gradient observed by the GNSS-based passive radar over proper CPIs could allow the rough identification of the dimensional class of the detected ship. In the following section, the extraction of the ship features is described. Then some results against real data are presented to show the potentiality of obtaining information about the detected target.

6.1 Ship target feature extraction

The block diagram in Figure 6.1 highlights the three main steps composing the overall processing chain. As already shown in Chapter 5, the target can be jointly detected and located in the Cartesian plane exploiting multiple satellites. In this way, from the joint detection and localization over successive time instants the target track can be obtained. At this stage, the information concerning the motion of the target can be derived directly from the data and needed by features extraction stage (as it will explained in the following).

Figure 6.1 - Main steps for feature extraction

While searching the ship, the techniques presented in Chapter 4 and Chapter 5 compensate the motion of the target fulcrum over consecutive frames. That is to say, they take into account the fulcrum trajectory $\{x_{REF}(u), y_{REF}(u)\}$. Therefore, the target fulcrum is imaged in the RD domain at a specific range and Doppler frequency that depends on the target kinematics at the reference time instant pertaining the overall integration window.

To calculate the target features, let us consider the ship target characterized by fictitious point scatterers A and B identifying the edges of the target and following a trajectory characterized by the heading angle $\theta(u) = tg^{-1}[\dot{x}_{REF}(u)/\dot{y}_{REF}(u)]$ measured clockwise from y-axis and variable during the acquisition time, as is shown in Figure 6.2. Changes in the motion direction are taken into account by considering the target rotating at an angular velocity $\omega_{rot}(u) = \dot{\theta}\,(u)$ around a vertical rotation axis (i.e. rotation normal to the ground plane). The direction of arrival of the target relative to receiver is ϕ_t, measured clockwise from the LOS. Figure 6.2 shows the angles ϕ_{Tx-Tg} and ψ_{Tx-Tg} that define the position of the transmitter (x_{Tx}, y_{Tx}, z_{Tx}) with respect to the target. The angle $\phi_{Tx-Tg} = -tg^{-1}\left\{\frac{y_{Tx}-R_R\cos\phi_t}{x_{Tx}-R_R\sin\phi_t}\right\}$ is measured in the x-y plane clockwise from the x-axis. The angle $\psi_{Tx-Tg} = tg^{-1}\left\{\frac{z_{Tx}}{\sqrt{(x_{Tx}-R_R\sin\phi_t)^2+(y_{Tx}-R_R\cos\phi_t)^2}}\right\}$, which defines the elevation of the satellite, is measured from the x-y plane. The information relating to the target position and velocity can be obtained after the target localization and tracking in the x-y plane, following the steps shown in Figure 6.1.

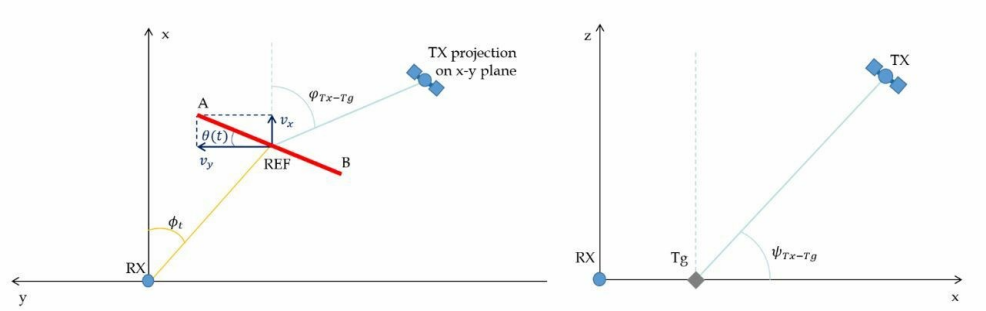

Figure 6.2 - Local reference system.

6.1.1 Range domain feature extraction

In the case of dominant radial motion, target length can be estimated from the number of range cells over which target energy spans. As seen in Chapter 5, the target-to-receiver range R_m can be obtained from the bistatic range R_R as:

$$R_m \approx R_R \cdot [1 - \cos(\theta_m)\cos(\phi_m - \phi_t)] = R_R \cdot \zeta_m(\phi_t) \tag{6.1}$$

where $\zeta_m(\phi_t)$ is a target DOA-dependent scale factor.

In the same way, the bistatic range extension measure of the target L_{exp} can be converted into monostatic measure and the target length can be retrieved by exploiting also the heading information, as follows:

$$L_{Tg} = L_{exp} \cdot \zeta_m(\phi_t)/cos\theta^0 \tag{6.2}$$

where the target range occupation L_{exp} is measured on the bistatic RD map and θ^0 is the target heading at the image time $u = 0$. Both target DOA ϕ_t and heading θ^0 can be made available from the detection and tracking stages.

6.1.2 Cross-range domain feature extraction

The target instantaneous Doppler bandwidth B_d (defined as the range of Doppler frequency spans from point A to point B) is composed by two contributions, one related to the receiver and the other one related to the transmitter.

As usual in ISAR literature, the generic target motion can be decomposed as the translation of a reference point (fulcrum) and the rotation of the target around that point. Therefore with respect to the receiver, both rotational and translational motions are expected to contribute to B_d. By considering a ship target with length $\overline{\mathrm{AB}}$ = L and scatterers A and B at distance L/2 from the target fulcrum (*REF* in Figure 6.2), the Rx-related instantaneous Doppler bandwidth due to target rotation can be written as:

$$B'_{d,r} = -\left(\frac{1}{\lambda}\right)\overline{AB}\,cos(\theta^0 - \phi_t)\,\omega^0_{rot} \tag{6.3}$$

where $\omega^0_{rot} = \dot{\theta}(0)$ is the angular velocity calculated at the image time $u = 0$ and $\overline{AB}\,cos(\theta_t - \phi_t)$ is the projection of $\overline{AB}$ on the normal to the line joining the receiver and the target reference point. The Rx-related instantaneous Doppler bandwidth due to target translation can be proven being equal to:

$$B_{d,t} = -\frac{|V|}{\lambda R_0}\overline{AB}cos^2(\theta^0 - \phi_t) \tag{6.4}$$

obtained by calculating the directional derivative of the Doppler frequency along the velocity vector.

Concerning the transmitter, due to the very large distance between the target and the transmitter, only the rotation motion contributes to instantaneous Doppler bandwidth, [50]. Similarly to eq. (6.3), this contribution can be evaluated as

$$B''_{d,r} = -\left(\frac{1}{\lambda}\right)\overline{AB}\,cos\left(\theta^0 - \phi_{Tx-Tg} - \pi\right)\omega^0_{rot}\,cos(\psi_{Tx-Tg}) \tag{6.5}$$

where $\overline{AB}\,cos\left(\theta^0 - \phi_{Tx-Tg} - \pi\right)$ is distance of the points A and B from the line joining the transmitter and the target reference point and θ^0_m is the out-of-plane angle between the (x, y) plane and the satellite at the reference time $u = 0$. In eq. (6.5), the projection according to the ψ_{Tx-Tg} value allows considering the effective rotation rate with respect to the transmitter LOS, [73].

The total instantaneous Doppler bandwidth is the summation of the three components calculated above:

$$B_d = B_{d,t} + B_{d,r}{}' + B_{d,r}{}' \tag{6.6}$$

This Doppler bandwidth can be compared to the Doppler resolution (1/CPI) to obtain the number of Doppler resolution cells occupied by the target: potentialities for feature extraction arise when $B_d \gg 1/CPI$ so that different target scattering centers can be separated in the Doppler domain and therefore an image or at least a Doppler/cross-range profile is obtained, [74]. Further, the target size could be retrieved by properly scaling the Doppler frequency axis. To measure the target length $\overline{AB}$, the Cross-range axis can be obtained by multiplying the Doppler axis by the factor equal to:

$$\begin{aligned} k = &-\frac{|V|}{\lambda R_0} cos^2(\theta^0 - \phi_t) - \frac{|V|}{\lambda R_0} \overline{AB} cos^2(\theta^0 - \phi_t) \\ &- \left(\frac{1}{\lambda}\right) cos\left(\theta^0 - \phi_{Tx-Tg} - \pi\right) \omega_0 \, cos(\psi_{Tx-Tg}) \end{aligned} \tag{6.7}$$

where, as done in sub-section 6.1.1, the θ^0, ϕ_t and ω_0 values are assumed available from the previous stages.

6.2 Experimental results

The potentialities and the effectiveness of the proposed feature extraction approach are now demonstrated on experimental datasets. Proof-of-concepts experiments were conducted in maritime scenarios considering two different kinds of targets: both datasets have been presented already in previous chapters for different purposes, but a brief description is again given here for the sake of clearness.

The experimental campaign was conducted by University of Birmingham and the corresponding datasets provided to University of Rome in the framework of the H2020 spyGLASS project, [34].

6.2.1 Experimental campaign with large size target

The first dataset comes from the maritime experimental campaign conducted in the eastern coastal area of Plymouth harbour in UK and involving two Galileo satellites, see Figure 6.3 (a). The experimental receiver [Figure 6.3 (b)] was equipped with two RF channels for recording direct and reflected signals, respectively. The target of opportunity was the commercial Brittany ferry shown in Figure 6.3 (c), having length L = 184 m and width W = 25 m. The automatic identification system (AIS) information was recorded and used as ground truth to validate the experimental results. Table 6.I shows the experimental and signal processing parameters. This acquisition concerns a high size and high RCS target, therefore a short integration time suffices to detect it, (sub-section 4.3.1). Since the target motion compensation procedures in Chapter 4 and Chapter 5 relocate the target energy over the same RD position, they, in principle, do not affect the imagery. Therefore, for feature extraction purposes only and provided that a single frame suffices (high-RCS targets), we can consider the observation time limited to the CPI, namely the reference frame duration.

Figure 6.7 and Figure 6.9 show the RD images achieved over a CPI of 3 s around two different reference time instants, one chosen in case of dominant radial motion and the other in case of tangential motion of the target with respect to the receiver. The reference time instants are chosen around T_{REF} = 10 s for radial motion case and T_{REF} = 120 s for tangential motion case and they are highlighted in Figure 6.4 and Figure 6.5, which show the ground truth compared to the tracks obtained by means of the single-channel M-MTD technique (sub-section 4.3.1). The results are presented for the two satellites in visibility and they show the different response of the target for the two satellites. The different RCS of the target observed in the two cases depends on the different geometry with which the target is observed. In general, the channel chosen for the extraction of target characteristics is expected to have a good level of SNR.

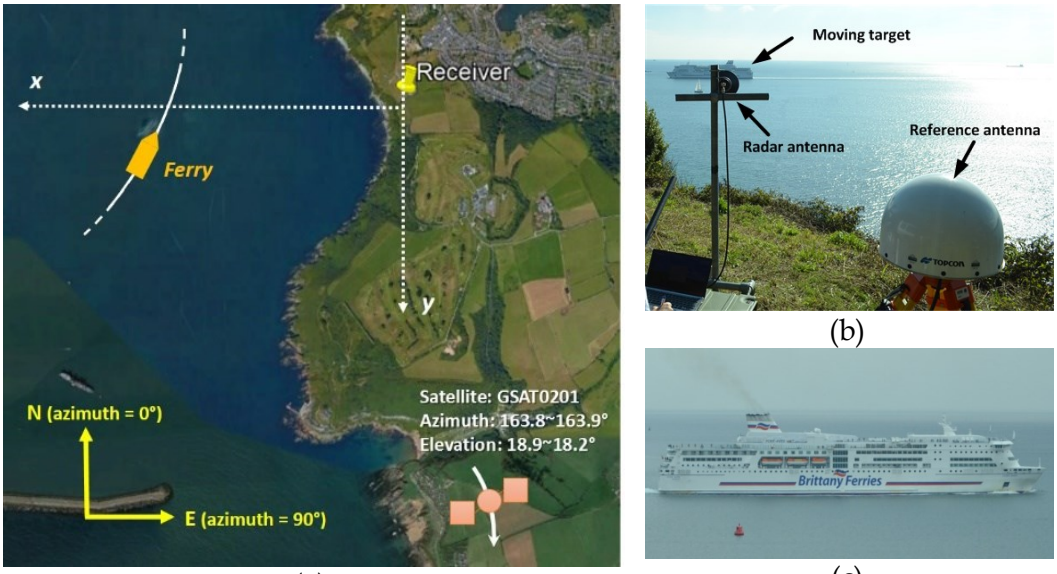

Figure 6.3 - (a) Schematic diagram of the experimental GNSS-based radar data acquisition geometry, (b) the experimental setup of the receiving system and (c) the optical photograph of the ferry.

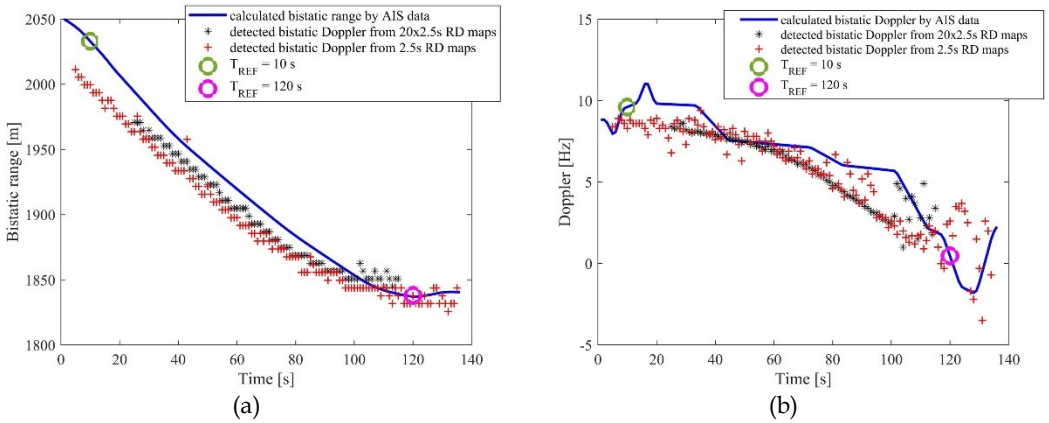

Figure 6.4 – Time instants chosen for the analysis indicated on (a) bistatic range for satellite 1 and (b) bistatic Doppler for satellite 1

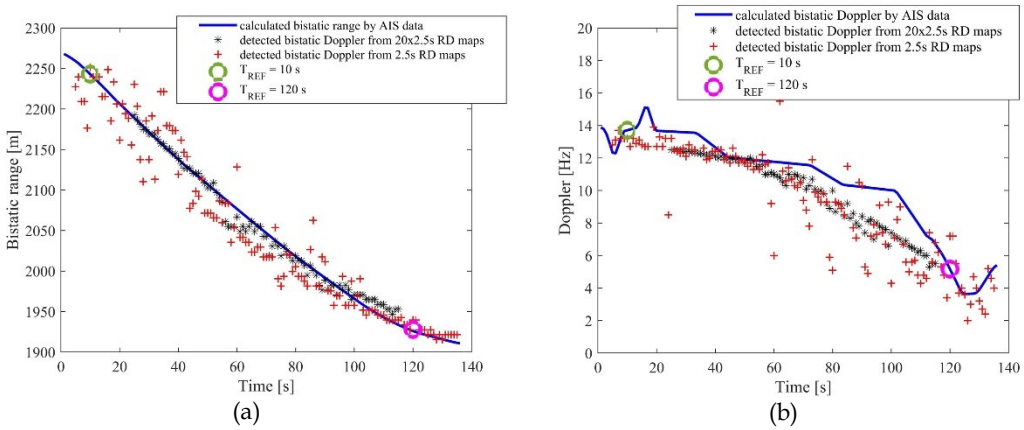

Figure 6.5 - Time instants chosen for the analysis indicated on (a) bistatic range for satellite 2 and (b) bistatic Doppler for satellite 2

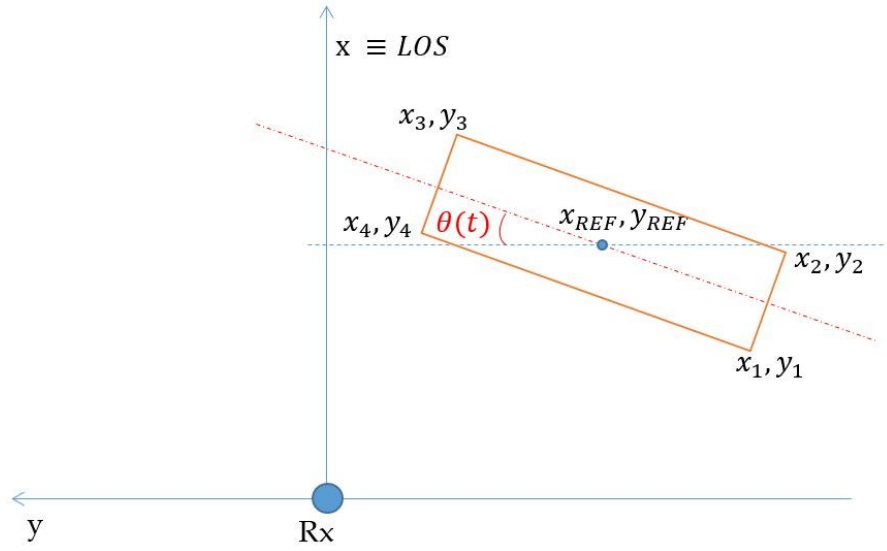

Figure 6.6 - Target shape

The following RD images have been obtained by applying to the range compressed data a proper dechirping followed by a Fast Fourier Transform. The dechirping is performed by considering $f_{dr} = 0.111\ Hz/s$ for radial motion case and $f_{dr} = 1\ Hz/s$ for tangential motion case. These values of Doppler rate are chosen by

testing the whole Doppler rate bank and selecting the branch that providing the best contrast in the images. In the images, 0 dB denotes the mean background power. The maximum value represented in each figure depends on the maximum return of the target, hence it is different for each image. For comparison, the figures show also the area for the RD plane where the target contribution is expected: this area (inside the white frame) is obtained by assuming the ideal shape modelled by a $L \times W$ rectangle with orientation depending on the target heading (Figure 6.6) and by propriety projecting this ideal target at the RD plane. Particularly, the four vertexes of the rectangle in Figure 6.6 have been projected on the RD plane ('*' white markers) by firstly evaluating their position on the (x, y) plane according to

$$\begin{bmatrix} x_i(t) \\ y_i(t) \end{bmatrix} = \begin{bmatrix} cos\ \omega_{rot} t & sin\ \omega_{rot} t \\ -\ sin\ \omega_{rot}\ t & cos\ \omega_{rot} t \end{bmatrix} \begin{bmatrix} x_i^0 - x_{REF}^0 \\ y_i^0 - y_{REF}^0 \end{bmatrix} + \begin{bmatrix} x_{REF}(t) \\ y_{REF}(t) \end{bmatrix}, \quad i = 1 \dots 4 \qquad (6.8)$$

where $\{x_{REF}(t), y_{REF}(t)\}$ and ω_{rot} are retrieved from AIS data and there using these coordinates inside eqs. (3.4) and (3.5).

TABLE 6.I – EXPERIMENTAL AND SIGNAL PROCESSING PARAMETERS

Parameter		Value
Sat 1	Number	GSAT0201
	Ranging code	PRN18 (E5a-Q primary code)
	Bistatic angle	97° ~ 85°
	Azimuth (relevant to North)	163.8° ~ 163.9°
	Elevation (relevant to HC antenna)	18.9° ~ 18.2°
Sat 2	Number	GSAT0203
	Ranging code	PRN26 (E5a-Q primary code)
	Bistatic angle	91° ~ 83°
	Azimuth (relevant to North)	158.1° ~ 158.4°
	Elevation (relevant to HC antenna)	49.6° ~ 48.7°
Carrier frequency		1176.45 MHz

Sampling frequency	50 MHz
Dwell time	145 second
Pulse repetition interval	1 millisecond
Coherent processing interval	3 second

The RD maps obtained in case of radial motion is shown in the Figure 6.7. The bistatic range could be measured directly from the image and consequently the target length is obtained with eq. (6.2). The calculated length is 132 m and 153 m for the satellite 1 and 2, respectively. The results are in good agreement with the target length.

For the tangential motion case, the overall bandwidth calculated with (6.6) is equal 5.6 Hz and 5 Hz with reference to Figure 6.9 (a) and (b), respectively. Therefore, the Doppler cells occupied by the target are 17 and 15, respectively. As evident, the area bounded by the projected rectangular shape fits well with the target dimension demonstrating the potentialities for feature extraction. Starting from the AIS information, it is possible to perform the scaling of the Doppler axis to achieve the cross-range domain with eq. (6.7) and to measure the target length. Figure 6.10 shows the target occupation in agreement with the target length. An autonomous procedure could be obtained by calculating the target kinematic parameters directly from the data.

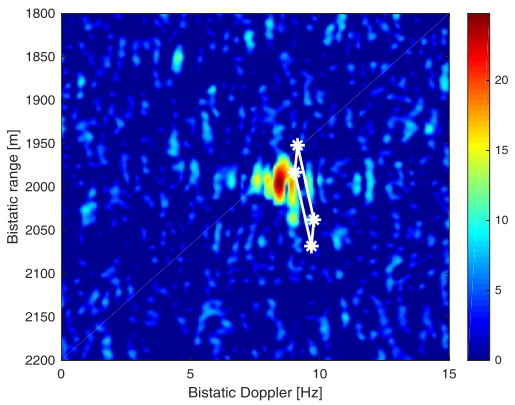

(a)

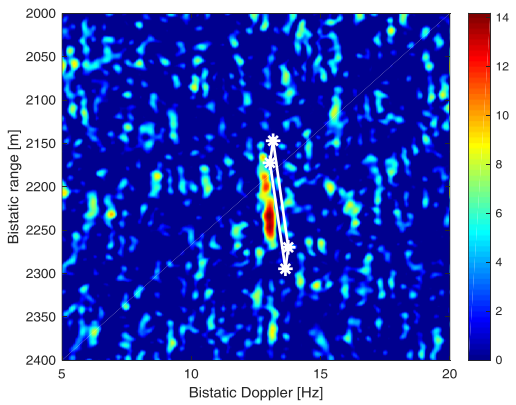

(b)

Figure 6.7 - Calculated corner point superimposed on ship RD images obtained for (a) satellite 1 and (b) satellite 2 in case of target radial motion

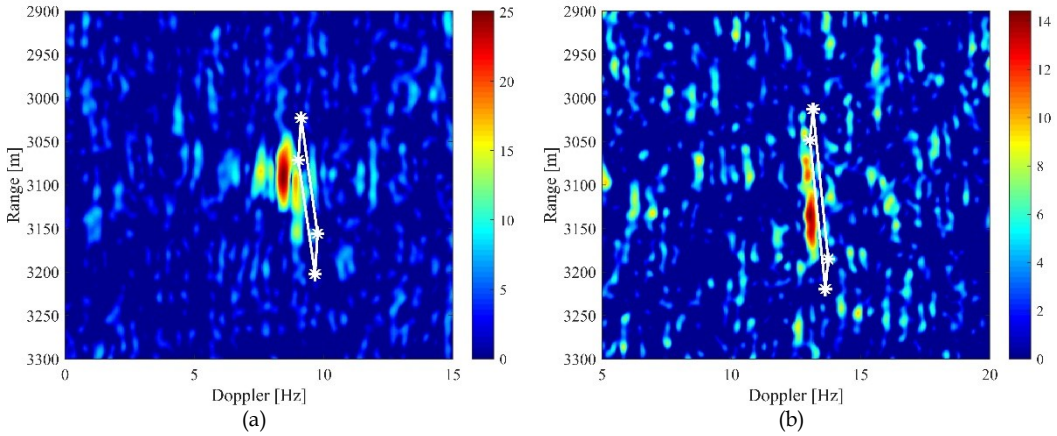

Figure 6.8 - Images after range axis scaling obtained for (a) satellite 1 and (b) satellite 2 in case of tangential motion

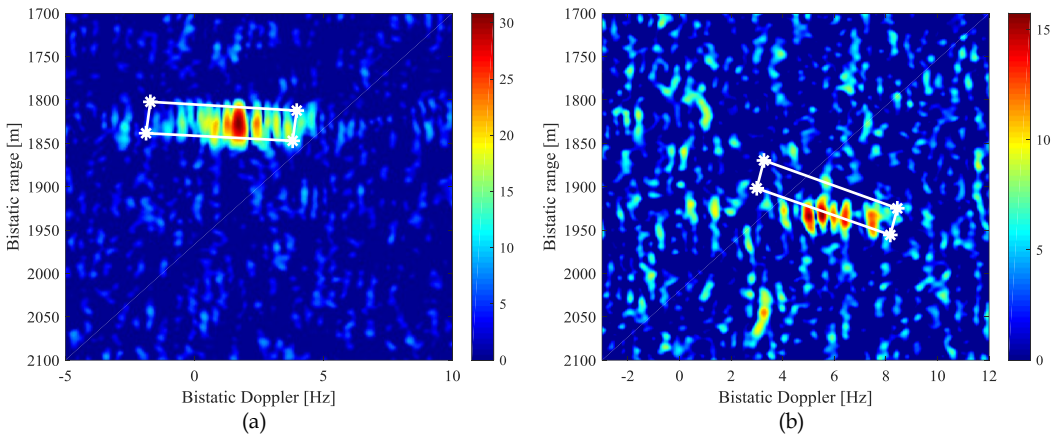

Figure 6.9 - Calculated corner point superimposed on ship RD images obtained for (a) satellite 1 and (b) satellite 2 in case of target tangential motion

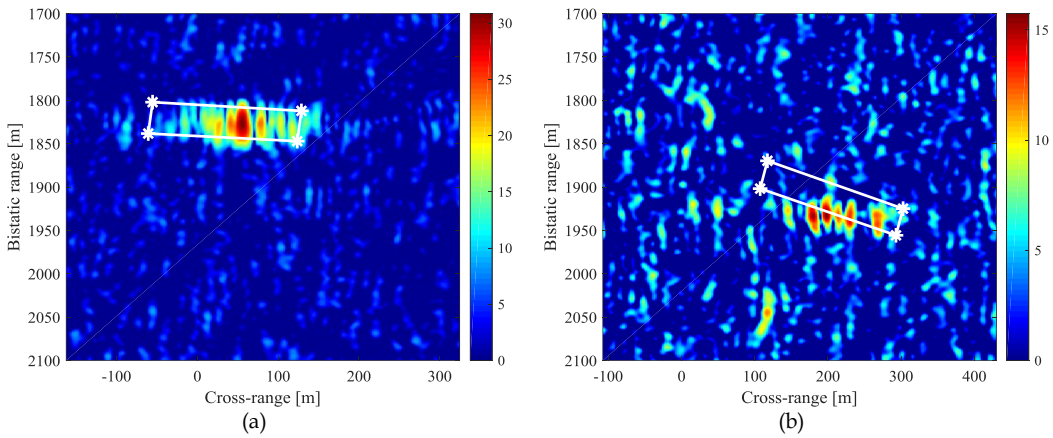

Figure 6.10 - Images after cross-range axis scaling obtained for (a) satellite 1 and (b) satellite 2 in case of tangential motion

6.2.2 Experimental campaign with small size target

To carry out a second experimental campaign, the receiving hardware [Figure 6.11 (a)] was placed in a coastal area of Portsmouth International port (UK). Galileo satellite is considered as transmitter of opportunity. In the Figure 6.11 (b) and (c) are given the optical photographs of the two targets in the area under surveillance: the passenger ferry 'St Faith' (length: 77.05 m, beam: 17.2 m, draught: 2.48 m) and the catamaran 'HSC Wight Ryder I' (length: 41 m, beam: 12 m, draught: 1.60 m). The target 'Ryder' is selected for the following analysis. The real track used as truth on the ground to validate the results is obtained by AIS information. The experimental and processing parameters are listed in Table 6.II. The target has a modest size compared to the ferry considered in the previous section. For this reason, the RD maps in Figure 6.13 are obtained over long integration time by applying TMC procedure (Chapter 4).

The target crosses the radar LOS, since its motion is mainly radial. For this reason, the target extension measure is calculated in the cross-range domain.

TABLE 6.II - EXPERIMENTAL AND SIGNAL PROCESSING PARAMETERS OF THE SECOND MARITIME ACQUISITION CAMPAIGN

	Parameter	Unit	Value
Satellite	number	-	GSAT0202
	carrier frequency	MHz	1176.450
	Chip rate	MHz	10.230
	azimuth (clockwise from N)	deg	64.86 ~ 62.00
	elevation (relevant to HC)	deg	24.87 ~ 24.06
Processing parameters	sampling frequency	MHz	50
	pulse repetition interval	ms	1
	overall observation interval	s	286
	frame duration	s	3
	non-coherent integrated frames	-	5

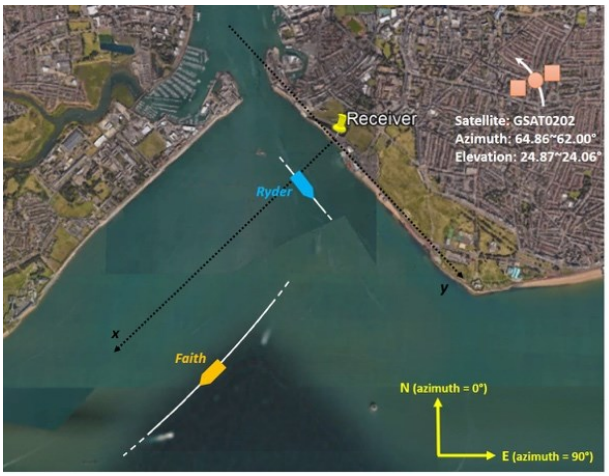

(a)

(b)

(c)

Figure 6.11 - Second maritime experimental campaign – a) acquisition geometry, b) non-cooperative target 'St Faith', c) non-cooperative target 'HSC Wight Ryder I'.

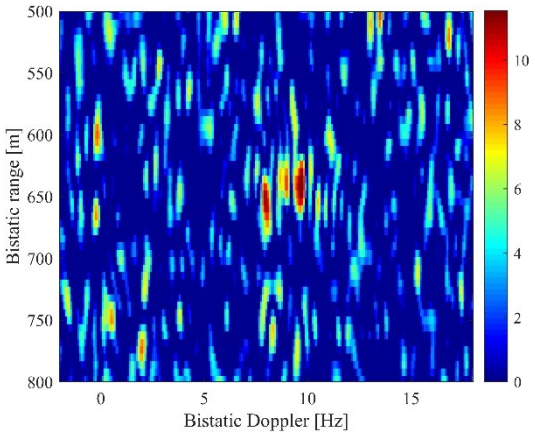

Figure 6.12 – Single frame CPI = 3 s

Figure 6.12 shows the single frame RD map. It can be seen that the target is barely visible; therefore, a long time integration is performed to obtain a better SNR. Figure 6.13 (a) represents the RD map obtained non-coherently integrated 5 frames. The theoretical bandwidth calculated with (6.6) using the AIS information is 3.3 Hz and it is consistent with the experimental results. The white vertical lines in Figure 6.13 indicate the theoretical target occupation from point A to point B. The coordinates of the edges A and B are calculated with the eq. (6.8) and the bistatic Doppler is obtained using the coordinates inside eqs. (3.4) and (3.5). The cross-range scaling is performed in Figure 6.13 (b). As you can see, the experimentally obtained value is comparable with the actual length of the target (41 m). This demonstrates the possibility of obtaining information on the target size even in case of small targets and after the application of the long time integration technique.

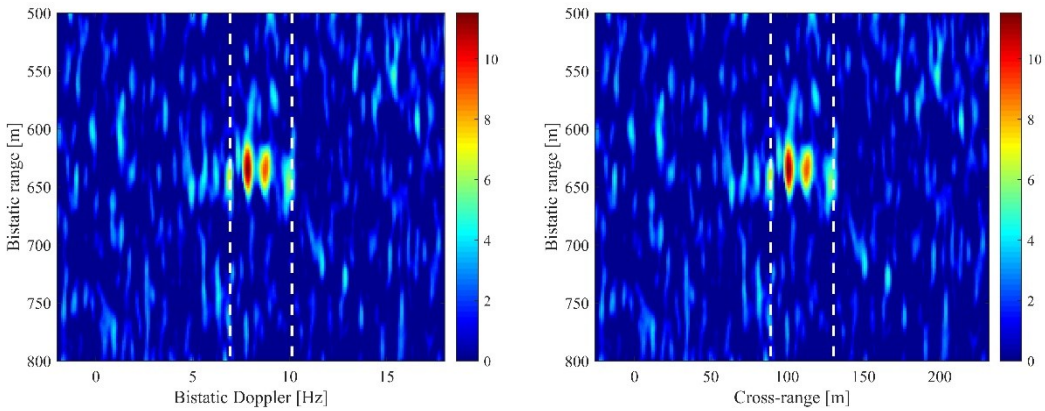

Figure 6.13 - (a) RD image, (b) image after cross-range scaling

Conclusions and Future work

The potential of using GNSS as transmitters of opportunity for maritime surveillance applications has been investigated in this thesis. To this purpose, two main topics have been considered:

- the definition of single-channel and multi-channel M-MTD techniques;
- the features extraction of the detected ship target.

With regard the first topic, the focus has been on the definition of suitable techniques able to properly integrate the returns from moving targets over long dwell times in order to counteract the low power density of the transmitted signal reaching the ground level, which represents the fundamental bottleneck of this technology for target detection. To this purpose firstly the case of single transmitter has been considered, secondly the exploitation of multiple sources has been investigated to improve the detection capability and simultaneously perform the target localization.

Therefore, at the beginning the focus has been on the definition of single-channel M-MTD technique. Particularly, a range-Doppler-based technique has been proposed able to concentrate the signal energy over integration times long enough to reach signal to disturbance levels suitable for the detection of maritime targets of small size. This technique works under the assumption of a linear Doppler history and a proper filter bank has been proposed to match the specific unknown target motion condition. The technique has been preliminarily tested against synthetic

data. Then, results from three experimental trials have been reported and discussed to show the relative improvement in SNR and detection range provided by the integration over long dwell time. The first trial (exploiting Galileo transmissions) involved a commercial ferry and the ground truth was provided by the AIS. The ferry has been successfully detected by two Galileo satellites simultaneously. The results have been preliminary demonstrated the feasibility of a long-time integration MTD technique to detect and track moving targets. Furthermore, they have indicated the potential of this approach to increase the detection performance of the proposed passive radar system, likely allowing the detection of low observable targets. The second trial (using GLONASS transmitter) involved a small cooperative fishing boat equipped with GPS: obtained results clearly demonstrate (i) the need to integrate over long time intervals (some tens of seconds) to detect small targets and, for the integration to be effective, to properly compensate the target motion; (ii) the capability of the technique to adapt to the unknown motion conditions. The third trial (exploiting Galileo transmissions) involved opportunity targets with reference ground truth provided by AIS receiver: obtained results demonstrated the achievement of an experimental integration gain well in line with theoretical predictions thus proving the effectiveness of the proposed approaches in practical applications.

Subsequently, the spatial diversity offered by the large number of navigation satellites simultaneously observing each point over the Earth surface has been exploited. In particular, a multi-channel M-MTD technique for enhancing the detection capability of the system has been proposed by reinforcing the target power by considering both long integration times and multiple illuminators, thus counteracting the restricted power budget provided by these sources representing the main shortcoming of this technology. By means of a single-stage approach, a joint detection and localization of vessels at sea has been demonstrated to be feasible, even for those targets not detectable by means of conventional MTI

approaches, by exploiting the inherent multistatic nature of GNSS-based passive radar systems.

A straightforward QI combination rule has been considered for the combination of the RD maps pertaining different satellites. Even though this does not represent the optimum solution because of the different average RCS observed by multiple perspective, it has been demonstrated that it offers a robust approach reaching comparable performance to those provided by the ideal LRT detector.

Moreover, concerning the variation of the target RCS under different bistatic angles, it has to be pointed out that having multiple independent looks at the target is actually a strong benefit in a multistatic radar system. Indeed, even though the returned target power can be very low for a given bistatic geometry, considering multiple geometry greatly enhances the chances of observing a strong backscattered energy from another bistatic angle, and this is expected to likely hold for the GNSS multistatic passive radar where widely separated and abundant perspectives are simultaneously available.

Experimental results considering two different scenarios involving vessels of different types supported the theoretical performance analysis, confirmed the effectiveness of the technique to jointly detect and localize vessels at sea despite the strong limitation represented by low EIRP sources employed.

With regard the second topic, the possibility to extract features of the detected ships has been investigated. The chance to extract useful information related to the target size depends on the number of range or Doppler cells over which the target spans. First, the target extension measure has been evaluated in range and cross-range domain. When the target motion is mainly radial with respect the receiver, the target length can be retrieved from the bistatic target extension measured on the RD map. When the target motion is tangential, the instantaneous Doppler bandwidth provided by the detected ship has been evaluated as composed by three contributions: the receive related bandwidth due to target translation, the receiver

related bandwidth due to target rotation and the satellite related bandwidth due to target rotation. From it the cross-range axis scaling can be performed. Then, an experimental study has been carried out. The signal transmitted by a satellite of the Galileo constellation and reflected from a ferry has been collected over a dwell time of more than two minutes. By appropriate signal processing, the corresponding RD images over consecutive CPIs have been obtained, allowing the identification of the area occupied by the ferry. The results obtained in range and cross-range domain showed that the target length could be retrieved from the resolution cells over the energy span, thus proving that information about the size of the detected target can be retrieved and therefore exploited in ATR procedures.

For these preliminary results, the target kinematic parameters have been calculated from the AIS information. The information necessary to extract the target length could be obtained autonomously using multiple bistatic couples to obtain information on the target kinematics.

Appendix A

The binary hypothesis test (5.11) can be rewritten as

$$\begin{aligned} &\mathcal{H}_0\colon\ r_{m,n}\sim\mathcal{CN}(0,\sigma_w^2)\\ &\mathcal{H}_1\colon\ r_{m,n}\sim\mathcal{CN}(0,\sigma_m^2+\sigma_w^2) \end{aligned} \tag{A.1}$$

According to the Neyman-Pearson criterion, the optimum solution is obtained by comparing the ratio of the likelihood of the received data under $\mathcal{H}_1$ over that under $\mathcal{H}_0$ to an appropriate threshold t_h set to guarantee the desired level of false alarm rate, carrying to the LRT detector, namely

$$\mathcal{L}=\frac{p(\boldsymbol{r}|\mathcal{H}_1)}{p(\boldsymbol{r}|\mathcal{H}_0)}\underset{\mathcal{H}_0}{\overset{\mathcal{H}_1}{\gtrless}}t_h \tag{A.2}$$

where $\boldsymbol{r}=\left[r_{1,-\frac{N}{2}},\dots,r_{m,-\frac{N}{2}},\dots r_{M,-\frac{N}{2}},\dots,r_{1,n},\dots,r_{m,n},\dots,r_{M,\frac{N}{2}-1}\right]$ is the $1\times MN$ vector of the received data, $p(\boldsymbol{r}|\mathcal{H}_0)$ and $p(\boldsymbol{r}|\mathcal{H}_1)$ are their probability density functions under the null and alternative hypothesis, respectively. Assuming both disturbance and target to be independent from frame to frame and from bistatic link to bistatic link, they are given by

$$p(\boldsymbol{r}|\mathcal{H}_j) = \prod_{m=1}^{M} \prod_{n=-\frac{N}{2}}^{\frac{N}{2}-1} \frac{1}{\sigma_w^2 + j\sigma_m^2} \exp\left\{ -\frac{|r_{m,n}|^2}{\sigma_w^2 + j\sigma_m^2} \right\}, j = 0,1 \tag{A.3}$$

Substituting (A.3) into (A.2) and taking the logarithm yields

$$\begin{aligned} -N \sum_m \ln(\sigma_w^2 + \sigma_m^2) - \sum_m \frac{1}{(\sigma_w^2 + \sigma_m^2)} \sum_n |r_{m,n}|^2 + \mathrm{NM} \cdot \ln(\sigma_w^2) \\ + \frac{1}{\sigma_w^2} \sum_m \sum_n |r_{m,n}|^2 \end{aligned} \tag{A.4}$$

Carrying out the calculus, the test statistic can be written as

$$\mathcal{L} = \sum_m \sum_n \frac{\sigma_m^2}{\sigma_w^2 + \sigma_m^2} |r_{m,n}|^2 \underset{\mathcal{H}_0}{\overset{\mathcal{H}_1}{\gtrless}} t_h^{LRT} \tag{A.5}$$

where the threshold in (A.5) is a suitable modified version of the threshold in (A.2).

Finally, $\frac{\sigma_m^2}{\sigma_w^2+\sigma_m^2}$ can be rewritten as $\frac{SNR_m}{SNR_m+1}$, so that (A.5) can be equivalently written as (5.12).

Appendix B

For a generic positive random variable x gamma-distributed with shape parameter α and scale parameter β, denoted as $x \sim \Gamma(\alpha, \beta)$, the probability density function is given by

$$p_X(x) = \frac{x^{\alpha-1} e^{-\frac{x}{\beta}}}{\Gamma(\alpha)\, \beta^N}, x > 0 \tag{B.1}$$

Let us define the random variable $q_m = \sum_n |r_{m,n}|^2$. From the statistical model (5.11) [or, equally, (A.1)], it follows that under $\mathcal{H}_0$ q_m has a probability density function as (B.1) with $\alpha = N$ and $\beta = \sigma_w^2$, i.e. $q_m \sim \Gamma(N, \sigma_w^2)$, while under $\mathcal{H}_1$, $q_m \sim \Gamma(N, \sigma_m^2 + \sigma_w^2)$. Further, we define the random variable $q'_m = \eta_m q_m$. It follows that $q'_m \sim \Gamma(N, \eta_m \sigma_w^2)$ under $\mathcal{H}_0$ and $q'_m \sim \Gamma\big(N, \eta_m(\sigma_m^2 + \sigma_w^2)\big)$ under $\mathcal{H}_1$.

Let us define the random variables $q = \sum_m q_m$ and $q' = \sum_m q'_m$. The P_{fa} for the LRT and the QI are given by

$$P_{fa}^{LRT} = \int_{t_h^{LRT}}^{\infty} p(q'|\mathcal{H}_0) dq = 1 - P_{q'|\mathcal{H}_0}\big(t_h^{LRT}\big) \tag{B.2}$$

$$P_{fa}^{QI} = \int_{t_h^{QI}}^{\infty} p(q|\mathcal{H}_0) dq = 1 - P_{q|\mathcal{H}_0}\big(t_h^{QI}\big) \tag{B.3}$$

where $P(\cdot)$ denotes the distribution function.

For the P_d, we have

$$P_d^{LRT} = 1 - P_{q'|\mathcal{H}_1}\left(t_h^{LRT}\right) \tag{B.4}$$

and

$$P_d^{QI} = 1 - P_{q|\mathcal{H}_1}\left(t_h^{QI}\right) \tag{B.5}$$

Therefore, to evaluate the LRT and QI performance we need expressions of $P_{q'|\mathcal{H}_0}$, $P_{q|\mathcal{H}_0}$, $P_{q'|\mathcal{H}_1}$ and $P_{q|\mathcal{H}_1}$.

Under the null hypothesis, q is the result of the summation of M identically distributed gamma variates. Therefore $q \sim \Gamma(MN, \sigma_w^2)$ and $P_{q|\mathcal{H}_0}(x) = \frac{\gamma\left(MN, {}^{x}/_{\sigma_w^2}\right)}{\Gamma(MN)}$. Replacing in (B.3), (5.17) is obtained.

Variables q (under $\mathcal{H}_1$) and q' (under both $\mathcal{H}_0$ and $\mathcal{H}_1$) are each one the result of a summation of M gamma-variates with same shape but different scale. The distribution function of the sum of M independent gamma random variables $x_m \sim \Gamma(\alpha, \beta_m)$ with $\beta_m{}'$ not restricted to be identical is given by [75]

$$P(\omega) = C \cdot \sum_{k=0}^{\infty} \delta_k \int_0^{\omega} \frac{x^{\rho+k-1}\, e^{-\frac{x}{\beta_1}}}{\Gamma(\rho+k)\beta_{min}^{\rho+k}} dx\,, \quad x > 0 \tag{B.6}$$

where $\beta_{min} = \min_m \beta_m$ and $\rho = \alpha M$; C is equal to

$$C = \prod_{m=1}^{M} \left(\frac{\beta_{min}}{\beta_m}\right)^{\alpha} \tag{B.7}$$

and the coefficients δ_k can be recursively obtained as

$$\delta_{k+1} = \frac{1}{k+1} \sum_{i=1}^{k+1} i\, g_i\, \delta_{k+1-i}\,, \qquad k = 0,1,2,\ldots \tag{B.8}$$

by setting $\delta_0 = 1$ and evaluating the parameters g_i by the following rule

$$g_k = \frac{\alpha}{k} \sum_{m=1}^{M} \left(1 - \frac{\beta_{min}}{\beta_m}\right)^k, \quad k = 1,2,\ldots \tag{B.9}$$

In (B.6) it can be observed that the integral represents the distribution function of a random variable $x \sim \Gamma(\rho + k, \beta_{min})$ evaluated in ω. Therefore, $P(\omega)$ can be rewritten as

$$P(\omega) = C \cdot \sum_{k=0}^{\infty} \delta_k \frac{\gamma\left(\alpha M, {}^{\omega}/_{\beta_{min}}\right)}{\Gamma(\rho + k)}, \quad x > 0 \tag{B.10}$$

By using the above equations, $P_{q'|\mathcal{H}_0}$, $P_{q'|\mathcal{H}_1}$, and $P_{q|\mathcal{H}_1}$ can be obtained by proper setting of α and β_m. In particular, in all the cases $\alpha = N$ and therefore $\rho = MN$. Table B1 lists the remainder settings to apply to (B.10) to obtain the three distribution functions, where $\sigma_{min}^2 = \min_m \sigma_m^2$ and $\eta_{min} = \frac{SNR_{min}}{SNR_{min}+1}$. Replacing the corresponding functions in (B.2) and in (B.4) with $\omega = t_h^{LRT}$ and in (B.5) with $\omega = t_h^{QI}$, after some simple manipulations P_{fa}^{LRT}, P_d^{LRT}, and P_d^{QI} are found as(5.16), (5.18), and (5.19), respectively.

It should be noted that exact evaluation of (B.10) would require the computation of an infinite series. For practical purposes, only the first K' coefficient can be computed, where K' has to assure an approximation error lower than a desired accuracy [75].

TABLE B1 PARAMETERS OF THE DISTRIBUTION FUNCTION (B.10) FOR THE EVALUATION OF THE CA AND LRT DETECTORS PERFORMANCE

$P(\omega)$	β_m	β_{min}	C	δ_k
			From (B.7)	Recursively evaluated by (B.8) and (B.9)
$P_{q'\|\mathcal{H}_0}$	$\eta_m\sigma_w^2$	$\eta_{min}\sigma_w^2$	$C_A = \prod_{m=1}^{M}\left(\frac{\eta_{min}}{\eta_m}\right)^N$	$\delta_{A_{k+1}} = \frac{1}{k+1}\sum_{i=1}^{k+1} i\, g_{A_i}\, \delta_{A_{k+1-i}}$, $k = 0,1,2,\ldots$ $g_{A_k} = \frac{N}{k}\sum_{m=1}^{M}\left(1-\frac{\eta_{min}}{\eta_m}\right)^k$, $k = 1,2,\ldots$ $\delta_{A_0} = 1$
$P_{q'\|\mathcal{H}_1}$	$\eta_m(\sigma_m^2 + \sigma_w^2)$	$\eta_{min}(\sigma_{min}^2 + \sigma_w^2)$	$C_B = \prod_{m=1}^{M}\left(\frac{SNR_{min}}{SNR_m}\right)^N$	$\delta_{B_{k+1}} = \frac{1}{k+1}\sum_{i=1}^{k+1} i\, g_{B_i}\, \delta_{B_{k+1-i}}$, $k = 0,1,2,\ldots$ $g_{B_k} = \frac{N}{k}\sum_{m=1}^{M}\left(1-\frac{SNR_{min}}{SNR_m}\right)^k$, $k = 1,2,\ldots$ $\delta_{B_0} = 1$
$P_{q\|\mathcal{H}_1}$	$(\sigma_m^2 + \sigma_w^2)$	$(\sigma_{min}^2 + \sigma_w^2)$	$C_C = \prod_{m=1}^{M}\left(\frac{SNR_{min}+1}{SNR_m+1}\right)^N$	$\delta_{C_{k+1}} = \frac{1}{k+1}\sum_{i=1}^{k+1} i\, g_{C_i}\, \delta_{C_{k+1-i}}$, $k = 0,1,2,\ldots$ $g_{C_k} = \frac{N}{k}\sum_{m=1}^{M}\left(1-\frac{SNR_{min}+1}{SNR_m+1}\right)^k$, $k = 1,2,\ldots$ $\delta_{C_0} = 1$

References

[1] R. Zemmari, M. Broetje, G. Battistello, and U. Nickel, "GSM passive coherent location system: performance prediction and measurement evaluation," IET Radar Sonar Navig., vol. 8, Iss. 2, pp. 94-105, 2014.

[2] K. Chetty, K. Woodbridge, H. Gui, G. E. Smith, "Passive bistatic WiMAX radar for marine surveillance," Proc. IEEE Int. Radar Conf., pp. 188-193, Washington, DC, USA, May 2010.

[3] F. Colone, D. Langellotti, P. Lombardo, "DVB-T Signal Ambiguity Function Control for Passive Radars", IEEE Trans. on Aerospace and Electronic Systems, vol. 50, no. 1, pp. 329-347, Jan. 2014.

[4] Navstar IS-GPS-200E, "Interface Specification", IRN-IS-200H-003, Dec. 2015.

[5] Russian Institute of Space Device Engineering, "Global Navigation Satellite System GLONASS Interface Control document", (Edition 5.1), 2008.

[6] China Satellite Navigation Office, "BeiDou Navigation Satellite System Signal In Space Interface Control Document", Open Service Signal (Version 2.0), Dec. 2013.

[7] European space agency/European GNSS, "Galileo open service, signal in space interface control document (OS SIS ICD)," Nov. 2015.

[8] M. Martín-Neira, "A Passive Reflectometry and Interferometry System (PARIS): Application to Ocean Altimetry," ESA Journal, vol. 17 (1993), pp. 331-355

[9] S. Jin, G.P. Feng, S. Gleason, "Remote sensing using GNSS signals: Current status and future directions," J. Adv. Space Research, 47 (2011), pp. 1645-1653.

[10] V.U. Zavorotny, S. Gleason, E. Cardellach, A. Camps, "Tutorial on remote sensing using GNSS bistatic radar of opportunity" , IEEE Geoscience and Remote Sensing Magazine, 2 (4), 2014, pp. 8-45.

[11] M. Cherniakov and T. Zeng, Passive Bistatic SAR with GNSS Transmitters, in Bistatic Radar: Emerging Technology, M. Cherniakov, Ed. New York: Wiley 2008.

[12] M. Antoniou and M. Cherniakov, "GNSS-based bistatic SAR: a signal processing view," EURASIP J. Adv. Sign. Process. 2013, 2013:98.

[13] M. Antoniou, Z. Zeng, F. Liu, M. Cherniakov, "Experimental demonstration of passive BSAR imaging using navigation satellites and a fixed receiver," IEEE Geosci. Remote Sens. Lett., vol. 9, no. 3, pp. 477-481, May 2013.

[14] M. Antoniou, Z. Hong, Z. Zhangfan, R. Zuo, Q. Zhang and M. Cherniakov, "Passive bistatic synthetic aperture radar imaging with Galileo transmitters and a moving receiver: experimental demonstration," in IET Radar Sonar Nav., vol. 7, no. 9, pp. 985-993, December 2013

[15] Q. Zhang, M. Antoniou, W. Chang, and M. Cherniakov, "Spatial decorrelation in GNSS-based SAR coherent change detection," IEEE Trans. Geosci. Remote Sens., vol. 53, no. 1, pp. 219-228, Jan. 2015.

[16] F. Santi, M. Antoniou, and D. Pastina, "Point Spread Function Analysis for GNSS-based Multistatic SAR," IEEE Geosci. Remote Sens. Lett., vol. 12, no. 2, pp. 304-308, Feb. 2015.

[17] H. Ma, M. Antoniou, and M. Cherniakov, "Passive GNSS-based SAR resolution improvement using joint Galileo E5 signals," IEEE Geosci. Remote Sens. Lett., vol. 12, no. 8, pp. 1640-1644, Aug. 2015.

[18] F. Santi, M. Bucciarelli, D. Pastina, M. Antoniou, and M. Cherniakov, "Spatial Resolution Improvement in GNSS-based SAR Using Multistatic Acquisitions and Feature Extraction," IEEE Trans. Geosci. Remote Sens., vol. 54, no. 10, pp. 6217-6231, Oct. 2016.

[19] A. G. Dempster, E. P. Glennon, and C. Rizos, "Feasibility of air target detection using GPS as a bistatic radar," J. Global Pos. Syst., 5, 1-2 (2006).

[20] I. Suberviola, I. Mayordomo, and J. Mendizabal. Experimental results of air target detection with a GPS forward-scattering radar," IEEE Geosci. Remote Sens. Lett., vol. 9, no. 1, pp. 47-51, Jan. 2012.

[21] S. Wachtl, V. Koch, L.-P. Schmidt, "Global Navigation Satellite Systems in Passive Surveillance Applications," Tyrrhenian International Workshop on Digital Communications – Enhanced Surveillance of Aircraft and Vehicles, Rome, 2014, pp. 135-140.

[22] A. Di Simone, H. Park, D. Riccio and A. Camps, "Sea Target Detection Using Spaceborne GNSS-R Delay-Doppler Maps: Theory and Experimental Proof of Concept Using TDS-1 Data," in IEEE Journal of Selected Topics in Applied Earth Observations and Remote Sensing, vol. 10, no. 9, pp. 4237-4255, Sept. 2017.

[23] M. Antoniou, Z. Hong, Z. Zhangfan, R. Zuo, Q. Zhang and M. Cherniakov, "Passive bistatic synthetic aperture radar imaging with Galileo transmitters and a moving receiver: experimental demonstration," in IET Radar, Sonar & Navigation, vol. 7, no. 9, pp. 985-993, December 2013.

[24] M.-P. Clarizia, P. Braca, C. S. Ruf, P. Willet, "Target detection using GPS signals of opportunity," 2015 18th International Conference on Information Fusion, art. No 7266725, pp. 1429-1436.

[25] A.K. Brown, "Remote sensing using bistatic GPS and digital beam-steering receiver," 2005 International Geoscience and Remote Sensing Symposium (IGARSS), 1, pp. 416-419.

[26] X. He, M. Cherniakov, T. Zeng., "Signal detectability in SS-BSAR with GNSS non-cooperative transmitter," IEE Proceedings Radar, Sonar and Navigation, vol. 152, no. 3, pp. 124-132, Jun. 2005.

[27] Xu, J., Yu, J., Peng, Y.-N., et al., "Radon-Fourier transform for radar target detection, I: generalized Doppler filter bank," IEEE Trans. Aerosp. Electron. Syst., vol. 47, no. 2, pp. 1186–1202, Apr. 2011

[28] X. Chen, J. Guan, N. Liu, and Y. He, “Maneuvering Target Detection via Radon-Fractional Fourier Transform-Based Long-Time Coherent Integration,” IEEE Trans. Signal Process., vol. 62, no. 4, pp. 939-953, Feb. 2014.

[29] K. Kulpa, and J. Misiurewicz, “Stretch processing for long integration time passive covert radar,” 2006 CIE International Conference on Radar, Shanghai, 2006, pp. 1-4.

[30] T. Zeng et al., "Multiangle BSAR Imaging Based on BeiDou-2 Navigation Satellite System: Experiments and Preliminary Results," IEEE Trans. Geosci. Remote Sens, vol. 53, no. 10, pp. 5760-5773, Oct. 2015.

[31] E. Fisher, et al., “Spatial diversity in radars – Models and detection performance,” IEEE Trans. Sign. Process., vol. 54, no. 3, pp. 823-838, Mar. 2006.

[32] H. Ma, M. Antoniou, A.G. Stove, J. Winkel, and M. Cherniakov, “Maritime moving target localization using passive GNSS-based multistatic radar,” IEEE Trans. Geosci. Remote Sens, vol. 56, no. 8, pp. 4808-4819, Aug. 2018.

[33] G. Mellen, M. Patcher, J. Racquet, “Closed-form solution for determining emitter location using time difference of arrival measurements,” IEEE Trans. Aerosp. Electron. Syst., vol. 39, no. 3, pp. 1056-1058, Jul. 2003.

[34] www.spyglassproject.eu

[35] H. Ma, M. Antoniou, D. Pastina, F. Santi, F. Pieralice, M. Bucciarelli, M. Cherniakov, “Maritime Target Detection Using GNSS-Based Radar: Experimental Proof of Concept”, IEEE Radar Conference 2017, Seattle, WA, USA, May 2017.

[36] H. Ma, M. Antoniou, D. Pastina, F. Santi, F. Pieralice, M. Bucciarelli, M. Cherniakov, “Maritime Moving Target Indication Using Passive GNSS-based Bistatic Radar”, IEEE Transactions on Aerospace and Electronic Systems, vol. 54, no. 1, pp. 115-130, Feb. 2018.

[37] F. Pieralice, F. Santi, D. Pastina, M. Bucciarelli, H. Ma, M. Antoniou, M. Cherniakov, “GNSS-Based Passive Radar for Maritime Surveillance: Long Integration Time MTI Technique,” IEEE Radar Conference 2017, Seattle, WA, USA, May 2017.

[38] D. Pastina, F. Santi, F. Pieralice, M. Bucciarelli, H. Ma, D. Tzagkas, M. Antoniou, M. Cherniakov, “Maritime moving target long time integration for GNSS-based passive

bistatic radar", IEEE Trans. Aerosp. Electron. Syst., in IEEE Transactions on Aerospace and Electronic Systems, vol. 54, no. 6, pp. 3060-3083, Dec. 2018.

[39] F. Pieralice, D. Pastina, F. Santi, M. Bucciarelli, "Multi-transmitter ship target detection technique with GNSS-based passive radar," Proc. Int. Conf. on Radar Syst., Belfast, Oct. 2017, pp. 1-6.

[40] F. Santi, F. Pieralice, D. Pastina, "Multistatic GNSS-based passive radar for maritime surveillance with long integration times: experimental results," Proc. IEEE RadarConf18, Oklahoma City, OK, Apr. 2018, pp. 1260-1265.

[41] F. Santi, F. Pieralice, D. Pastina, "Joint detection and localization of vessels at sea with a GNSS-based multistatic radar", submitted to Transactions on Geoscience and Remote Sensing currently under review

[42] F. Pieralice, F. Santi, D. Pastina, M. Antoniou and M. Cherniakov, "Ship targets feature extraction with GNSS-based passive radar via ISAR approaches: preliminary experimental study," EUSAR 2018 12th European Conference on Synthetic Aperture Radar, Aachen, Germany, 2018, pp. 1-5.

[43] M. I. Skolnik, "Radar Handbook", McGraw- Hill 1970.

[44] N.J. Willis, "Bistatic Radar", 2nd ed. SciTech Publishing Inc., 2005.

[45] V.S. Chernyak, "Fundamentals of multisite radar systems", Gordonand Breach Science Publishers, 1998.

[46] M. Cherniakov, "Bistatic Radar: Emerging Technology", John Wiley & Sons, UK

[47] M. Antoniou, Z. Zeng, L. Feifeng and M. Cherniakov, "Experimental Demonstration of Passive BSAR Imaging Using Navigation Satellites and a Fixed Receiver," in IEEE Geoscience and Remote Sensing Letters, vol. 9, no. 3, pp. 477-481, May 2012.

[48] M. Antoniou, Z. Hong, Z. Zhangfan, R. Zuo, Q. Zhang and M. Cherniakov, "Passive bistatic synthetic aperture radar imaging with Galileo transmitters and a moving receiver: experimental demonstration," in IET Radar, Sonar & Navigation, vol. 7, no. 9, pp. 985-993, December 2013.

[49] Antoniou, M., Cherniakov, H. Ma, “Space-surface bistatic synthetic aperture radar with navigation satellite transmissions: a review”, Sci. China Inf. Sci. (2015) 58: 1.

[50] D. Pastina, M. Sedehi, D. Cristallini, “Geostationary satellite based passive bistatic ISAR for coastal surveillance”, 2010 IEEE Radar Conference, May 2010, pp. 865–870.

[51] S. Brisken, M. Moscadelli, V. Seidel, and C. Schwark, “Passive Radar Imaging Using DVBS2”,2017 IEEE Radar Conference, May 2017, pp. 552 - 556.

[52] I. Pisciottano, D. Cristallini, J. Schell and V. Seidel, "Passive ISAR for Maritime Target Imaging: Experimental Results," 2018 19th International Radar Symposium (IRS), Bonn, 2018, pp. 1-10.

[53] A. Manno-Kovacs, E. Giusti, F. Berizzi, L. Kovács: “Automatic Target Classification in Passive ISAR Range-Crossrange Images”, Proc. of 2018 IEEE Radar Conference, April 2018.

[54] M. Rodriguez-Cassola, S. V. Baumgartner, G. Krieger and A. Moreira, "Bistatic TerraSAR-X/F-SAR Spaceborne–Airborne SAR Experiment: Description, Data Processing, and Results," in IEEE Transactions on Geoscience and Remote Sensing, vol. 48, no. 2, pp. 781-794, Feb. 2010.

[55] I. Walterscheid et al., "Bistatic SAR Experiments With PAMIR and TerraSAR-X—Setup, Processing, and Image Results," in IEEE Transactions on Geoscience and Remote Sensing, vol. 48, no. 8, pp. 3268-3279, Aug. 2010.

[56] P.Z. Peebles Jr. “Radar principles”, John Wiley & Sons, New York, 1998.

[57] W. J. Albersheim, “A closed-form approximation to Robertson’s detection characteristics”, Proc. IEEE, 69 (1981).

[58] B. D. Carlson, E. D. Evans, S. L. Wilson, "Search radar detection and track with the Hough transform (I): System concept", IEEE Transactions on Aerospace and Electronic Systems, vol. 30, no. 1, pp. 102-108, Jan. 1994.

[59] B. D. Carlson, E. D. Evans, S. L. Wilson, "Search radar detection and track with the Hough transform (II): Detection statistics", IEEE Transactions on Aerospace and Electronic Systems, vol. 30, no. 1, pp. 109-115, Jan. 1994.

[60] B. D. Carlson, E. D. Evans, S. L. Wilson, "Search radar detection and track with the Hough transform (III): Detection performance with binary integration", IEEE Transactions on Aerospace and Electronic Systems, vol. 30, no. 1, pp. 116-125, Jan. 1994.

[61] L. Yang, T. Zeng, T. Long, W. Zheng, "Range migration compensation and Doppler ambiguity resolution by Keystone transform", Proceedings of the CIE. International Conference on Radar, pp. 1466-1469, 2006.

[62] A. S. Paulus, W. L. Melvin and D. B. Williams, "Multistage Algorithm for Single-Channel Extended-Dwell Signal Integration," in IEEE Transactions on Aerospace and Electronic Systems, vol. 53, no. 6, pp. 2998-3007, Dec. 2017.

[63] J. Xu, X. Zhou, L. Qian, X. Xia and T. Long, "Hybrid integration for highly maneuvering radar target detection based on generalized radon-fourier transform," in IEEE Transactions on Aerospace and Electronic Systems, vol. 52, no. 5, pp. 2554-2561, October 2016.

[64] K. S. Kulpa, J. Misiurewicz, "Stretch Processing for Long Integration Time Passive Covert Radar," 2006 CIE International Conference on Radar, Shanghai, 2006, pp. 1-4.

[65] J. M. Christiansen, K. E. Olsen and G. Weiß, "Coherent range and Doppler-walk compensation in PBR applications," 2014 15th International Radar Symposium (IRS), Gdansk, 2014, pp. 1-4.

[66] M. Malanowski, K. Kulpa and K. E. Olsen, "Extending the integration time in DVB-T-based passive radar," 2011 8th European Radar Conference, Manchester, 2011, pp. 190-193.

[67] T. Kelso, "CelesTrak," Public Domain Satellite Tracking Data, 2010. [Online]. Available: http://celestrak.com/

[68] F. Colone, D. W. O'Hagan, P. Lombardo and C. J. Baker, "A Multistage Processing Algorithm for Disturbance Removal and Target Detection in Passive Bistatic Radar," IEEE Trans. Aerosp. Electr. Syst., vol. 45, no. 2, pp. 698-722, April 2009.

[69] D.E. Hack, L. K. Patton, A. D. Kerrick, and M. Saville, "Direct Cartesian detection, localization, and de-ghosting for passive multistatic radar," Proc. IEEE 7th Sensor Array and Multichannel Processing Workshop, pp. 45-48, 2012.

[70] D. Zhu, and Z. Zhu, "Range Resampling in the Polar Format Algorithm for Spotlight SAR Image Formation Using the Chirp z-Transform," IEEE Trans. Sign. Process., vol. 55, no. 3, pp. 1011-1023, Mar. 2007.

[71] D. Baumgarten, "Optimum detection and receiver performance for multistatic radar configurations," Proc. IEEE Int. Conf. Acoustics, Speech, and Signal Proc., 1982, pp. 359-362.

[72] www.marinetraffic.com

[73] D.R. Wehner, "High Resolution Radar", Norwood, MA, Artech House, Inc., 1995, 2nd edn.

[74] F. Colone, D. Pastina and V. Marongiu, "VHF Cross-Range Profiling of Aerial Targets Via Passive ISAR: Signal Processing Schemes and Experimental Results," in IEEE Transactions on Aerospace and Electronic Systems, vol. 53, no. 1, pp. 218-235, Feb. 2017.

[75] P. G. Moschopoulos, "The distribution of the sum of independent gamma random variables", Ann. Inst. Statist. Math., vol. 37, no. 1, Dec. 1985, pp. 541-544.

List of publications

This research has resulted in the following publications:

Journals

1. H. Ma, M. Antoniou, D. Pastina, F. Santi, F. Pieralice, M. Bucciarelli, M. Cherniakov, "Maritime Moving Target Indication Using Passive GNSS-Based Bistatic Radar," in IEEE Transactions on Aerospace and Electronic Systems, vol. 54, no. 1, pp. 115-130, Feb. 2018.
2. D. Pastina, F. Santi, F. Pieralice, M. Bucciarelli, H. Ma, D. Tzagkas, M. Antoniou, M. Cherniakov, "Maritime moving target long time integration for GNSS-based passive bistatic radar," in IEEE Transactions on Aerospace and Electronic Systems, vol. 54, no. 6, pp. 3060-3083, Dec. 2018.
3. F. Santi, F. Pieralice, D. Pastina, "Joint detection and localization of vessels at sea with a GNSS-based multistatic radar", submitted to Transactions on Geoscience and Remote Sensing currently under review

Conferences

1. F. Pieralice, F. Santi, D. Pastina, M. Bucciarelli, H. Ma, M. Antoniou, M. Cherniakov, "GNSS-Based Passive Radar for Maritime Surveillance: Long Integration Time MTI Technique", 2017 IEEE Radar Conference (RadarConf), Seattle, WA, 2017, pp. 0508-0513.
2. H. Ma, M. Antoniou, D. Pastina, F. Santi, F. Pieralice, M. Bucciarelli, M. Cherniakov, "Maritime target detection using GNSS-based radar: Experimental proof of concept," 2017 IEEE Radar Conference (RadarConf), Seattle, WA, 2017, pp. 0464-

0469.

3. F. Pieralice, D. Pastina, F. Santi and M. Bucciarelli, "Multi-transmitter ship target detection technique with GNSS-based passive radar," International Conference on Radar Systems (Radar 2017), Belfast, 2017, pp. 1-6.

4. F. Santi, F. Pieralice and D. Pastina, "Multistatic GNSS-based passive radar for maritime surveillance with long integration times: Experimental results," 2018 IEEE Radar Conference (RadarConf18), Oklahoma City, OK, 2018, pp. 1260-1265.

5. F. Pieralice, F. Santi, D. Pastina, M. Antoniou, M. Cherniakov, "Ship targets feature extraction with GNSS-based passive radar via ISAR approaches: preliminary experimental study", 12th European Conference on Synthetic Aperture Radar (EUSAR 2018), Aachen, Germany, June 4-7th, 2018. – Second place Student paper award.

6. F. Santi, F. Pieralice, D. Pastina, M. Antoniou, M. Cherniakov, "Passive radar imagery of ship targets by using navigation satellites transmitters of opportunity", submitted to IRS 2019 (International Radar Symposium), 28 June 2019, Ulm, Germany

International workshops

1. F. Pieralice, F. Santi, D. Pastina, M. Bucciarelli, H. Ma, M. Antoniou, M. Cherniakov, "GNSS-Based Passive Radar Detection for Maritime Surveillance", GTTI Radar and Remote Sensing Workshop 2017, Naples, Italy, 25-26 May 2017.

2. F. Santi, F. Pieralice, D. Pastina, "Multistatic GNSS-Based Passive Radar for Maritime Surveillance", GTTI Radar and Remote Sensing Workshop 2018, Pavia, Italy, 28-29 May 2018.

Acknowledgments

This work was carried out during the year 2015-2018 at the "Radar Remote Sensing and Navigation" (RRSN) group at the Department of Information Engineering and Telecommunications, Sapienza University of Rome.

I would like to express my sincere gratitude to my supervisor Prof. D. Pastina for her support on my research during my PhD study.